Effects of a Single Moving Mass on the Dynamics of a Samara-Inspired Vehicle

Peter F. Tyree

Thesis submitted to the faculty of the Virginia Polytechnic Institute and State University
in partial fulfillment of the requirements for the degree of

Master of Science
In
Aerospace Engineering

Shane D. Ross, Chair
Craig A. Woolsey
Sevak Tahmasian

4 May 2026
Blacksburg, VA

Keywords: Samara Seeds, Time-Varying Dynamics, Blade Element Theory, Moving Mass Control

Copyright 2026

Effects of a Single Moving Mass on the Dynamics of a Samara-Inspired Vehicle

Peter F. Tyree

ABSTRACT

Nature has often been used as a source of inspiration for dynamics. The simple yet elegant design of the single-winged samara seed has been theorized as a form of evolution that has enabled the distribution of large seeds to greater distances in the presence of prevalent wind conditions resulting from the characteristic stable autorotation that slows vertical descent. This behavior has interested engineers and technologists alike in application areas that include sensor network distribution over large areas as well as precision package-drop operations. While past biomimetic samara-inspired vehicle designs have focused on the use of wing flaps, wingtip rudders, and propellers, this work explores for the first time the use of a single moving mass actuator as a potential means of control without external actuating surfaces. A six degree of freedom time-varying triple-mass rigid body model was derived for a samara-inspired vehicle with a moving mass actuator on a linear rail to assess the possible use of moving mass control in future samara autorotating wing vehicle design. For the model, blade element theory was used to define the forces and moments used for the equations of motion. The results of four case studies demonstrated an ability to laterally displace the samara as well as affect the biased direction of the displacement that shows promise for future vehicle design.

Effects of a Single Moving Mass on the Dynamics of a Samara-Inspired Vehicle

Peter F. Tyree

GENERAL AUDIENCE ABSTRACT

Nature has often been used as a source of inspiration for engineering. The simple yet elegant design of the samara seed has been theorized as a form of evolution that has enabled the distribution of large seeds to greater distances in the presence of prevalent wind conditions resulting from the characteristic autorotational behavior, slowing vertical descent. This behavior has interested engineers and technologists alike in application areas that include sensor network distribution over large areas as well as precision package-drop operations. While past samara-inspired vehicle designs have focused on a variety of control features, this work explores for the first time the use of a single moving mass actuator as a potential means of control without changing the external surfaces. A model was derived for a samara-inspired vehicle to assess the possible use of moving mass control in future samara autorotating wing vehicle design. The results of four case studies demonstrated an ability to affect position and direction that offers promise for future vehicle design.

Acknowledgements

First, I would like to thank Dr. Shane Ross for his mentorship and advice throughout the development of this thesis. When I first sought him out as my advisor, I was still uncertain what I wanted the focus of the research to be. Dr. Ross provided the initial spark of interest, motivation, and constant guidance throughout the research development process that helped hone the concepts and goals of this project into the final report that is presented here.

Early in the research gathering process, I came across a recently published article that presented a reduced order samara dynamic model. I reached out to the authors, Dr. Tuhin Das and Dr. Jonathan McConnell, who were willing to help me understand the nuanced behavior of the samara seed and their model. Dr. McConnell graciously took the time to meet with me, talk me through his dynamic model, and provide me the supporting MATLAB scripts and Simulink model. The provided scripts were eventually used as the foundation for the six degree of freedom time-varying triple-mass rigid body model implementation developed and used in this report. I am grateful for this willingness to collaborate and for them sharing their research in the greater pursuit of knowledge.

Last, and certainly not least, I would like to thank my wife, Kristin, who patiently bided her time as I invested countless hours dedicated to this project over the past few years. I am incredibly grateful for the emotional support and constant source of motivation that undoubtedly had a positive influence on the work produced.

Table of Contents

List of Figures

List of Tables

Appendices

List of Abbreviations and Symbols

Abbreviations

BEMT	Blade Element Momentum Theory
BET	Blade Element Theory
CFD	Computational Fluid Dynamics
c.m.	Center of Mass
DARPA	Defense Advanced Research Project Agency
DoF	Degrees of Freedom
dSAW	diving Single Autorotating Wing
F-SAM	Foldable Single Actuator Monocopter
LEV	Leading Edge Vortex
M&D	McConnell and Das
MMC	Moving Mass Control
mSAW	motorized Single Autorotating Wing
NAV	Nano Air Vehicle
PIV	Particle Image Velocimetry
SAW	Samara Autorotating Wing
UAV	Unmanned Aerial Vehicle

Symbols

a	samara wingspan
b	samara wing width
$\hat{b}_x$	x component of the fixed body unit vector
$\hat{b}_y$	y component of the fixed body unit vector
$\hat{b}_z$	z component of the fixed body unit vector
C_L	samara lift coefficient
C_D	samara drag coefficient
C_{D_0}	tunable drag coefficient
D	net drag force across span of samara wing
$\hat{e}_x$	x component of the inertial unit vector
$\hat{e}_y$	y component of the inertial unit vector
$\hat{e}_z$	z component of the inertial unit vector
$\mathcal{F}_b$	fixed body reference frame
$\mathcal{F}_i$	inertial reference frame
$\boldsymbol{F}_b$	net generalized forces as seen from the fixed body reference frame
$\boldsymbol{F}_i$	net generalized forces as seen from the inertial reference frame
$\boldsymbol{F}_g$	gravitational force acting on the samara
g	gravitational acceleration
$\boldsymbol{H}_Q$	angular momentum about an arbitrary point Q
$\boldsymbol{I}_C$	moment of inertia about a rigid body's center of mass
$\boldsymbol{I}_Q$	moment of inertia about an arbitrary reference point Q

I_{xx}	*x* component of the moments of inertia
I_{yy}	*y* component of the moments of inertia
I_{zz}	*z* component of the moments of inertia
L	Net lift force across span of samara wing
l	Samara Seed Length
m	Total Mass of the Samara
m_{comp}	Mass of the composite model (equivalent notation: m)
m_m	Mass of the Moving Mass
m_s	Mass of the Samara Seed
m_w	Mass of the Samara Wing
$\boldsymbol{M}_c$	Applied moment about the center of mass of the samara
M_x	*x* component of the applied angular moment about the center of mass
M_y	*y* component of the applied angular moment about the center of mass
M_z	*z* component of the applied angular moment about the center of mass
O	inertial reference frame origin
Q	fixed body reference frame origin
q_∞	dynamic pressure acting on the samara
r_0	lower bound of samara wingspan used for BET
r_f	upper bound of samara wingspan used for BET
$\boldsymbol{r}_O$	inertial position vector of the fixed body origin Q
R_{final}	Case 3: final moving mass position
R_{ub}	upper bound of linear moving mass rail
S	surface area of an arbitrary blade element on the samara
$s(t)$	moving mass position function
T_P	period of the samara precession cycle
T_ϕ	period of the samara autorotational cycle
T_1	Case 2 and Case 3: time to ramp to rail upper bound of $s(t)$ function
T_2	Case 2 and Case 3: time to ramp to final position of $s(t)$ function
t_1	time trigger for moving mass function
t_2	Case 2 and Case 3: trigger time for transition to final $s(t)$ position
$\boldsymbol{U}_\infty$	relative free-stream wind velocity experienced by the wing
$\boldsymbol{v}_O$	inertial velocity vector of the fixed body origin Q
$(\dot{\boldsymbol{v}}_O)_r$	absolute acceleration relative to a rotating fixed body reference frame
v_x	inertial velocity in the *X*-direction
v_y	inertial velocity in the *Y*-direction
v_z	inertial velocity in the *Z*-direction
w	width of the samara
x	inertial position in the *X*-direction
X_b	*x* component of the fixed body reference frame
X_i	*x* component of the inertial reference frame
y	inertial position in the *Y*-direction
$,Y_b$	*y* component of the fixed body reference frame
Y_i	*y* component of the inertial reference frame
z	inertial position in the *Z*-direction
Z_b	*z* component of the fixed body reference frame

Z_i	z component of the inertial reference frame
α	samara angle of attack
θ	samara coning angle
ϑ	samara pitch angle (additive inverse of coning angle)
$\boldsymbol{\rho}$	position vector with respect to fixed body origin
$\boldsymbol{\rho}^{QC}$ or $\boldsymbol{\rho}_C$	fixed body position vector from fixed body origin to center of mass
$\boldsymbol{\rho}_P$	fixed body position of a blade element at point P with respect to Q
ρ_{air}	air density
ρ_x	distance of c.m. from the fixed body origin along the X_b-axis
$(\dot{\rho}_x)_r$	the change in position of the c.m. with respect to time as seen in $\mathcal{F}_b$
ϕ	samara angle of revolution (yaw angle)
ψ	Samara Roll Angle
$\boldsymbol{\omega}$	samara angular velocity

Chapter 1. Introduction

Nature has often been used as a source of inspiration for dynamics. The simple yet elegant design of the single-winged samara seed has been theorized as a form of evolution that has enabled the distribution of large seeds to greater distances with prevalent wind conditions [1] [2] [3] [4]. Some of the key advantageous characteristics of this design include a steady autorotating helical motion that slows the rate of vertical descent and robust auto-rotational stability in the presence of wind disturbance [5]. Figure 1-1 provides a visualization of a samara seed, which includes both (a) a simple still frame image as well as (b) a dynamic view of the samara in a helical spiral descent. The basic design of the samara consists of the large seed located at one end of the design, which is attached to a thin single wing. In general, the seed component of the design contains a much larger portion of the total mass compared to the relatively less dense wing, which leads to an asymmetric mass distribution across the overall design. The terms leading edge and trail edge are often used to distinguish between the edge of the wing that leads the autorotation.

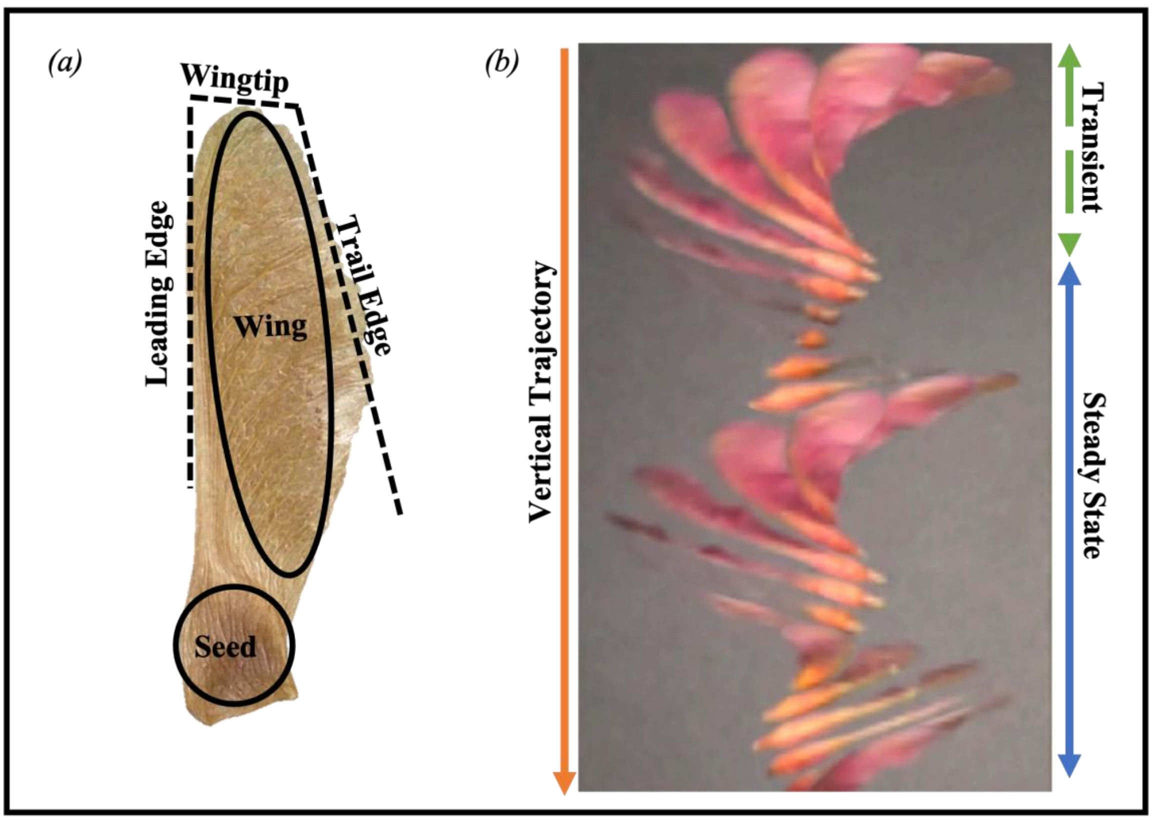

Figure 1-1. Visualizations of a samara seed. (a) Still frame of a Norway Maple seed (Acer platanoides) [6]. *(b) Samara seed helical spiral decent trajectory* [2].

A biomimetic samara vehicle design could have a variety of immediate practical applications. Leveraging wind dispersal, a large amount of inexpensive small samara-like sensors could be released to efficiently establish a distributed network over a large area [6] [7]. Fields that are researching sensor development that could leverage the samara distribution method include precision meteorology and atmospheric physics [8] [9] [10], wildfire management [11] [12], air quality [13] [14], water quality [15], agricultural management [16] [17], and potentially exploration of other planetary surfaces [18] [19]. Alternatively, scaled to a larger size, the samara seed design could also be used as a method of package delivery for humanitarian aid or disaster relief. For instance, a company called Five Forces leveraged the samara concept for an airdrop delivery system to deliver critical supplies following an earthquake [20] [21].

Understanding the dynamics of the samara is critically important for design optimization as well as control implementation. Past design and development work of biomimetic samara inspired vehicles have explored control features such as wing flaps, wingtip rudders, and propellers [22] [23] [24] [25] [26] [27] [28] [29] [30] [31] [32]; however, moving mass control (MMC) has never been investigated. Considering that mass distribution [33] and center of gravity [34] have been found to have significant impact on samara dynamics, MMC could be an effective means to control a samara-inspired vehicle.

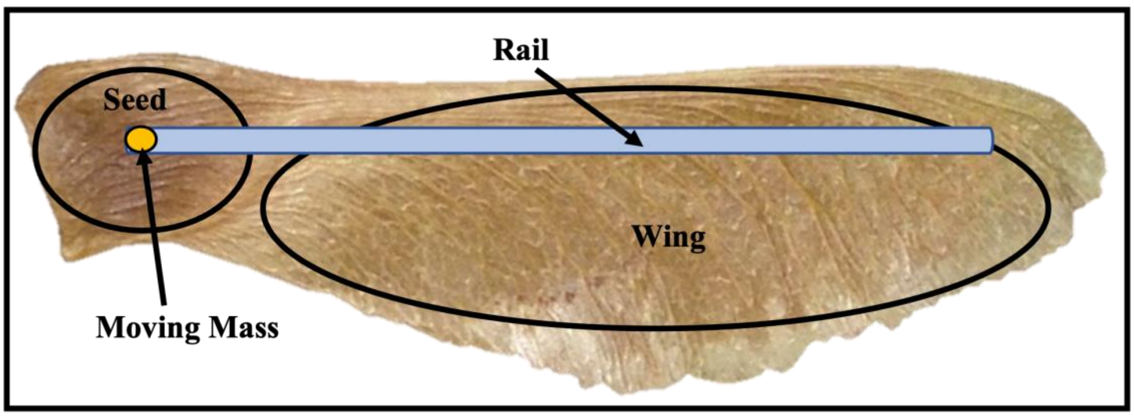

Figure 1-2. Example concept of MMC applied to a samara seed design using a Norway Maple seed (Acer platanoides) [6] *as the representative samara.*

This paper establishes a dynamic model of a samara-inspired vehicle with a single moving mass on a linear rail and evaluates whether a moving mass actuator is a viable option for control that could be considered in future work. The paper is organized as follows: Chapter 2, Literature Review; Chapter 3, Dynamics Model Overview; Chapter 4, Results; Chapter 5, Discussion of Engineering Application; and, Chapter 6, Conclusion.

Chapter 2. Review of Literature

While the study of the free-falling samara seed is not a new area of research, it continues to be an area of interest to academic researchers and technologists alike. Documented literature studying the autorotating wing extends back into the 19th century with some experimental studies [35]. In 1973, Norberg published an influential study characterizing the stability behavior of the samara based on experimental analysis [36]. Over the next several decades, extensive work has been published further investigating and qualifying samara dynamics. In this section, the following areas of literature will be reviewed: (1) the samara studies since Norberg's seminal work, (2) biomimetic samara vehicles that have either been designed or developed, and (3) a brief review of moving mass literature that influenced this project.

2.1. Samara Dynamics Studies

Generally, samara studies can be divided into experimental studies and theoretical studies. The theoretical studies can be further divided based on the theory supporting the analysis of the associated study. Depending on the samara characteristic that is being evaluated will determine which theory is most fitting to use, and in some cases, researchers have found ways to create hybrid approaches, combining different theories and approaches to achieve desired results.

The theories can be generally grouped into the following two categories: (1) the physics of the samara behavior itself and (2) the physics of the fluid dynamics in response to the samara behavior. Regarding the physics of the samara behavior itself, the three different theories that have been leveraged throughout the literature are Momentum Theory, Blade Element Theory, and Blade Element-Momentum Theory. For any of the theories or approaches associated with the fluid dynamics surrounding the samara, computation fluid dynamics (CFD) or other numerical simulation approaches were used.

2.1.1. Experimental Studies

Experimental studies have provided key insight into a variety of samara characteristics that have been correlated with the samara dynamic behavior. The different samara characteristics that have been studied include the effects of wind dispersal [6] [37] [38] [39], the precession cycle [40], the wing geometry [4] [41], the morphology [42] [43], the mass distribution [33], the pitch and coning angles [44], the initial conditions (i.e., attitude [45] and inertial velocity [46]). Recent studies have leveraged particle image velocimetry (PIV) for areas including flow structures induced by free-falling spin flight [47] and wingtip vortices [48] as well as velocity fields of the flow around the samara [49].

2.1.2. Momentum Theory

Momentum theory, also known as actuator disk theory, examines the change in momentum of the airflow as it passes through the plane of the rotation, typically visualized as a virtual disk [50]. Originally developed for spinning rotors, the theory assumes an infinite number of blades attached to the rotor that can be represented as an actuator disk [22]. As the simplest of the rotary theories, it is useful for initial performance estimates. The momentum theory can address many of the basic aspects of performance with low computational burden, including thrust and average velocity. However, because the dynamics are modeled as a disc, the theory does not provide a physical concept that could explain the nonuniformities of downwash velocities or any insight into rotor characteristics as a ratio to the blade area, blade airfoil characteristics, or tip speed values [51].

As the first analytical study of samara behavior, Norberg leveraged momentum theory [36]. Other studies leveraged this theory for the following purposes: terminal velocity calculations [39], back-end calculations from empirical study to find induced velocity [48], and dynamic gust response and post gust acceleration [52]. Other work combined momentum theory with numerical simulation [53].

2.1.3. Blade Element Theory (BET)

Blade element theory (BET) divides the blade into a discrete number of thin strips (elements) along the span of the wing. The aerodynamic loads (lift and drag) of each element are calculated based on its angle of attack and local velocity, then integrated along the span [50] [54]. This theory generally provides accurate local aerodynamic load estimates, which makes this method better than momentum theory for detailed blade design. Because the blade elements are viewed independently in the model, the induced inflow velocity cannot be determined with this method [54].

BET has been used multiple times in literature to model the dynamic behavior of the samara. Most recently, it was used to model the steady-state descent and rotation of the maple-inspired rotochute [55]. Separately, a biomimetic autorotating aerial vehicle known as the samara autorotating wing (SAW) used BET [56] [57]. Furthermore, BET defined the forces and moments used in the reduced-order model of the samara [1] [2] [3]. Because the reduced-order model was heavily leveraged for the dynamic model derived in Chapter 3 and compared to in Chapter 4, BET is the chosen theory used in this report.

2.1.4. Blade Element-Momentum Theory (BEMT)

Blade Element-Momentum Theory (BEMT) is an attempt to address the limitations of the previous two theories by combining the detailed analysis of BET with the overall flow dynamics calculated by the momentum theory [50] [54]. BEMT is more complex than either of the two previously mentioned theories but is still a relatively simple method that yields a relatively low computational burden compared to many numerical simulation approaches. As such, this theory is appealing for rapid design iterations since it provides the fastest and most robust performance estimations out of the three analytical approaches presented thus far. One significant limitation to BEMT is that it cannot account for instantaneous flow changes, which limits its ability to model aeroelastic and some airload problems due to variations of forces and moments with time [54]. As is the case with all three of the theories discussed thus far, this theory is inadequate for calculating complex three-dimensional fluid effects, which is why a significant number of studies leveraged computational fluid dynamics and other numerical simulation techniques as discussed in the next section.

In terms of the simpler analytical rotary theories discussed thus far, BEMT is found to be the most used. The first six degree of freedom dynamics model for the samara used BEMT in the workflow [58] [59] [60]. A separate study used BEMT to determine limits of samara performance [61]. Some of the different biomimetic vehicles used BEMT in the dynamic modeling and analysis, including the Guided Samara [22], the maple-inspired rotochute, and a monocopter (specifically looking at lateral behavior) [55]. Other work combined BEMT with numerical simulation to improve accuracy of induced flow velocity calculations with numerically simulated lift and drag coefficients [62].

2.1.5. Computational Fluid Dynamics (CFD) / Numerical Simulation

To better understand the flow of the air around the samara and the impact the flow has on the samara behavior, numerical simulation approaches have frequently been used in literature. The most notable theory that has been identified is the Leading Edge Vortex theory, which has shown to increase both lift and drag of the samara [53] [63] [49] [64] [65]. Vortex theory provides the basis for investigating the three-dimensional vortical behavior of the flow field induced by a rotor [66]. Using CFD to model the vortices and some other characteristics, other research has modeled the samara as a wind turbine to analyze performance and compared the analysis to experimental testing [67]. Other key features that were evaluated using numerical simulation methods include the effects of scaling the size of the samara [68], the samara center of gravity [34], Reynolds number [69] [70], and wing loading on aerodynamic characteristics [71].

2.2. Biomimetic Samara Vehicles

Over the past twenty years, an increasing number of biomimetic vehicles have been designed and developed. The first two that have been documented are the Guided Samara and the Lockheed Martin Samarai, both of which were prototyped in the 2006 to 2008 timeframe. The Guided Samara was a monocopter using wing flaps and a wingtip rudder for control [22]. The Samarai was part of a Defense Advanced Research Projects (DARPA) Nano Air Vehicle (NAV) program and is a biomimetic single-winged unmanned aerial vehicle (UAV) that was designed with a thrust nozzle at the wingtip and pitch actuator flaps along the span of the wing [23] [24] [25]. In 2008, a monocopter was developed using a fly-by-wire control that leveraged two actuators: one motorized propeller that is opposite the wing and a separate wing flap actuator that folds in parallel with the center chord of the wing [26]. Then in 2010, a few different designs of samara NAV were developed using two sources of control, a servo propeller at the end of a counterbalance arm from the wing as one source of control and a tail flap actuator perpendicular to the wing as a second source of control [27]. These two controls were used to control the pitch and heave [28].

In 2019, a research team started designing and prototyping a series of vehicles in a "samara autorotating wing (SAW)" group of vehicles, which used one actuator on the wing to change the angle of attack [29] [56]. The same research team proceeded to develop modified versions of this design to include the motorized SAW (mSAW) in 2020

[57] and the diving SAW (dSAW) in 2022 [30]. The mSAW replaced the actuating flap on the wing with a motorized propeller for control [57]. The dSAW was designed with two modes allowing for a precision drop: an autorotating mode and a dive mode. A spanwise actuator folds the wing to transition between modes [30].

Separately in 2021, a foldable single actuator monocopter (F-SAM) was designed with a motor propeller on the leading edge of the wing near the wingtip that was used to control the vehicle [31]. And, most recently in 2025, a maple seed inspired single actuator monocopter was developed to optimized flight endurance, which was designed with a motor propeller on the leading edge of the wing near the wingtip [32]. Figure 2-1 shows a variety of example designs and prototypes of the samara-inspired vehicles discussed in this section.

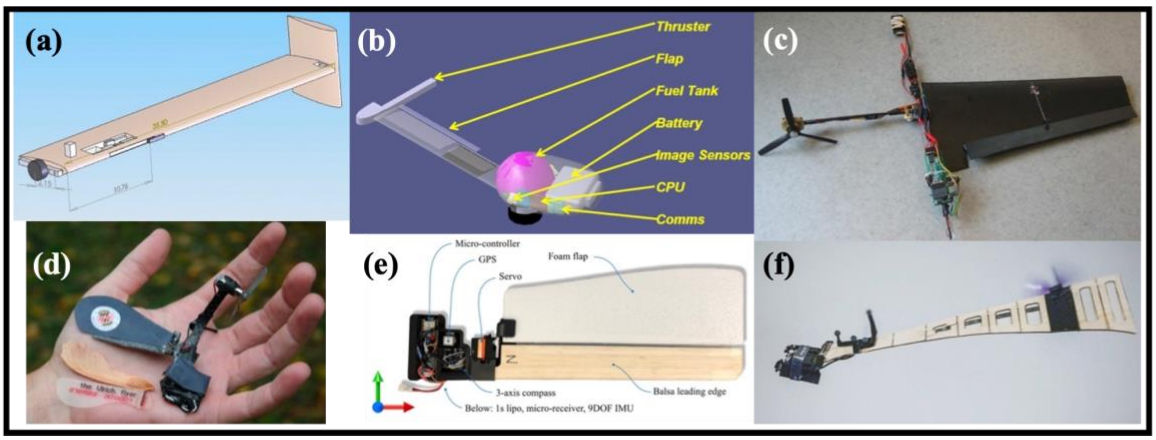

Figure 2-1. Examples of biomimetic samara-inspired vehicles: (a) Guided Samara design [22]*; (b) Samarai design* [23]*; (c) Fly-by-Wire Monocopter* [26]*; (d) Smallest robotic samara NAV developed* [41]*; (e) dSAW* [30]*; and, (f) F-SAM* [31].

In addition to the previously mentioned vehicles that were designed with control in mind, several biomimetic vehicles were developed without actuators. The first instance found in literature was in 2015 where biomimetic sensors were designed and prototyped with the goal of them potentially serving a variety of applications [7]. In 2021, a study was performed to compare the dynamics of 3D printed samara seeds with natural samara seeds [6]. In 2022, a samara inspired satellite design in the CanSat Competition was released at a 650-725m altitude using a UAV. The initial release was with a parachute containing two payloads, both resembling samaras. The first payload was released at 500m and second at 400m [72]. And, most recently in 2026, a paper was published documenting a maple-seed rotochute design [55].

2.3. Moving Mass / Time-Varying Dynamics

Using a moving mass as a control mechanism, often called moving mass control (MMC), for control of biomimetic samara-inspired vehicles or monocopters is a concept that has not been documented in literature despite previous research showing that mass distribution [33] and center of gravity [34] have significant impacts on the dynamics of the falling samara. Despite the lack of literature associated with samaras, the use of

MMC has been around for decades, having been used in domain areas such as fixed wing flight [73] [74], quadcopter UAVs [75], stratospheric airships [76], and most recently hypersonic vehicles [77]. These examples are all axisymmetric and non-spinning vehicles that use linear rails to control roll and pitch.

The only example MMC vehicle design with an angular rate loop spinning feature that could be found in literature is a ballistic reentry vehicle design [78] [79] [80]. One of the example designs utilized a linear rail set at an angle along the trajectory to allow the rail to freely rotate. As will be discussed in greater detail in Chapter 3, although the samara physical design is very flat, a rail that runs along the span of the samara wing would create a similar angled rail when viewing the rail in the context of the cone created by the dynamic samara behavior. Figure 2-2 depicts the example MMC design of a reentry vehicle with an angular rate loop spinning feature that was used for the inspiration of the moving mass feature discussed throughout the remainder of this report.

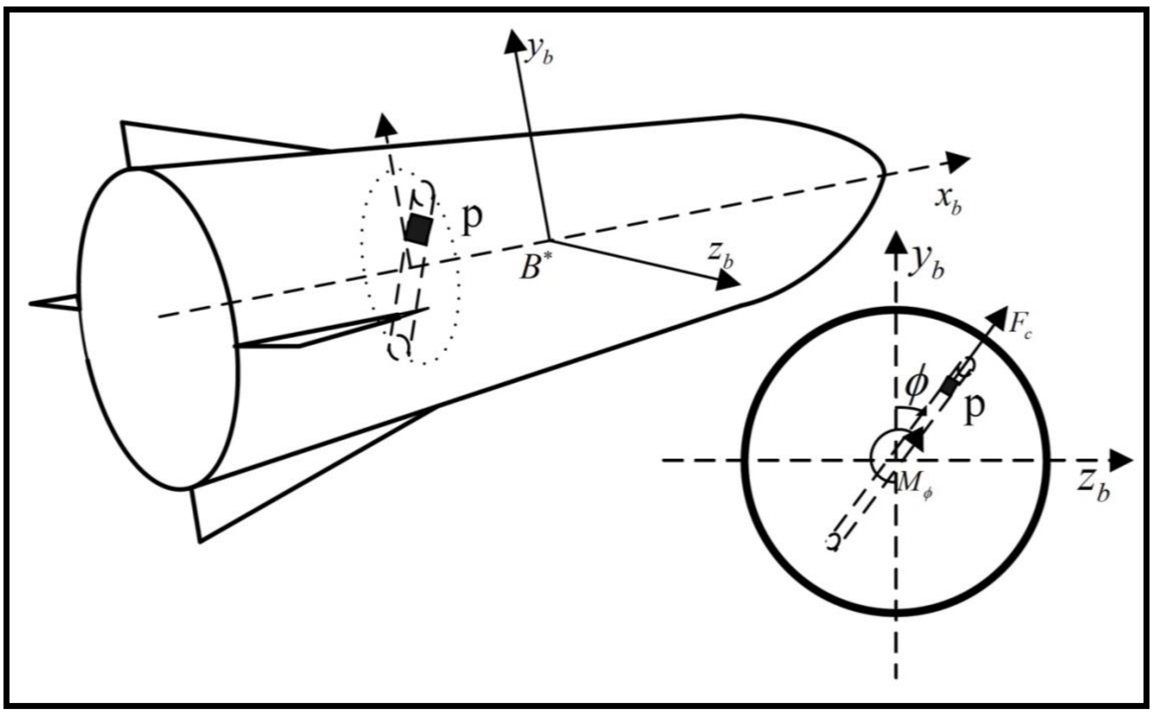

Figure 2-2. Example vehicle design with an angular rate loop spinning feature leveraging MMC [78].

Chapter 3. Dynamics Model Overview

The dynamics model derived and implemented in this report is a time-varying triple-mass rigid body model with six degrees of freedom. To define the forces and applied moments, blade element theory (BET) is chosen. While BET assumes negligible spanwise flow, which is a generally valid assumption for the steady state phase of flight, there will be increased error with the initial transient phase of the trajectory. In a benign environment, the transient phase of a samara seed is relatively quick before transitioning to steady state descent, so the BET assumption should have minimal impact on the modeling of the overall trajectory in this environment. If a wind gust profile is introduced, this assumption would likely have more significant impact on the samara model since the gusts would likely cause the samara to leave its steady state phase and repeat the transient phase throughout flight. Because the objective of this work is to develop an intuitive understanding of whether a moving mass could be a viable approach to controlling a samara-inspired vehicle, BET was determined to be a sufficient approach. This overview will first review the reference frame and equations of motion used followed by an overview of the moments of inertia and aerodynamic force calculations.

3.1. Reference Frame and Equations of Motions

The reference frames used for this model are chosen to align with those used by McConnell and Das [1] [2] [3]. This choice was intentionally made so that the model defined in this report could be compared against the results achieved by McConnell and Das.

As depicted in Figure 3-1(a), two coordinate systems are defined to describe the wing motion. The inertial reference frame, $\mathcal{F}_i = \{X_i, Y_i, Z_i\}$, with inertial origin O is an earth fixed reference frame where the Z_i axis is pointed upward in the negative direction of gravity from the Earth Center to the initial position of the samara seed. The X_i and Y_i axes form a plane orthogonal to the Z_i axis. The unit vectors for $\mathcal{F}_i$ are $\{\hat{e}_x, \hat{e}_y, \hat{e}_z\}$, where the subscripts relate to the respective axes.

The second frame is a fixed body reference frame, $\mathcal{F}_b = \{X_b, Y_b, Z_b\}$. The origin Q is located at the center of mass of the wing's seed, depicted by the darker shaded green located at the base of the wing in Figure 3-1(a). The X_b and Y_b axes are in plane with the wing of the samara where the X_b axis is parallel to the span of the samara wing. The Z_b axis is orthogonal to the other two axes. The unit vectors for $\mathcal{F}_b$ are $\{\hat{b}_x, \hat{b}_y, \hat{b}_z\}$, where the subscripts relate to the respective axes.

Figure 3-1(b) depicts the angular rotation sequence. Utilizing the commonly used Right Hand Rule, three Euler angles, ϕ, ϑ, and ψ, are used to transform the inertial reference frame $\{X_i, Y_i, Z_i\}$ to the fixed body reference frame through the sequence of reference frames, $\mathcal{F}_i \rightarrow \mathcal{F}_{i'} \rightarrow \mathcal{F}_{i''} \rightarrow \mathcal{F}_b$, where i represents the inertial frame, b represents the fixed body frame, and i' and i'' represent the intermediate reference frames between $\mathcal{F}_i$

and $\mathcal{F}_b$. The first rotation is about the Z-axis, followed by a "pitch" rotation ϑ about the new Y-axis ($Y_{i'}$), and the third rotation is a "yaw" rotation ψ about the third axis ($X_{i''}$).

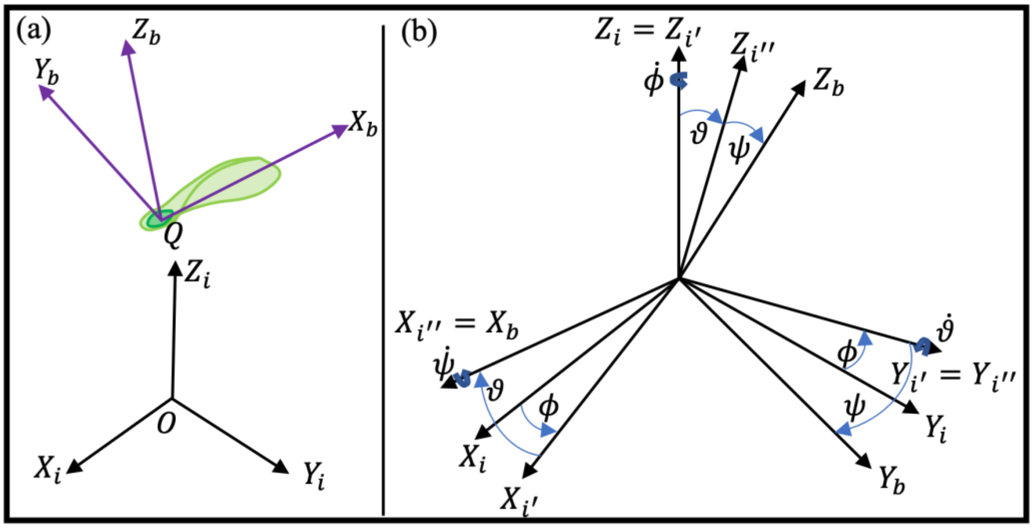

Figure 3-1. (a) Depiction of the coordinate systems used to describe the samara dynamics. (b) Euler transformation from the inertial reference frame to the fixed body reference frame.

Once the samara achieves stable motion, it creates a cone-like behavior from its autorotating motion [36]. This coning behavior is a defining characteristic of the samara motion. As seen in Figure 3-2, the samara is expected to "pitch down" at a negative ϑ angle to create the coning behavior. Since the coning angle is of particular interest in the design of the samara, a new angle θ is defined to represent the coning angle, where $\vartheta = -\theta$. This technique of defining the coning angle was implicitly used in [1] [2] [3] to generate their equations of motion.

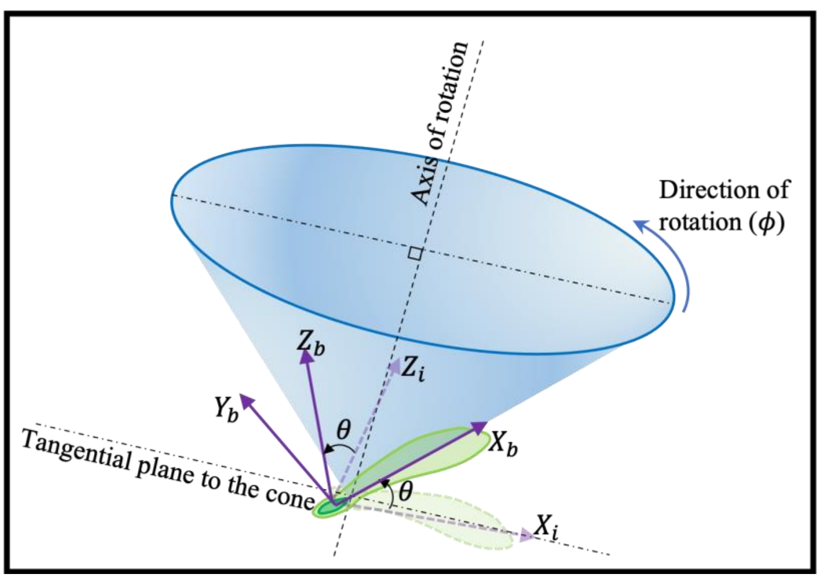

Figure 3-2. Depiction of samara conical motion [36].

Using a *Z-Y-X* Rotation Matrix, which proves to be consistent with what was used by McConnell and Das [1] [2] [3], Equation (3-1) defines the rotation matrix that relates $\mathcal{F}_i$ to $\mathcal{F}_b$. Supporting calculations for deriving the rotation matrix are provided in Appendix A.

$$\begin{bmatrix} \hat{e}_x \\ \hat{e}_y \\ \hat{e}_z \end{bmatrix} = \begin{bmatrix} \cos\phi\cos\theta & -\sin\phi\cos\psi - \cos\phi\sin\theta\sin\psi & \sin\phi\sin\psi - \cos\phi\sin\theta\cos\psi \\ \sin\phi\cos\theta & \cos\phi\cos\psi - \sin\phi\sin\theta\sin\psi & -\cos\phi\sin\psi - \sin\phi\sin\theta\cos\psi \\ \sin\theta & \cos\theta\sin\psi & \cos\theta\cos\psi \end{bmatrix} \begin{bmatrix} \hat{b}_x \\ \hat{b}_y \\ \hat{b}_z \end{bmatrix} \tag{3-1}$$

Equation (3-2) defines the six degrees of freedom (DoF) equations of motion used to define the dynamic behavior of the model, three DoF rotational equations and three DoF translational equations. Appendix B defines the angular velocity $\boldsymbol{\omega}$ and angular acceleration $\dot{\boldsymbol{\omega}}$ in terms of the Euler angles defined earlier in this chapter. Appendix D and Appendix E derive the equations in (3-2) as well as implementable versions of these equations that are used in the model.

$$\begin{gathered} M_x = I_{xx}\dot{\omega}_x + \left(I_{zz} - I_{yy}\right)\omega_y\omega_z + \dot{I}_{xx}\omega_x \\ M_y = \left(I_{yy} + m\rho_x^2\right)\dot{\omega}_y + \left(I_{xx} - I_{zz} - m\rho_x^2\right)\omega_x\omega_z + \left(\dot{I}_{yy} + m\rho_x(\dot{\rho}_x)_r\right)\omega_y \\ M_z = \left(I_{zz} + m\rho_x^2\right)\dot{\omega}_z + \left(I_{yy} - I_{xx} + m\rho_x^2\right)\omega_x\omega_y + \left(\dot{I}_{zz} + m\rho_x(\dot{\rho}_x)_r\right)\omega_z \\ \dot{v}_x = F_{x_i}/m \\ \dot{v}_y = F_{y_i}/m \\ \dot{v}_z = \left(-F_{g_i} + F_{z_i}\right)/m \end{gathered} \tag{3-2}$$

In these equations, $\{M_x, M_y, M_z\}$ represent the components of the applied angular moment about the overall samara center of mass, $\{I_{xx}, I_{yy}, I_{zz}\}$ represent the components of the moments of inertia, ρ_x defines the distance of the center of mass from the fixed body origin Q along the fixed body *x*-axis, $(\dot{\rho}_x)_r$ represents the change in position of the samara center of mass with respect to time as seen in the fixed body reference frame, $\{F_{x_i}, F_{y_i}, F_{z_i}\}$ represent the components of the generalized aerodynamic forces acting on the samara seed as seen from the inertial reference frame, $\{v_x, v_y, v_z\}$ represent the components of the velocity of the samara fixed body origin Q with respect to the inertial reference frame, m represents the total mass of the samara seed, and F_{g_i} represents the gravitational force. Throughout the remainder of this chapter, these various terms will be mathematically defined.

3.2. Moments of Inertia

To calculate the moments of inertia more easily for the dynamic model, a simplified model of the samara is introduced, using a combination of well-defined homogenous geometric bodies. The relatively large wing is modeled as a thin rectangular plate and the seed at the base of the wing is modeled as a thin rod. The moving mass is treated as a particle mass. While there are distinct differences between the modeled samara and the typical geometry of the samara, past research has shown that the asymmetric mass distribution is a larger factor than geometry in causing the observed helical motion [4] [42]. Figure 3-3 depicts the simplified model of the samara overlaying a more representative geometry of the samara seed in the fixed body reference frame that was previously defined.

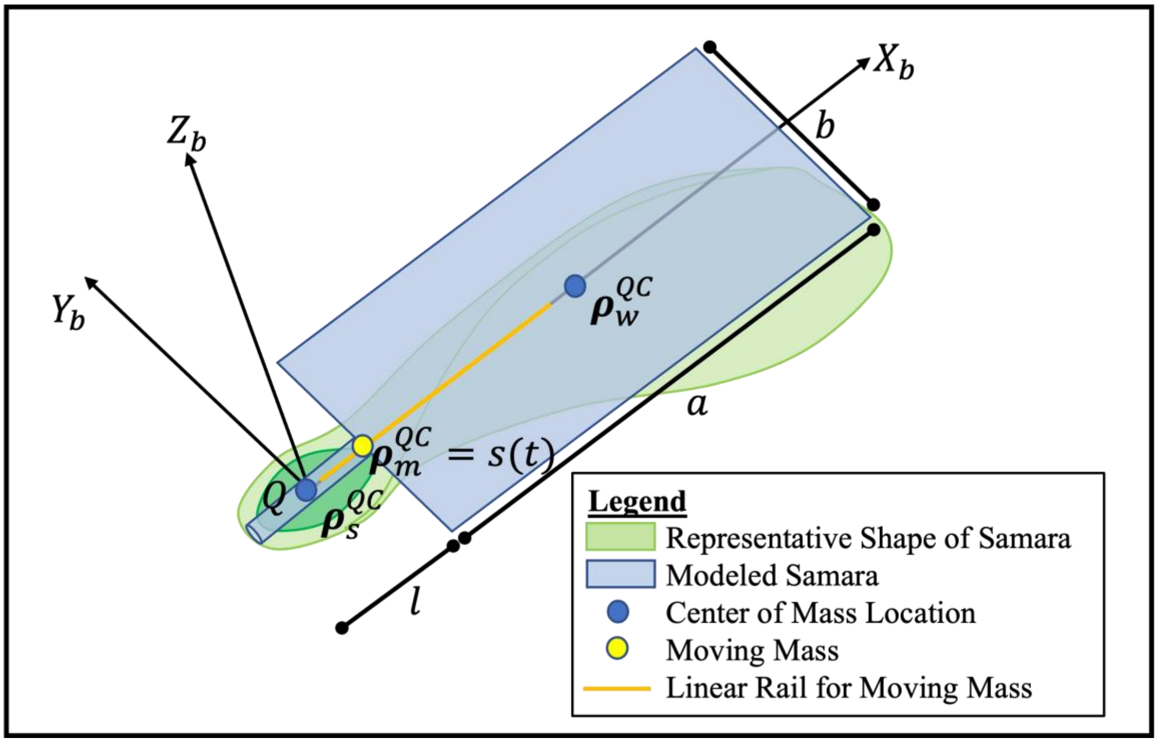

Figure 3-3. Model of the autorotating vehicle overlayed on an example samara geometry.

The parameters used in this diagram are sufficient to define the geometry of the model. The wing is defined by length a and width b. The seed is defined by length l. The vector $\boldsymbol{\rho}$ is used to denote the position of an arbitrary point with respect to Q in the fixed body reference frame. All three components to this model have independent centers of mass depicted by the fixed body position vector $\boldsymbol{\rho}^{QC}$ from the fixed body origin Q to the respective center of mass. The subscripts are used to define which center of mass is associated with which component of the model, where s represents the seed, w represents the wing, and m represents the moving mass. Since this model considers a mass that moves with respect to time, the function $s(t)$ is introduced and is equal to the $\boldsymbol{\rho}_m^{QC}$.

From the derivation provided in Appendix C, the moments of inertia can be defined in Equation (3-8). Like the center of mass notation, the mass m of the associated component is annotated with the subscripts s, w, and m defined in the previous paragraph. The subscript "$comp$" is used to annotate the full composite model, and the use of this subscript is to clearly distinguish the total mass from the component masses.

The "$comp$" subscript notation is removed in other areas of this report since the mass used in other equations only refers to the total mass of the samara.

$$I_{xx} = \frac{m_w b^2}{12}$$

$$I_{yy} = \frac{m_s l^2}{12} + m_w\left(\frac{a^2}{12} + \left(\frac{l+a}{2}\right)^2\right) + m_m[s(t)]^2 + \frac{1}{m_{comp}}\left(\frac{m_w(l+a)}{2} + m_m s(t)\right)^2$$

$$I_{zz} = \frac{m_s l^2}{12} + m_w\left(\frac{a^2+b^2}{12} + \left(\frac{l+a}{2}\right)^2\right) + m_m[s(t)]^2 + \frac{1}{m_{comp}}\left(\frac{m_w(l+a)}{2} + m_m s(t)\right)^2 \tag{3-3}$$

From Equation (3-8), the first order time derivatives of moments of inertia can be found in Equation (3-9).

$$\begin{aligned} \dot{I}_{xx} &= 0 \\ \dot{I}_{yy} &= 2m_m s(t)s'(t) + \frac{2m_m}{m_{comp}}\left(\frac{m_w(l+a)}{2} + m_m s(t)\right)s'(t) \\ \dot{I}_{zz} &= 2m_m s(t)s'(t) + \frac{2m_m}{m_{comp}}\left(\frac{m_w(l+a)}{2} + m_m s(t)\right)s'(t) \end{aligned} \tag{3-4}$$

3.3. Calculating Aerodynamic Forces with BET

To determine the aerodynamic forces and the applied angular moments used in the equations of motion, the model uses BET to define the dynamic behavior of the samara. Figure 3-4 shows the free body diagrams depicting the different forces acting on the samara seed. In these diagrams, F_{x_b}, F_{y_b}, and $F_{z_b}$are the components of the net aerodynamic forces, in the respective coordinate directions, (X_b, Y_b, Z_b), as annotated by the subscripts. The drag force and lift force are also defined as D and L, respectively. Across the span of the samara wing, the net forces vary by every change in $\boldsymbol{\rho}$, which is used to define the blade element, $d\boldsymbol{\rho}$. As such, for every $d\boldsymbol{\rho}$, there are local aerodynamic forces dF_{x_b}, dF_{y_b},dF_{z_b}, dD, and dL. As an input to the blade element definition, the width of the wing as a function of $\boldsymbol{\rho}$ is defined as $w(\boldsymbol{\rho})$. A few other parameters captured in the Figure 3-4 that also need to be defined are α which is the spanwise local angle of attack and $\boldsymbol{U}_\infty$ which is the relative freestream wind velocity experienced by the blade element $d\boldsymbol{\rho}$.

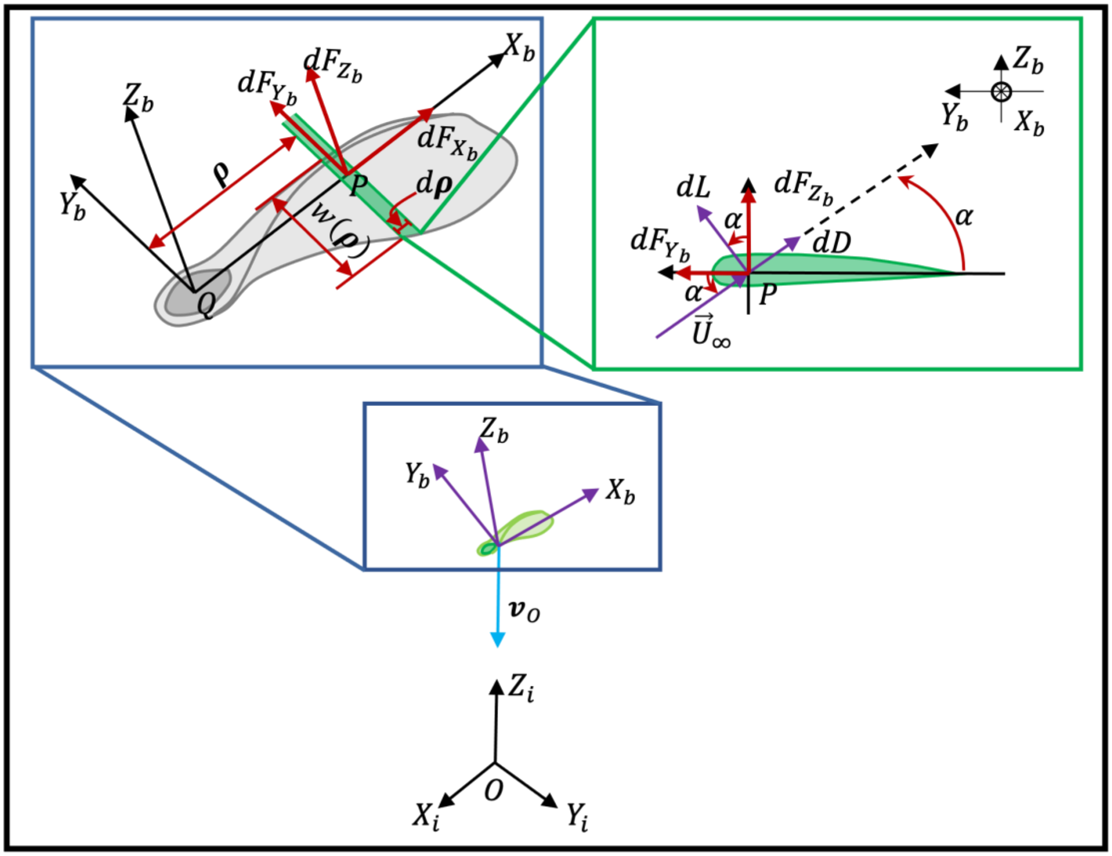

Figure 3-4. Free body diagram using BET to describe forces acting on the samara.

First, the position and velocity need to be defined for the samara. For this model, two positions are important: (1) the position of the samara fixed body reference frame origin Q relative to the inertial reference frame, denoted by $\boldsymbol{r}_O$, (2) the position at the blade element relative to the origin Q of the fixed body reference frame, denoted by $\boldsymbol{\rho}_P$. The difference in notation is used to clearly distinguish between the inertial and fixed body reference frames.

A general equation for the inertial velocity, $\boldsymbol{v}_O$, associated with $\boldsymbol{r}_O$ can be depicted as follows,

$$\vec{\boldsymbol{v}}_O = v_x\hat{e}_x + v_y\hat{e}_y + v_z\hat{e}_z \tag{3-5}$$

where $\{v_x, v_y, v_z\}$ are the inertial velocity components and $\{\hat{e}_x, \hat{e}_y, \hat{e}_z\}$ are the inertial frame unit vectors.

Using the rotation matrix relationship defined in Equation (3-1), $\boldsymbol{v}_O$ can be defined in the fixed body reference frame with Equation (3-11).

$$
\begin{aligned}
\vec{\boldsymbol{v}}_O = v_x\big(&\cos\phi\cos\theta\,\hat{b}_x + (-\sin\phi\cos\psi - \cos\phi\sin\theta\sin\psi)\hat{b}_y \\
&+ (\sin\phi\sin\psi - \cos\phi\sin\theta\cos\psi)\hat{b}_z\big) \\
&+ v_y\big(\sin\phi\cos\theta\,\hat{b}_x + (\cos\phi\cos\psi - \sin\phi\sin\theta\sin\psi)\hat{b}_y \\
&+ (-\cos\phi\sin\psi - \sin\phi\sin\theta\cos\psi)\hat{b}_z\,\big) \\
&+ v_z\big(\sin\theta\,\hat{b}_x + \cos\theta\sin\psi\,\hat{b}_y + \cos\theta\cos\psi\,\hat{b}_z\big)
\end{aligned}
\tag{3-6}
$$

Leveraging the definition for velocity in a non-inertial frame [81], the absolute velocity of the samara at an arbitrary blade element relative to the moving fixed body reference frame can be defined by Equation (3-12).

$$
\boldsymbol{v}_P = \boldsymbol{v}_O + (\dot{\boldsymbol{\rho}}_P)_r + (\boldsymbol{\omega} \times\ \boldsymbol{\rho}_P)
\tag{3-7}
$$

where $\boldsymbol{\rho}_P$ is the distance from the fixed body origin Q to an arbitrary blade element, $(\dot{\boldsymbol{\rho}}_P)_r$ is the rate of change of the blade element position with respect to the fixed body reference frame, and $\boldsymbol{\omega}$ is the angular velocity of the samara. Since the overall samara is a rigid body, the change in position of the blade element from Q is equal to 0, i.e., $(\dot{\boldsymbol{\rho}}_P)_r = 0$. Also, since the samara is relatively thin compared to its length, the distance of the blade element $\boldsymbol{\rho}_P$ is measured along the X_b-axis. Therefore, the Y_b and Z_b components of $\boldsymbol{\rho}_P$ can be approximated as zero and $(\boldsymbol{\omega} \times \boldsymbol{\rho}_P)$ can be calculated as follows,

$$
(\boldsymbol{\omega} \times \boldsymbol{\rho}_P) = \begin{vmatrix} \hat{b}_x & \hat{b}_y & \hat{b}_z \\ \omega_x & \omega_y & \omega_z \\ \rho_{P_x} & \rho_{P_y} & \rho_{P_z} \end{vmatrix} = \begin{vmatrix} \hat{b}_x & \hat{b}_y & \hat{b}_z \\ \omega_x & \omega_y & \omega_z \\ \rho_{P_x} & 0 & 0 \end{vmatrix} = \begin{bmatrix} 0 \\ \omega_z\rho_{P_x} \\ -\omega_y\rho_{P_x} \end{bmatrix}
\tag{3-8}
$$

Substituting Equations (3-11) and (3-13) back into Equation (3-12) yields Equation (3-14).

$$
\begin{aligned}
\vec{\boldsymbol{v}}_P = \big[v_x\big(&\cos\phi\cos\theta\,\hat{b}_x + (-\sin\phi\cos\psi - \cos\phi\sin\theta\sin\psi)\hat{b}_y \\
&+ (\sin\phi\sin\psi - \cos\phi\sin\theta\cos\psi)\hat{b}_z\big) \\
&+ v_y\big(\sin\phi\cos\theta\,\hat{b}_x + (\cos\phi\cos\psi - \sin\phi\sin\theta\sin\psi)\hat{b}_y \\
&+ (-\cos\phi\sin\psi - \sin\phi\sin\theta\cos\psi)\hat{b}_z\,\big) \\
&+ v_z\big(\sin\theta\,\hat{b}_x + \cos\theta\sin\psi\,\hat{b}_y + \cos\theta\cos\psi\,\hat{b}_z\big)\big] \\
&+ \big(\omega_z\rho_{P_x}\hat{b}_y - \omega_y\rho_{P_x}\hat{b}_z\big)
\end{aligned}
\tag{3-9}
$$

Using the angular velocity relationship derived in Appendix B, Equation (3-14) produces the following,

$$
\begin{aligned}
\vec{\boldsymbol{v}}_P = {} & v_x \cos\phi \cos\theta\, \hat{b}_x + v_x(-\sin\phi\cos\psi - \cos\phi\sin\theta\sin\psi)\hat{b}_y \\
& + (v_x \sin\phi\sin\psi - \cos\phi\sin\theta\cos\psi)\hat{b}_z + v_y \sin\phi\cos\theta\, \hat{b}_x \\
& + v_y(\cos\phi\cos\psi - \sin\phi\sin\theta\sin\psi)\hat{b}_y \\
& + v_y(-\cos\phi\sin\psi - \sin\phi\sin\theta\cos\psi)\hat{b}_z + v_z\sin\theta\, \hat{b}_x \\
& + v_z\cos\theta\sin\psi\, \hat{b}_y + v_z\cos\theta\cos\psi\, \hat{b}_z \\
& + \rho_{P_x}\big(\dot{\phi}\cos\theta\cos\psi + \dot{\theta}\sin\psi\big)\hat{b}_y \\
& - \rho_{P_x}\big(\dot{\phi}\cos\theta\sin\psi - \dot{\theta}\cos\psi\big)\hat{b}_z
\end{aligned}
\tag{3-10}
$$

Combining like terms in Equation (3-15) yields the following,

$$
\begin{aligned}
\vec{\boldsymbol{v}}_P = {} & \big(v_x\cos\phi\cos\theta + v_y\sin\phi\cos\theta + v_z\sin\theta\big)\hat{b}_x \\
& + \Big(v_x(-\sin\phi\cos\psi - \cos\phi\sin\theta\sin\psi) \\
& + v_y(\cos\phi\cos\psi - \sin\phi\sin\theta\sin\psi) + v_z\cos\theta\sin\psi \\
& + \rho_{P_x}\big(\dot{\phi}\cos\theta\cos\psi + \dot{\theta}\sin\psi\big)\Big)\,\hat{b}_y \\
& + \Big(v_x(\sin\phi\sin\psi - \cos\phi\sin\theta\cos\psi) \\
& + v_y(-\cos\phi\sin\psi - \sin\phi\sin\theta\cos\psi) + v_z\cos\theta\cos\psi \\
& - \rho_{P_x}\big(\dot{\phi}\cos\theta\sin\psi - \dot{\theta}\cos\psi\big)\Big)\,\hat{b}_z
\end{aligned}
\tag{3-11}
$$

Equation (3-17) introduce the general definitions of C_L and C_D, the lift and drag coefficients, respectively, as well as supporting definitions of dynamic pressure, q_∞, and the referenced surface area of an arbitrary blade element on a samara seed, S [82].

$$
\begin{aligned}
C_L &\equiv \frac{L}{q_\infty S} & C_D &\equiv \frac{D}{q_\infty S} \\
q_\infty &= \frac{1}{2}\rho_{air}\|\boldsymbol{U}_\infty\|^2 & S &= w\big(\rho_{P_x}\big)d\rho_{P_x}
\end{aligned}
\tag{3-12}
$$

In these definitions, ρ_{air} represents the local air density surrounding the samara seed, $\boldsymbol{U}_\infty$ is the relative wind velocity experienced by the blade element, $w\big(\rho_{P_x}\big)$ is the width of the blade element for a given ρ_{P_x}, and $d\rho_{P_x}$ is the incremental width of the given blade element.

Using the geometric relationships defined in Figure 3-4 along with the definitions shown in Equation (3-17), the local drag and lift are defined for an element along the samara blade in the following equations.

$$
\begin{aligned}
dL &= \frac{1}{2}\rho_{air}\|\boldsymbol{U}_\infty\|^2 C_L(\alpha) w\big(\rho_{P_x}\big)d\rho_{P_x} \\
dD &= \frac{1}{2}\rho_{air}\|\boldsymbol{U}_\infty\|^2 C_D(\alpha) w\big(\rho_{P_x}\big)d\rho_{P_x}
\end{aligned}
\tag{3-13}
$$

Assuming there is a benign environmental wind profile with negligible crosswind, negligible effects of leading-edge vortex (which couples blade elements), and negligible spanwise flow, $\boldsymbol{U}_\infty$ and α can be expressed by the following equations based on the geometric relationships defined in Figure 3-4,

$$\vec{\boldsymbol{U}}_\infty = -\left(v_{P_y}\hat{b}_y + v_{P_z}\hat{b}_z\right), \quad \tan\alpha = -\frac{v_{P_z}}{v_{P_y}} \tag{3-14}$$

Using the $\boldsymbol{v}_P$ definition from Equation (3-16), $\boldsymbol{U}_\infty$ can be expressed as follows,

$$\begin{aligned}\|\boldsymbol{U}_\infty\|^2 = \Big(-\Big(& v_x(-\sin\phi\cos\psi - \cos\phi\sin\theta\sin\psi) \\ &+ v_y(\cos\phi\cos\psi - \sin\phi\sin\theta\sin\psi) + v_z\cos\theta\sin\psi \\ &+ \rho_{P_x}(\dot{\phi}\cos\theta\cos\psi + \dot{\theta}\sin\psi)\Big)\Big)^2 \\ &+ \Big(-\Big(v_x(\sin\phi\sin\psi - \cos\phi\sin\theta\cos\psi) \\ &+ v_y(-\cos\phi\sin\psi - \sin\phi\sin\theta\cos\psi) + v_z\cos\theta\cos\psi \\ &- \rho_{P_x}(\dot{\phi}\cos\theta\sin\psi - \dot{\theta}\cos\psi)\Big)\Big)^2\end{aligned} \tag{3-15}$$

Equation (3-20) can then be simplified to the following,

$$\begin{aligned}\|\boldsymbol{U}_\infty\|^2 = v_x^2\sin^2\phi &- 2v_y\sin\phi\left(v_x\cos\phi + \rho_{P_x}\dot{\theta}\sin\theta\right) \\ &- 2v_z\sin\theta\cos\theta\left(v_x\cos\phi + v_y\sin\phi\right) \\ &- 2v_x\rho_{P_x}\left(\dot{\phi}\sin\phi\cos\theta + \dot{\theta}\cos\phi\sin\theta\right) \\ &+ \sin^2\theta\left(v_x\cos\phi + v_y\sin\phi\right)^2 + \left(v_y\cos\phi + \rho_{P_x}\dot{\phi}\cos\theta\right)^2 \\ &+ \left(\rho_{P_x}\dot{\theta} + v_z\cos\theta\right)^2\end{aligned} \tag{3-16}$$

While McConnell and Das simplified their model to only consider vertical translation in the Z_i-direction, their work can be used as a point of reference to build confidence that this extended derivation aligns with their findings. When the constraints $v_x = 0$, $v_y = 0$, and $\rho_{P_x} = 0$ are applied to Equation (3-21), the resulting Equation (3-22) shows to be consistent with the equation found in [1] [2] [3].

$$\|\boldsymbol{U}_\infty\|^2 = \rho_{P_x}^2\dot{\phi}^2\cos^2\theta + \left(\rho_{P_x}\dot{\theta} + v_z\cos\theta\right)^2 \tag{3-17}$$

Using the angle of attack relationship defined in Equation (3-19), the angle of attack of the samara can be found by the following,

$$\alpha = -\tan^{-1}\left(\frac{v_{P_z}}{v_{P_y}}\right) \tag{3-18}$$

Again, as a point of comparison, Substituting Equation (3-16) into Equation (3-23) and applying the assumptions in [1] [2] [3] ($\psi = \dot{\psi} \approx 0$), the following result shows to be consistent with what was found in [1] [2] [3],

$$\alpha = \tan^{-1}\left(\frac{-v_z \cos\theta - \rho_{P_x}\dot{\theta}}{\rho_{P_x}\dot{\phi}\cos\theta}\right) \tag{3-19}$$

In order to better compare the results from the expanded model described in this report to the results obtained by the McConnell and Das reduced order model, the method for calculating C_L, C_D and $w(\rho_{P_x})$ were replicated with what was used by McConnell and Das [1]. The model used by McConnell and Das implements a simple thin symmetric airfoil model in Equation (3-25) to find the associated lift and drag coefficients as functions of α, utilizing Equation (3-23).

$$\begin{gathered} C_L(\alpha) = 2\pi \sin\alpha \\ C_D(\alpha) = C_L(\alpha)\sin\alpha + C_{D_0} \end{gathered} \tag{3-20}$$

where the model introduces C_{D_0} as a tunable additional drag coefficient to numerically account for the effects of roughness, airfoil thickness, and the leading-edge vortex (LEV) phenomenon. While the equation is representative of potential flow without flow separation and thereby not the greatest representation of a LEV, McConnell and Das found the model to be comparable to experimental results in literature that had low Reynolds Number flow over small wings. Given a scenario where the Reynolds Number is greater, this model may see a divergence from experimental data [1] [2] [3]. An area of future research would be to apply more realistic lift and drag coefficient calculations incorporating the LEV effect into this model.

Now, using the same planform of the samara used in [1], Figure 3-5 defines the normalized width data across the span of the wing, which is used to determine $w(\rho_{p_x})$.

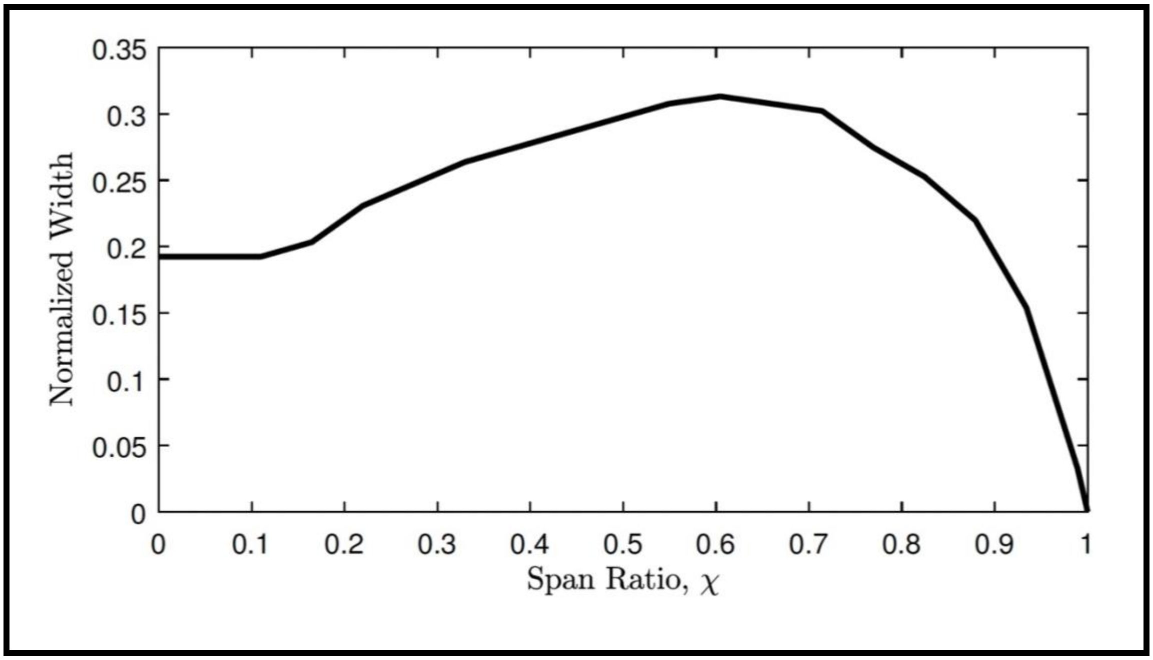

Figure 3-5. Normalized samara width data [1].

From Figure 3-4, the net blade element forces can be defined in the fixed body coordinate frame in the Y_b and Z_b directions as shown in Equation (3-26).

$$\begin{aligned} dF_{y_b} &= \sin(\alpha)\, dL - \cos(\alpha)\, dD \\ dF_{z_b} &= \cos(\alpha)\, dL + \sin(\alpha)\, dD \end{aligned} \tag{3-21}$$

Substituting Equation (3-18) into Equation (3-26), Equation (3-27) provides the simplified equation for the blade element aerodynamic forces.

$$\begin{aligned} dF_{y_b} &= \frac{1}{2}\rho_{air}\|\boldsymbol{U}_\infty\|^2\big(\sin(\alpha)\, C_L(\alpha) - \cos(\alpha)\, C_D(\alpha)\big)w\big(\rho_{P_x}\big)d\rho_{P_x} \\ dF_{z_b} &= \frac{1}{2}\rho_{air}\|\boldsymbol{U}_\infty\|^2\big(\cos(\alpha)\, C_L(\alpha) + \sin(\alpha)\, C_D(\alpha)\big)w\big(\rho_{P_x}\big)d\rho_{P_x} \end{aligned} \tag{3-22}$$

Leveraging the combination of equations found throughout this section, the net blade element forces defined in terms of the state variables can be integrated across the span of the wing to find the overall net forces F_{y_b} and F_{z_b}, as shown in the following equation.

$$F_{y_b} = \int_{r_0}^{r_f} dF_{y_b}, \qquad F_{z_b} = \int_{r_0}^{r_f} dF_{z_b} \tag{3-23}$$

where r_0 and r_f represent the initial and final distances from point Q, used as bounds of integration. As one of the simplifying assumptions used in [1] [2] [3], the effect of the blade element force along the blade span is neglected, thus $F_{x_b} \approx 0$, which is a typical assumption made with BET [54] [83] [84]. In an environment with a benign relative freestream wind velocity, this assumption has minimal impact on the model's performance; however, with the addition of turbulence or dynamically changing wind velocity, F_{x_b} would likely need to be added back into the model to align with experimental data.

Next, leveraging the definition of applied moment [81], the applied moments about the samara center of mass can be defined by the following equation.

$$\boldsymbol{M}_c = \sum_{i=1}^{N} \boldsymbol{\rho}_{P_i} \times dF_{b_i} \tag{3-24}$$

where $\boldsymbol{M}_C$ is the applied moment about the center of mass of the samara, dF_{b_i} is the local aerodynamic force of the samara blade element in the fixed body reference frame, N is the total number of blade elements used by the model, and i is the index determining which blade element is being referenced.

Since the distance of the blade element from the fixed body origin Q is taken along the X_b axis, $\rho_y = 0$ and $\rho_z = 0$. Along with the previous assumption made that $F_{x_b} \approx 0$ in a benign environment, the following applied moments at a given blade element, $\boldsymbol{dF}_i$, can be defined,

$$d\boldsymbol{M}_C = \begin{vmatrix} \hat{b}_x & \hat{b}_y & \hat{b}_z \\ \rho_{P_x} & 0 & 0 \\ 0 & dF_{y_b} & dF_{z_b} \end{vmatrix} = \begin{bmatrix} 0 \\ -\rho_{P_x} dF_{z_b} \\ \rho_{P_x} dF_{y_b} \end{bmatrix} \tag{3-25}$$

where $d\boldsymbol{M}_C$ is the local applied moment about the center of mass of a given blade element. Integrating the force across the span of the samara wing yields the following applied moments for the overall samara,

$$M_{y_b} = -\int_{r_0}^{r_f} \rho_{P_x} dF_{z_b}, \qquad M_{z_b} = \int_{r_0}^{r_f} \rho_{P_x} dF_{y_b} \tag{3-26}$$

Chapter 4. Results

Based on the dynamic model defined in Chapter 3, a MATLAB Simulink model was created to implement the model. The base structure of the model leveraged the Simulink model and supporting MATLAB functions that were used to implement the McConnell and Das reduced order model [1] [2] [3]. Results generated from the model include the following: (1) verification of the base dynamic model, (2) evaluation of the baseline model in a little greater detail, and (3) exploration of several case studies evaluating various time-varying moving mass functions. In general, the goal of the different case studies is to isolate specific features of the model in order to better understand how the specified feature impacts the overall behavior of the model. Thus, the initial conditions and the model parameters are left constant throughout the various case studies. The exception is that mass distribution between m_s and m_m, which is varied as part of the moving mass sizing studies.

Table 4-1 lists the initial conditions used throughout this study. For the duration used for the simulation scenarios, the initial conditions are relatively arbitrary. While prior work has found initial orientation [45] and initial velocity [46] to have a noticeable effect on how quickly the samara reaches steady-state autorotation, the impacts are on the time scale of microseconds. The initial position is set to the inertial origin so that inertial displacement over time is easier to determine.

Table 4-1. Initial conditions used for model verification and subsequent case studies.

Initial Conditions	**Values**
x_0	0 m
y_0	0 m
z_0	0 m
$v_{x,0}$	0 m/s
$v_{y,0}$	0 m/s
$v_{z,0}$	0 m/s
θ_0	0 deg
ϕ_0	0 rev
ψ_0	0 deg
$\dot{\theta}_0$	0 deg/s
$\dot{\phi}_0$	0 rev/s
$\dot{\psi}_0$	0 deg/s

Table 4-2 summarizes the parameters used for the baseline case as well as the subsequent case studies. The mass and geometry parameters were based on the Norway maple seed (*Acer platanoides*) empirically measured in [36]. Norberg calculated 15% of the total mass is in the samara wing. Regarding geometry, Norberg measured the total length of the seed, distance from center of mass to the wingtip normal to the axis of rotation, and the maximal width; from these measurements, l is calculated. The tunable drag coefficient C_{D_0} is the value that McConnell and Das calculated in their studies [1] [2] [3]. Lastly, the integration bounds r_0 and r_f are the same as what was used in [1]. For r_0, the increased thickness of the camber near to the seed has an inherently high angle of attack and a significant impact on the drag; by neglecting the thicker portion of the wing, the tuning parameter C_{D_0} can compensate for the neglected drag. For r_f, the upper bound needed to be truncated to account for tip loss [1].

Table 4-2. Model parameters used for baseline case and subsequent case studies.

Model Parameters	**Values**
r_0	$0.2R$ m $= 0.0070$ m
r_f	$0.9R$ m $= 0.0315$ m
m	0.00013 kg
m_s	$0.85m = 0.0001105$ kg
m_w	$0.15m = 0.0000195$ kg
m_m	0 kg
a	0.035 m
b	0.017 m
l	0.047 m $- 0.035$ m $= 0.012$ m
g	9.81 m/s^2
ρ_{air}	1.225 kg/m^3
C_{D_0}	0.126

4.1. Model Verification

To verify the model in this study, the simulated results are compared to the simulated results achieved by the McConnell and Das reduced order model as well as the empirical results from Norberg to which the McConnell and Das results were originally compared. Norberg's empirical results are single values, which were likely either average numbers or estimates based on the testing conducted. The simulation scenario uses the parameters of the natural samara originally studied by Norberg, so $s(t) = 0$ for this verification. Since a moving mass has never been evaluated on a biomimetic single-winged vehicle, the time-varying portion of this model remains theoretical. Future work could involve designing a single moving mass controlled biomimetic vehicle for experimental study.

Figure 4-1 compares the four variables that have available data. Since Norberg did not explicitly have a coning angle rate calculation, the assumption is that the rate is negligibly small if the provided coning angle is in a steady state descent.

Generally, the outputs from the model presented in this paper complement the reduced order model as well as the empirical data. A small deviation in the coning angle exists between what was generated by the simulation and what was observed by Norberg. Seeing that the McConnell and Das reduced order model achieved the expected coning angle, the error is likely inherent to the extended model presented in this report. The cause of this deviation is suspected to be linked to the difference in how the moments of inertia are calculated. The McConnell and Das model uses a tuning parameter to numerically account for the nonuniform mass distribution of the samara, which appears to perform well. While the more detailed rigid body calculation of the moments of inertia are needed in the presented model to account for the moving mass, the use of the flat plate and thin rod may be too coarse.

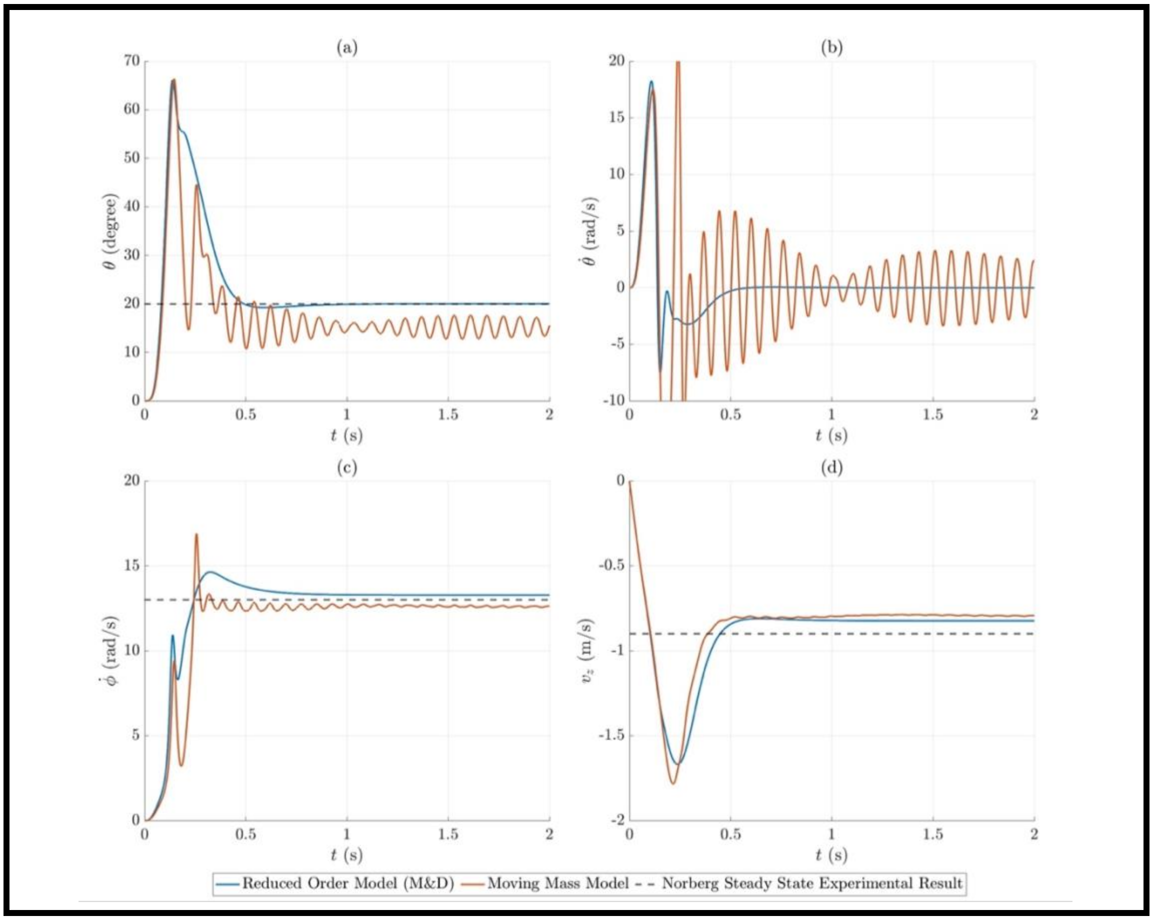

Figure 4-1. Model comparison with reduced order model [1] [2] [3] *and Norberg experimental results* [36]*: (a) coning angle over time; (b) coning angle rate of change over time; (c) rate of revolution over time; (d) vertical velocity over time.*

The other notable difference between the models is the sinusoidal perturbations that are present in the moving mass model. Because the moving mass model removed the pure vertical descent constraint, adding lateral motion, it makes sense that there will be some periodic variation in the variables. This will be discussed further in the next session; however, it is noteworthy that empirical results from various studies of samara and similar biomimetic vehicles revealed similar sinusoidal temporal perturbations in similar variables to what are being reviewed in Figure 4-1 [30] [63] [85]. The numerical study in [53] specifically looks at the temporal behavior of the coning angle in steady state descent, which shows agreement with the peak-to-peak amplitude of the perturbations being roughly 4 degrees.

4.2. Dynamics of the Baseline Model

Before evaluating the full time-varying model, the baseline case used in the model verification is examined closer. The simulation for this case was run for 60 seconds in duration to better understand the longer-term behavior of the model.

Figure 4-2 depicts the trajectory of the baseline case, of which a couple notable characteristics are revealed. First, there exists a macroscopic tornado-like precession cycle that appears to converge over time. This behavior is consistent with what has been observed in past studies. Norberg was one of the first researchers to document this behavior, calling it 'side-slip', which was observed to cause the samara to shift in the opposite direction of the samara's rotation [36]. This behavior was further characterized as a slow-moving large helix trajectory, but some samaras were observed to be more prone to this behavior than other, despite visually identical appearance [86]. Most recently, [40] studied this behavior relating it to a precession cycle and identified morphology, mass asymmetry, and wing thickness as key drivers in this behavior.

In terms of the other notable characteristic, small ripples in the trajectory are evident. This behavior is likely associated with the model's choice of fixed body origin, which serves as the position tracker of the samara. As discussed in Chapter 3, the fixed body origin was placed on the center of mass of the modeled seed portion of the samara to account for time-varying mass distribution changes. Because there is a displacement between the seed center of mass and the overall samara center of mass (which serves as the axis of rotation), this small ripple is reasonable behavior.

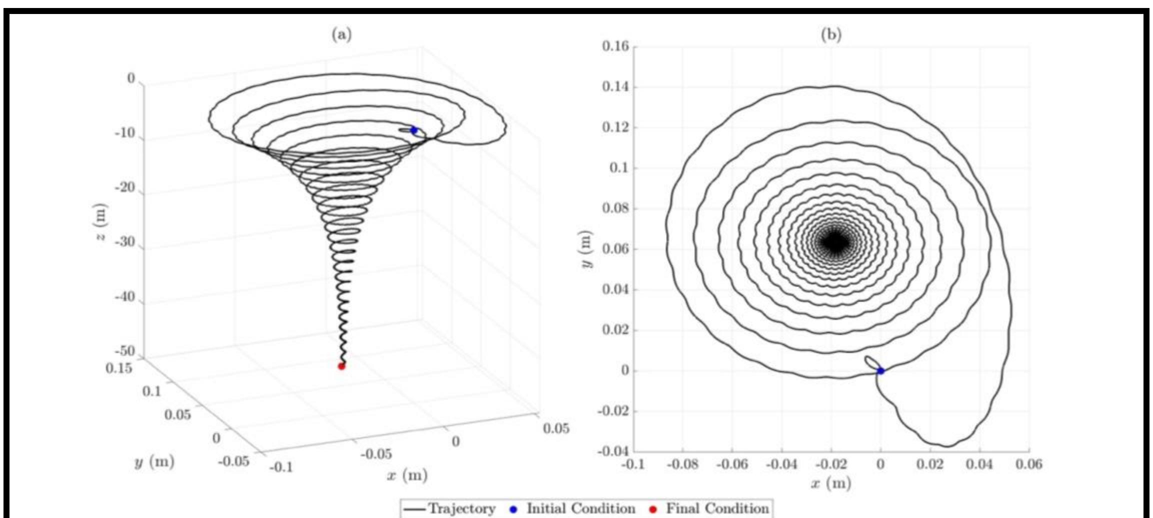

Figure 4-2. Baseline case trajectory: (a) 3-dimensional view; (b) overhead view of lateral displacement.

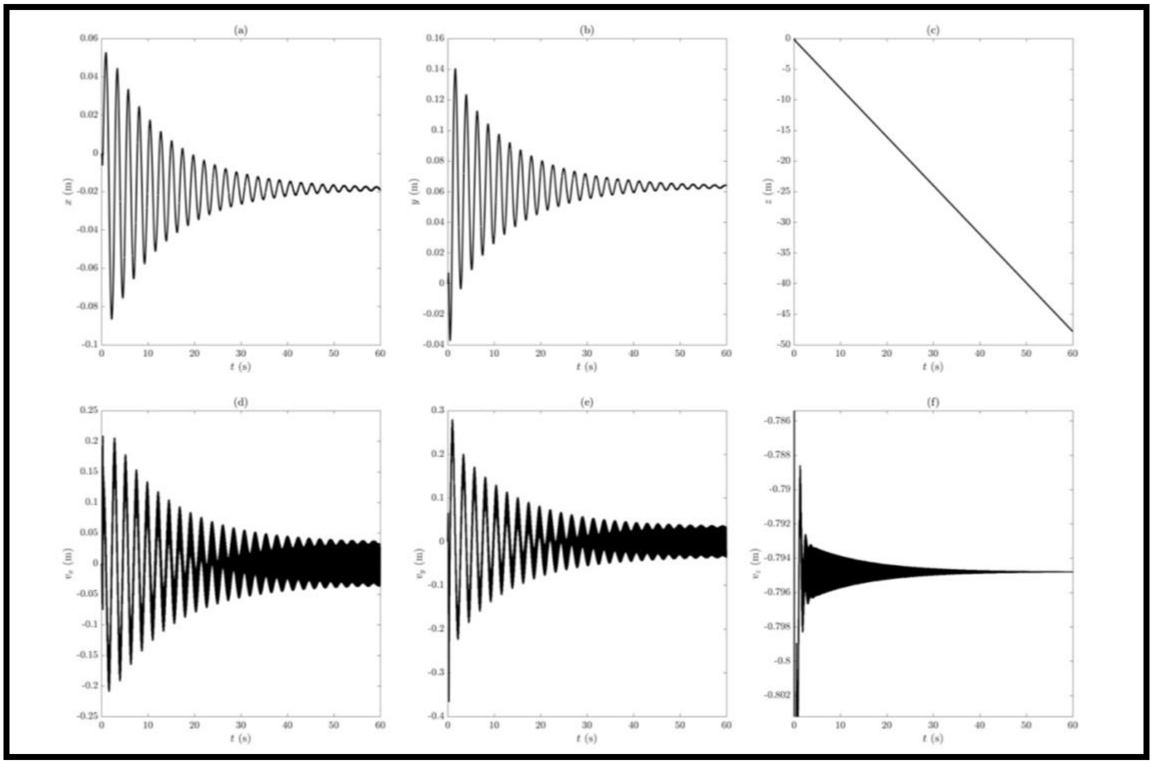

Figure 4-3. Baseline case inertial kinematics over time: (a) x position; (b) y position; (c) z position; (d) x velocity component; (e) y velocity component; (f) z velocity component.

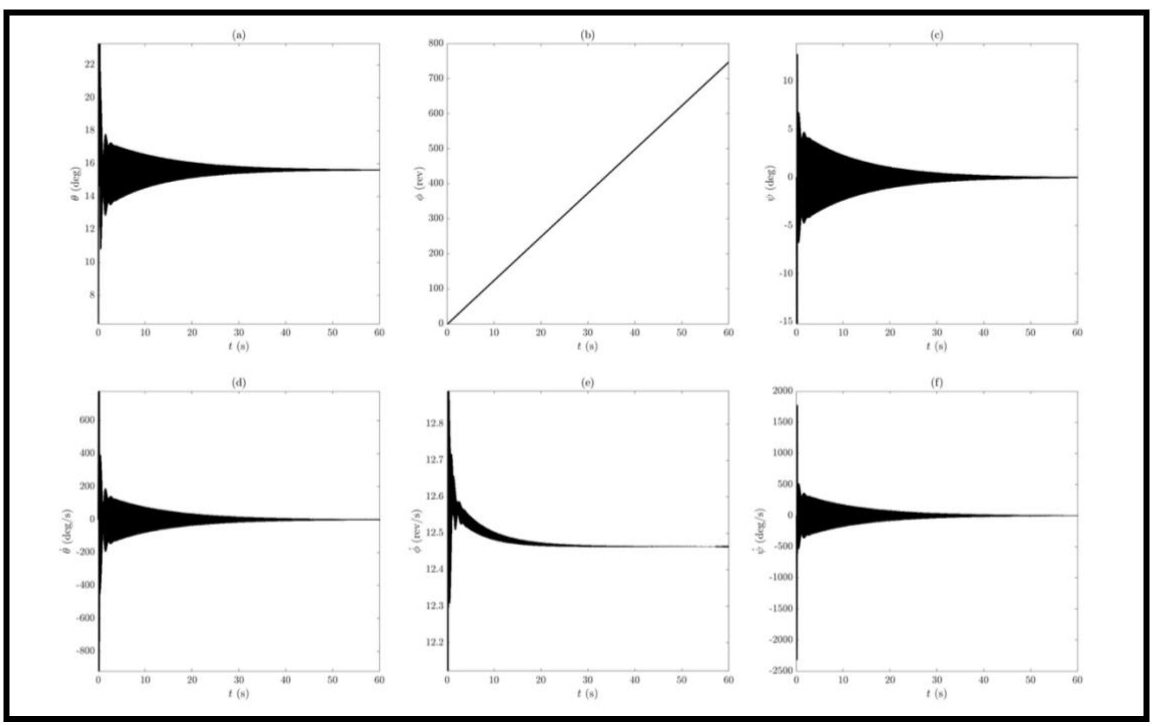

Figure 4-4. Baseline case rotational kinematics over time: (a) coning angle; (b) autorotational revolutions; (c) roll angle; (d) coning angle rate; (e) rotation frequency; (f) roll rate.

Figure 4-2 and Figure 4-3 depict the inertial and rotational kinematics, respectively, over the duration of the simulation. As an expected observation based on the tornado-like precession behavior, the sinusoidal behavior asymptotically stabilizes.

4.2.1. Precession Cycle Analysis

Diving a little deeper into the precession cycle behavior, Figure 4-5 depicts temporal analysis of the baseline case precession cycle. Figure 4-5(a) shows that the rate of completing a precession cycle is remarkably constant. The two drivers for the rate of precession cycle completion are the trajectory speed and the distance covered in each precession cycle. Figure 4-5(b) shows the trajectory speed is relatively constant but does gradually decrease over the first 20 seconds before stabilizing at approximately 0.8 m/s. Figure 4-5(c) agrees with the other two plots, showing that the distance between precession cycles is greatest in the first few cycles when the trajectory speed has the greatest amount of change, and as the distance between precession cycles approach zero, the trajectory speed stabilizes to a constant value.

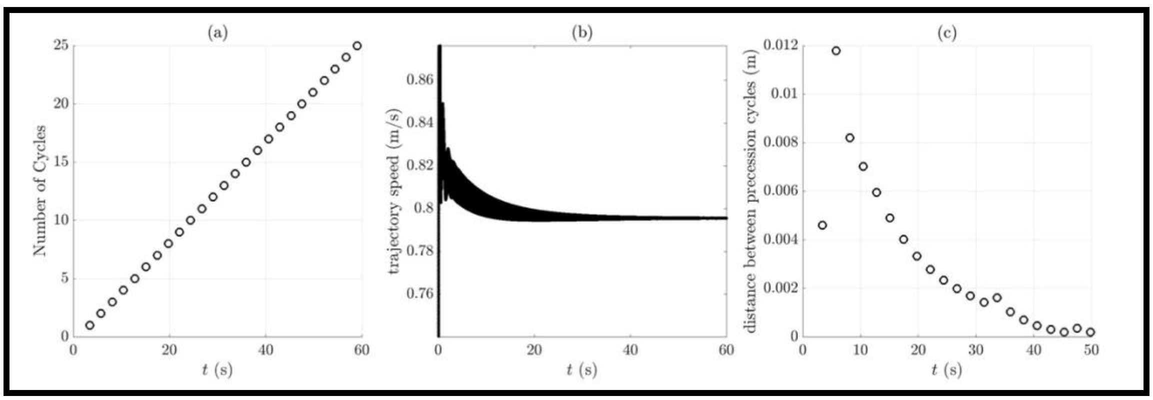

Figure 4-5. Temporal analysis of baseline case precession cycle: (a) number of precession cycles over time; (b) trajectory speed over time; (c) distance between precession cycles over time.

4.2.2. Effect of Moving Mass Size on Baseline Model

As the last study of the baseline case before introducing time-varying functions, a sizing study of the moving mass is used to determine the impact of adding the moving mass to the design. For this study, and all subsequent studies presented in this report, the simulation time is abbreviated to 20 seconds, which gives ample data to understand deviations in behavior. The default position of the moving mass is set to be at the center of the seed center of mass ($s(t) = 0$). Over the course of this study, the ratio of the total mass between the seed and the moving mass is varied while maintaining a constant m_w. Table 4-3 summarizes the ratio between the multiple mass points over the various runs. These same ratios are used for the similar mass studies performed on the time-varying case studies.

Table 4-3. Variation of mass parameters by simulation run.

Run Number	m_m	m_s	m_w
1	$0.8m$	$0.05m$	$0.15m$
2	$0.7m$	$0.15m$	$0.15m$
3	$0.6m$	$0.25m$	$0.15m$
4	$0.5m$	$0.35m$	$0.15m$
5	$0.4m$	$0.45m$	$0.15m$
6	$0.3m$	$0.55m$	$0.15m$
7	$0.2m$	$0.65m$	$0.15m$
8	$0.1m$	$0.75m$	$0.15m$

Figure 4-6 depicts the resulting trajectories from this study. While the model generally behaves the same regardless of the ratio of mass between the seed and the moving mass, there appears to be an interesting phasing of position that subtly grows with time. The source of this change is likely linked to the moments of inertia. The seed is modeled as thin rod with constant density. As the seed's mass is reduced and transferred to a moving mass, which is modeled as a point mass, the density of the seed geometric area is no longer constant since the location of the moving mass will be denser than any other part of the modeled seed and the overall center of mass of the samara is minorly shifted toward the seed center of mass. This effect is the inverse of what was studied in [40]; as the moving mass increases in size, the precession cycle reduces in radius, which creates a phasing of the trajectory. Figure 4-7 and Figure 4-8 depict the inertial and rotational kinematics, respectively, which more clearly shows the phasing of the variables with respect to the different runs.

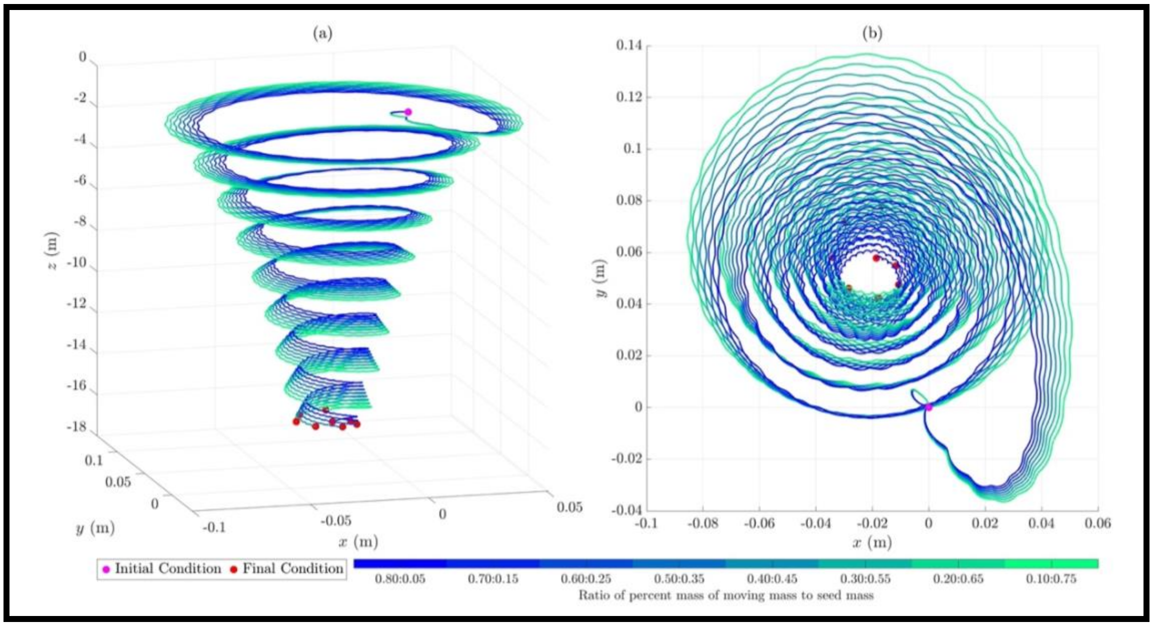

Figure 4-6. Baseline case trajectory with varying of size of moving mass: (a) 3-dimensional view; (b) overhead view of lateral displacement.

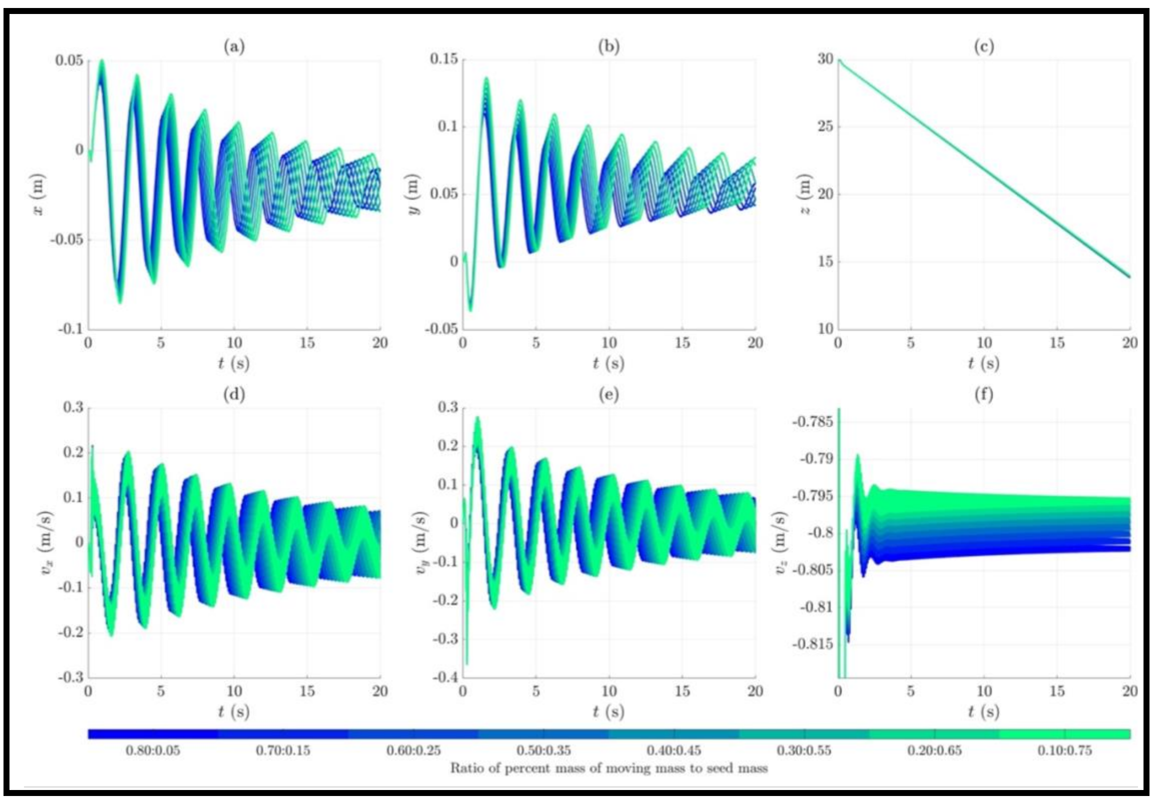

Figure 4-7. Baseline case inertial kinematics over time with varying of size of moving mass: (a) x position; (b) y position; (c) z position; (d) x velocity component; (e) y velocity component; (f) z velocity component.

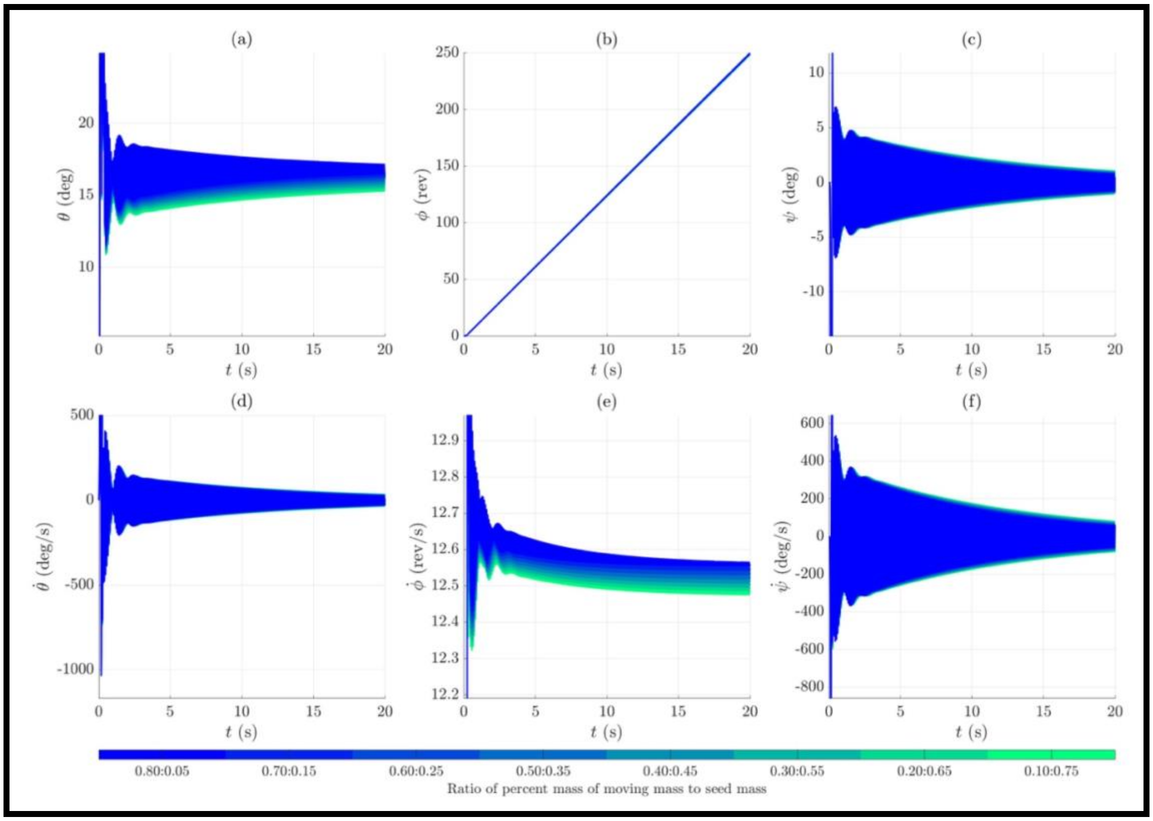

Figure 4-8. Baseline case rotational kinematics over time with varying of size of moving mass: (a) coning angle; (b) autorotational revolutions; (c) roll angle; (d) coning angle rate; (e) rotation frequency; (f) roll rate.

4.3. Evaluating Time-Varying Function

This section introduces four different case studies, each with a different time-varying function associated with the moving mass. Figure 4-9 provides the graphical depiction of the modulated position of the moving mass with respect to time. While only 12 seconds are shown in the plots, 20 seconds of simulation data was collected for each case study, which was an ample duration to assess the impact of the time-varying functions. The different case studies will be discussed in greater detail in subsequent sections.

One of the primary goals of the case studies is to provide a proof of concept that a moving mass could be used to control the lateral displacement of a samara-inspired vehicle. For the evaluation of the time-varying function, three different assessments are performed for each case study. First, a moving mass sizing assessment is performed to see what impact modulating different sized moving masses have on the model dynamics. As part of this study, one of the runs are selected based on which laterally displaces the vehicle the best. The associated mass distribution ratio is used for the subsequent two assessments, which focus on the impact of varying the trigger time of the $s(t)$ function by the period of the autorotation cycle (T_{ϕ}) and by the period of the precession cycle (T_P).

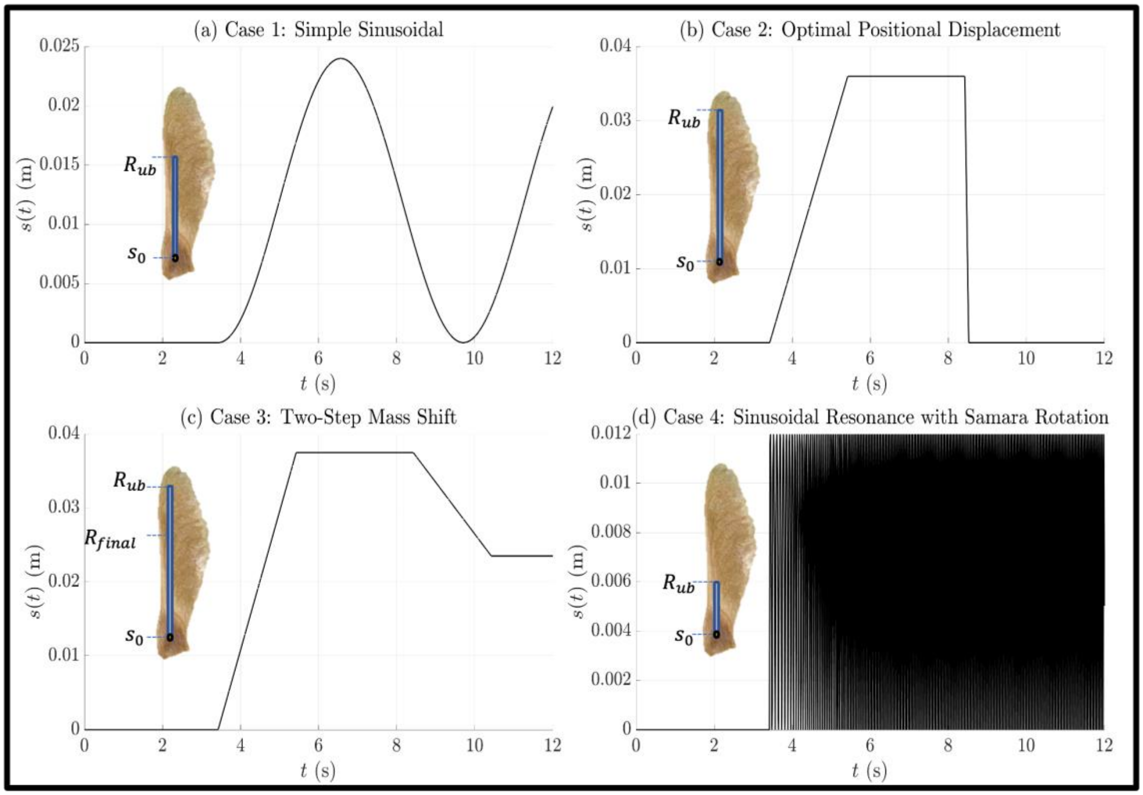

Figure 4-9. Functions used to modulate the moving mass along rail: (a) Cases 1; Simple Sinusoidal; (b) Case 2: Optimal Positional Displacement; (c) Two-Step Mass Shift; (d) Sinusoidal Resonance with Samara Rotation.

4.3.1. Case 1: Simple Sinusoidal

Case 1 can be described as a low frequency sinusoidal function, where the moving mass is slowly modulated between the lower and upper bound of the linear rail. The goal of this case study is to evaluate the impact of a simple oscillation of the moving mass on the dynamics of the model. As can be observed from Figure 4-9(a), once the function is triggered, one cycle takes approximately 6 seconds to complete. Equation (4-1) provides the mathematical expression for the function.

$$s(t) = \begin{cases} 0, & t < t_1 \\ -R_{ub}\sin(t - t_1 + \pi/2) + R_{ub}\,, & t \geq t_1 \end{cases} \tag{4-1}$$

where R_{ub} is the chosen amplitude of the sine function and t_1 is the activating trigger time for $s(t)$. Since R_{ub} is the amplitude of the sine function, $2R_{ub}$ is the upper bound of the moving mass rail. This value extends the moving mass significantly into the samara wing but not so far as to reach the tip of the samara wing. Table 4-4 defines the values of the parameters used in the time function for Case 1.

Table 4-4. Parameters used for the $s(t)$ time function for Case 1.

$s(t)$ **Parameters**	**Chosen Values for Case Study**
R_{ub}	$l = 0.012$ m

4.3.1.1. Case 1: Effect of Varying Size of Moving Mass

This section provides the results to the Case 1 moving mass sizing study, which uses the mass ratios defined in Table 4-3. The $s(t)$ function trigger time used was $t_1 = 3.4263$, which is roughly the time it takes for the base model to complete one precession cycle. Figure 4-10 depicts the resulting trajectories from this study, which all exhibited a periodic curlicue feature with the trajectories. The lighter moving masses do not seem to have enough mass to fully break away from the precession cycle and subsequently curl back into the initial precession cycle. The heaviest moving masses have no trouble breaking away, but the extra inertia associated with the heavier moving mass likely causes a slower turn with the curlicue feature, which cause them to effectively fold backwards toward the initial lateral position. Run 3 shows the optimal displacement of the samara from its initial position, where the curlicue launches the samara back in the same direction it was previously going. As such, $m_m = 0.6m$ and $m_s = 0.25m$ are used for the subsequent Case 1 assessments.

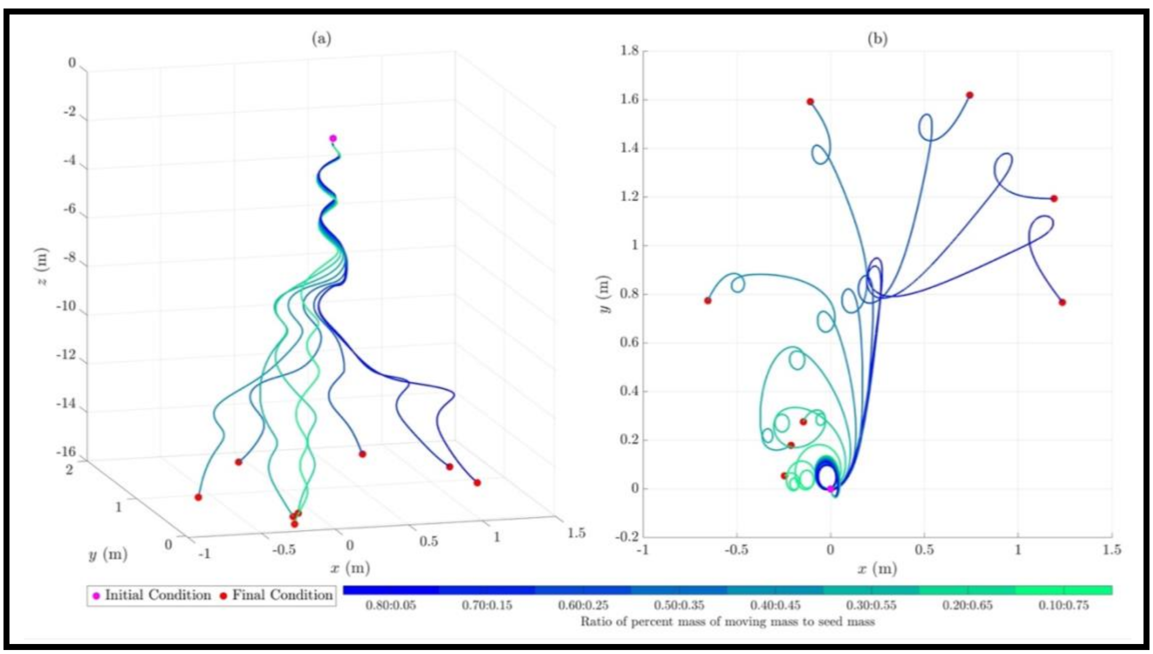

Figure 4-10. Case 1 trajectory with varying of size of moving mass: (a) 3-dimensional view; (b) overhead view of lateral displacement.

Figure 4-11 and Figure 4-12 depict the inertial and rotational kinematics, respectively. From the kinematics, it becomes apparent that the troughs in the sine function are associated with the curlicue feature. The telling variables are the peaks exhibited by the x and y position charts and the reduction in the vertical velocity v_z. Some of the rotational variables also surge at the sine troughs, reasonably due to the conservation of angular momentum.

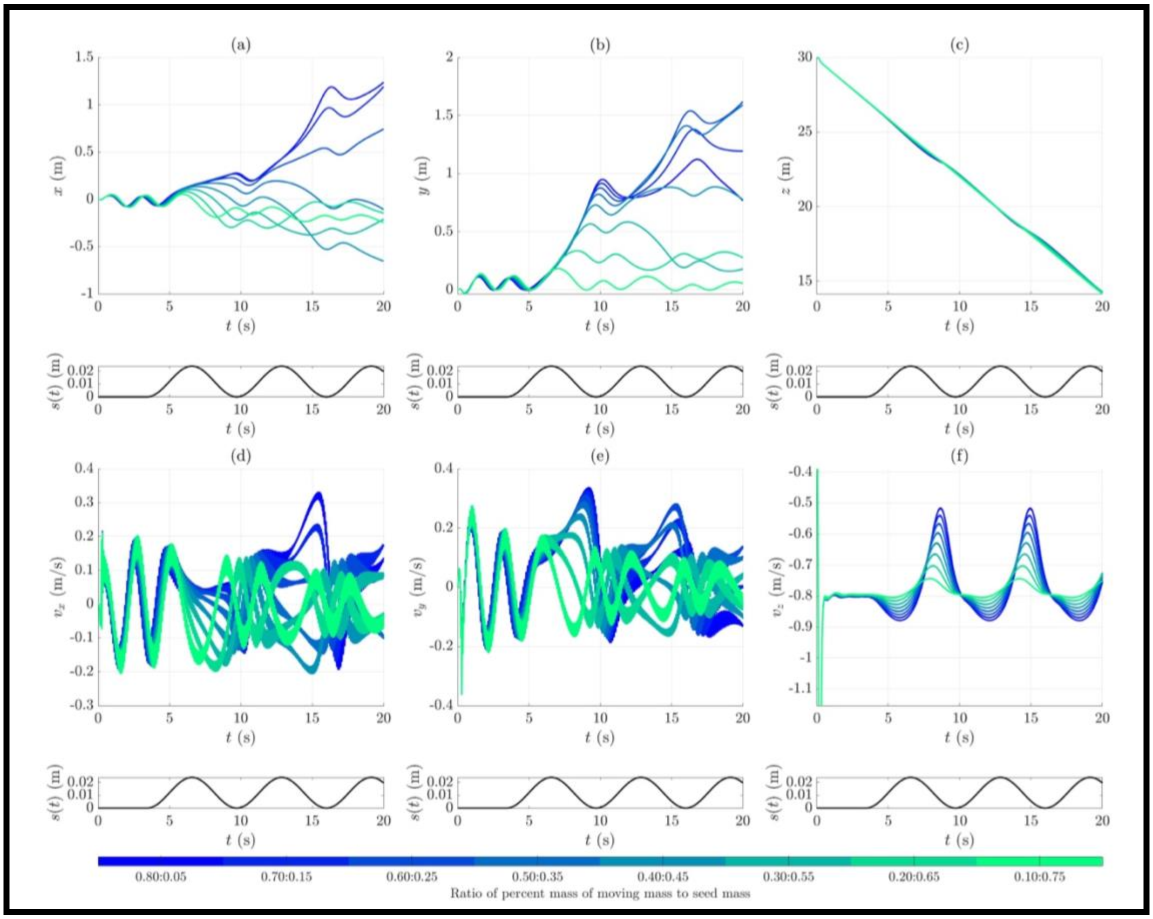

Figure 4-11. Case 1 inertial kinematics over time with varying of size of moving mass: (a) x position; (b) y position; (c) z position; (d) x velocity component; (e) y velocity component; (f) z velocity component.

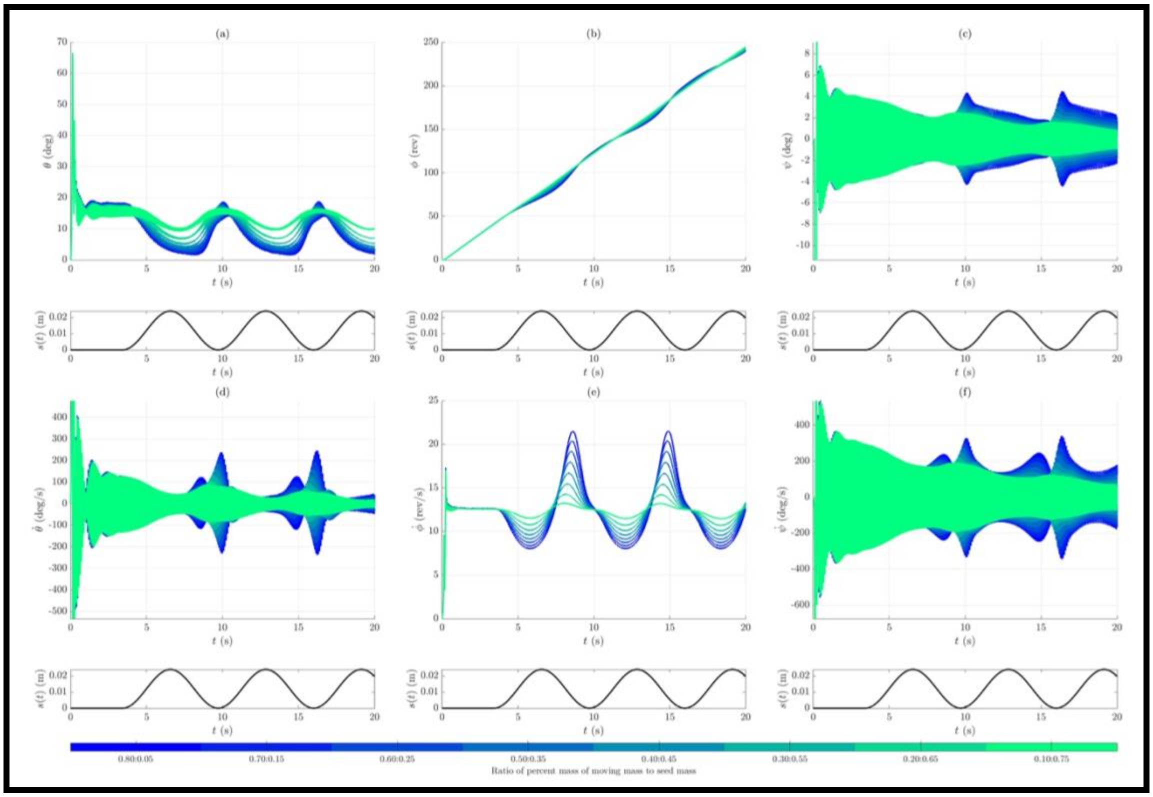

Figure 4-12. Case 1 rotational kinematics over time with varying of size of moving mass: (a) coning angle; (b) autorotational revolutions; (c) roll angle; (d) coning angle rate; (e) rotation frequency; (f) roll rate.

4.3.1.2. Case 1: Effect of Varying Trigger Time about the Samara Rotation

This section provides the results from the assessment of the effect of varying the trigger time t_1 based on varying points in the samara autorotational cycle period (T_ϕ). Table 4-5 shows the varying trigger times used for this assessment and the associated ϕ revolution. The t_1 times were selected for the runs such that each run was staggered by approximately a quarter revolution of the samara.

Table 4-5. Variation of moving mass trigger times by simulation run. Trigger times varied by roughly a quarter autorotation revolution per run.

Run Number	t_1 (s)	ϕ_1 (rev)
1	3.4263	40.99370227
2	3.4467	41.24974768
3	3.4667	41.50038538
4	3.4866	41.75011047
5	3.5065	41.99998412

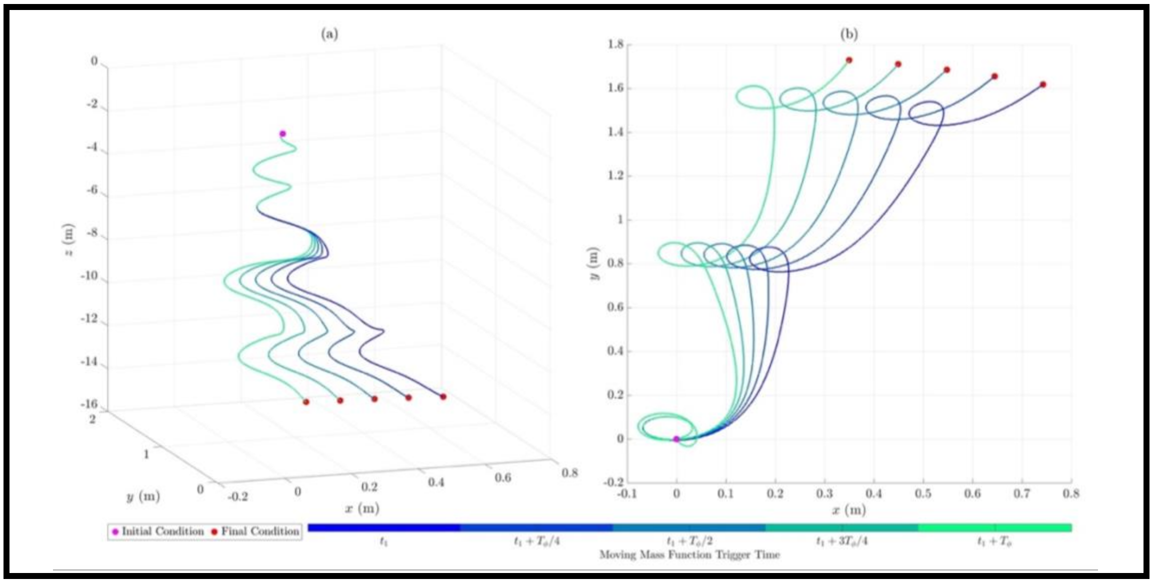

Figure 4-13. Case 1 trajectory with varying of moving mass trigger time about samara autorotation revolution: (a) 3-dimensional view; (b) overhead view of lateral displacement.

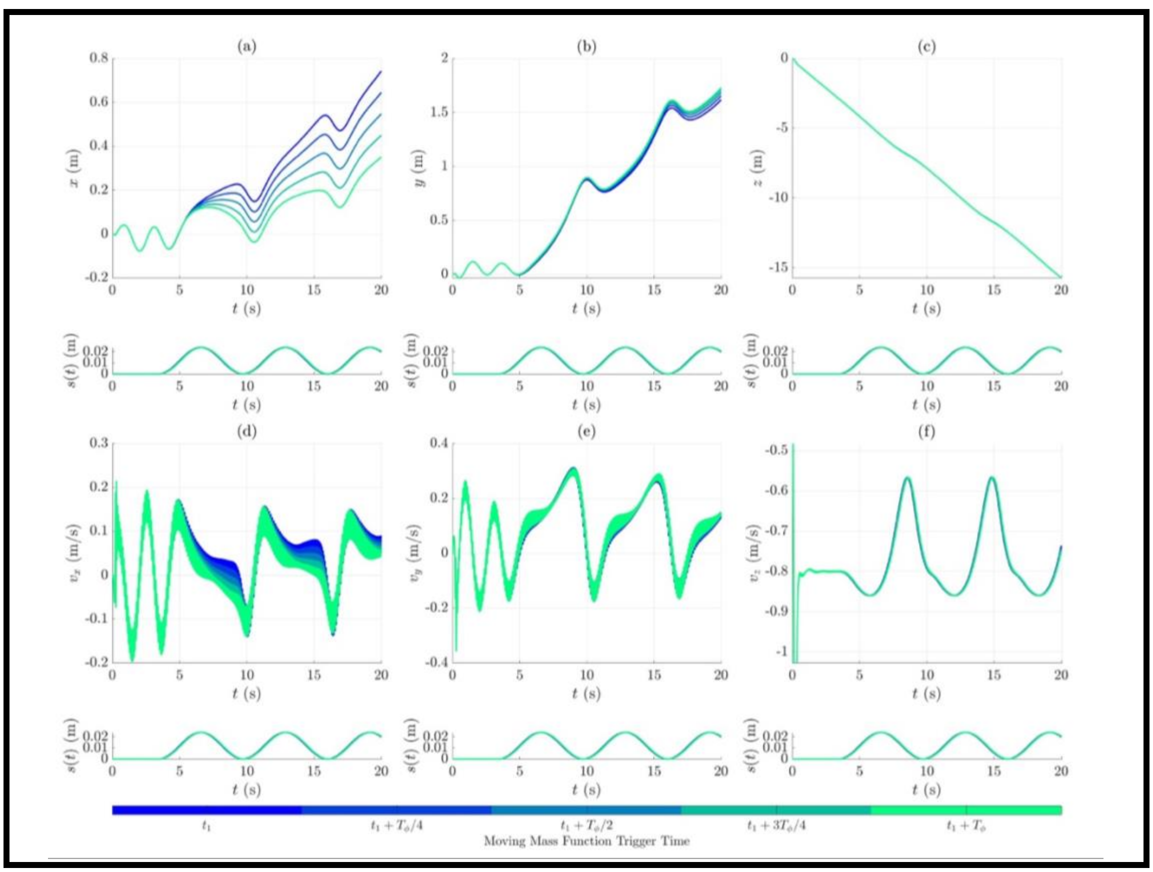

Figure 4-14. Case 1 inertial kinematics over time with varying of moving mass trigger time about samara autorotation revolution: (a) x position; (b) y position; (c) z position; (d) x velocity component; (e) y velocity component; (f) z velocity component.

Figure 4-13 depicts the resulting trajectories from the assessment. The only discernible difference between the trajectories is the slight variation in radial direction that the trajectories are traveling. Figure 4-14 and Figure 4-15 depict the inertial and rotational kinematics, respectively. From the kinematics, the phasing of the time trigger based T_ϕ has negligible influence on the model variables. The only kinematics that shows any significant difference are the x and y position and velocity; however, as will be discussed in section 4.3.1.3, this difference is likely due more to the change in precession cycle than the change orientation based on the autorotational revolution period.

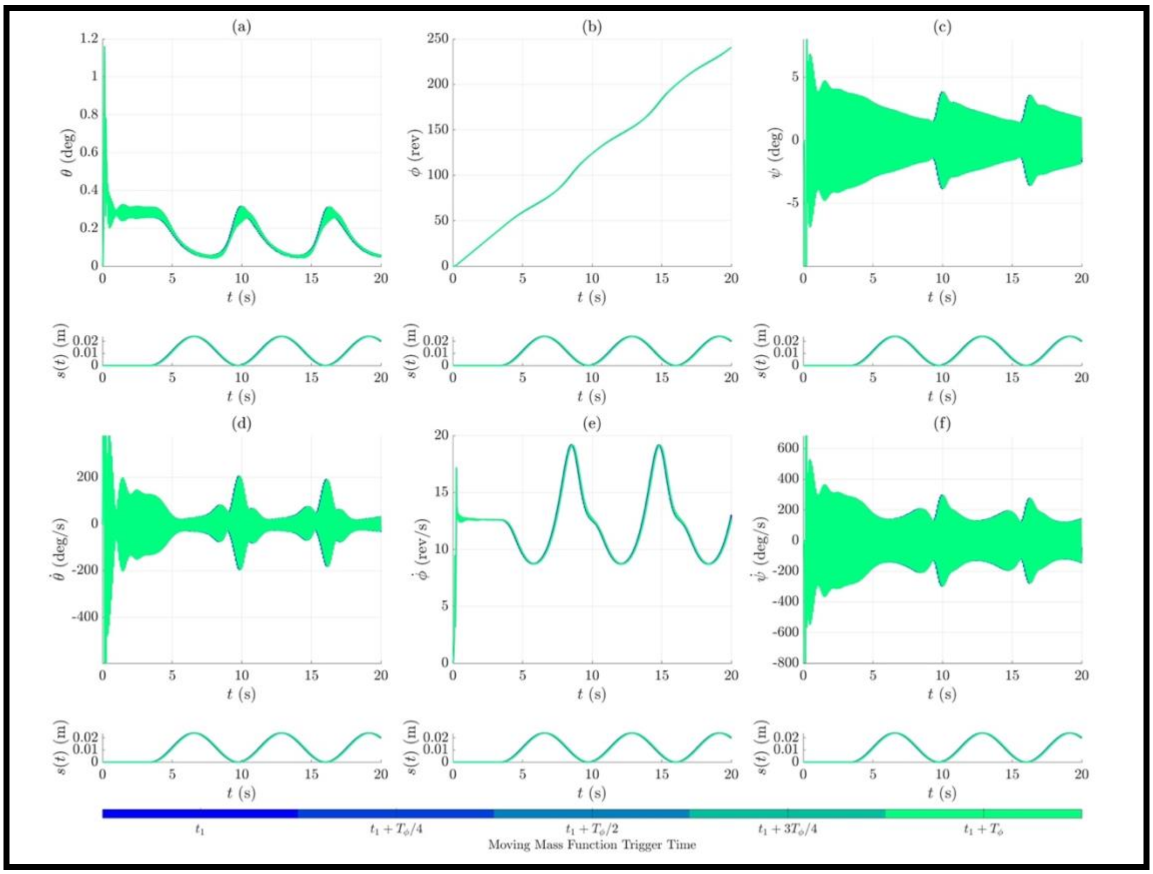

Figure 4-15. Case 1 rotational kinematics over time with varying of moving mass trigger time about samara autorotation revolution: (a) coning angle; (b) autorotational revolutions; (c) roll angle; (d) coning angle rate; (e) rotation frequency; (f) roll rate.

4.3.1.3. Case 1: Effect of Varying Trigger Time about the Precession Cycle

This section provides the results from the assessment of the effect of varying the trigger time t_1 based on varying points in the samara precession cycle period (T_P). Table 4-6 shows the varying trigger times used for this assessment and the associated ϕ revolution. It also gives an indication of the phasing of T_P. The t_1 times were selected for the runs such that each run was staggered by approximately a quarter precession cycle.

Table 4-6. Variation of moving mass trigger times by simulation run. Trigger times staggered by approximately a quarter of a precession cycle per run.

Run Number	t_1 (s)	ϕ_1 (rev)	T_P
1	3.4263	40.99370227	1
2	4.0153	48.38229935	1.25
3	4.6043	55.76623803	1.5
4	5.1933	63.14632271	1.75
5	5.7823	70.52303918	2

Figure 4-16 depicts the resulting trajectories from the assessment. The T_P phasing clearly has an impact to where the samara seed is displaced once the time function is activated. The only other notable feature is that the direction of the samara when released at $T_P = 1$ versus $T_P = 2$ is significantly different. This is likely due to the difference in size between the two cycles and can be explained by a similar phenomenon to the slingshot effect in orbital mechanics. Because the radius of the cycle at $T_P = 2$ is significantly smaller than that of $T_P = 1$, the samara will have less torque, which results in a slower release from the precession cycle once the time function is activated. Figure 4-17 and Figure 4-18 depict the inertial and rotational kinematics, respectively.

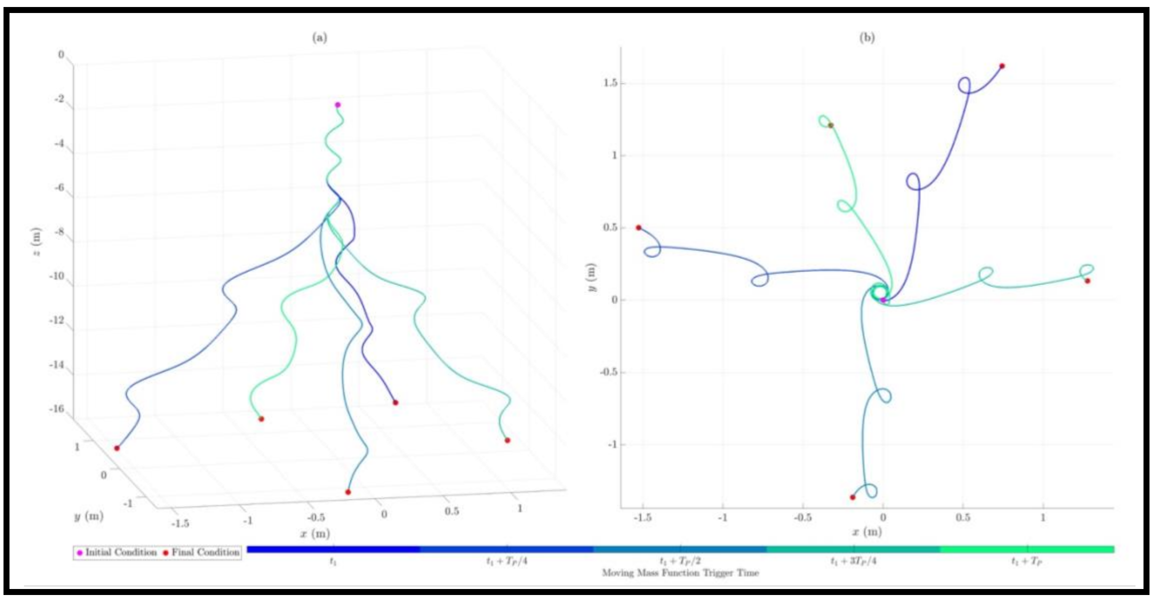

Figure 4-16. Case 1 trajectory with varying of moving mass trigger time about the precession cycle: (a) 3-dimensional view; (b) overhead view of lateral displacement.

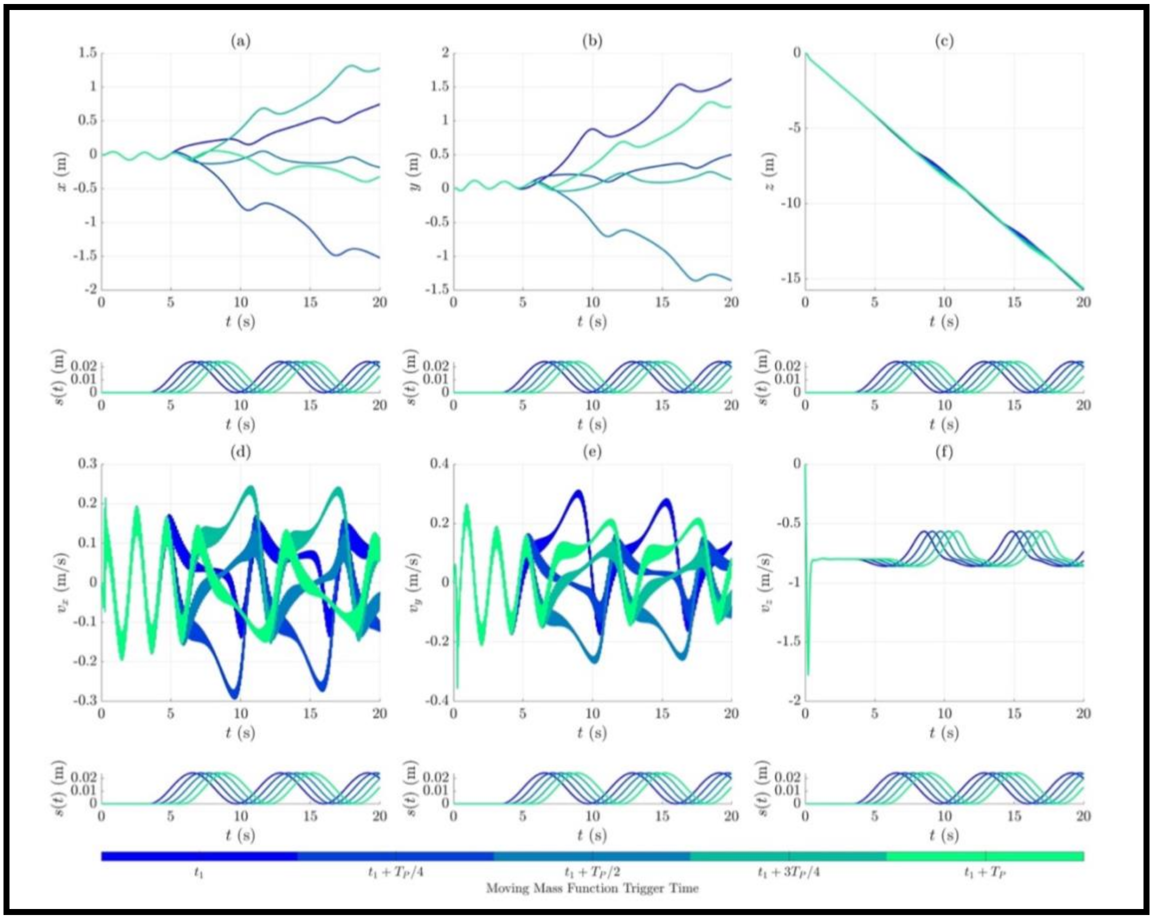

Figure 4-17. Case 1 inertial kinematics over time with varying of moving mass trigger time about the precession cycle: (a) x position; (b) y position; (c) z position; (d) x velocity component; (e) y velocity component; (f) z velocity component.

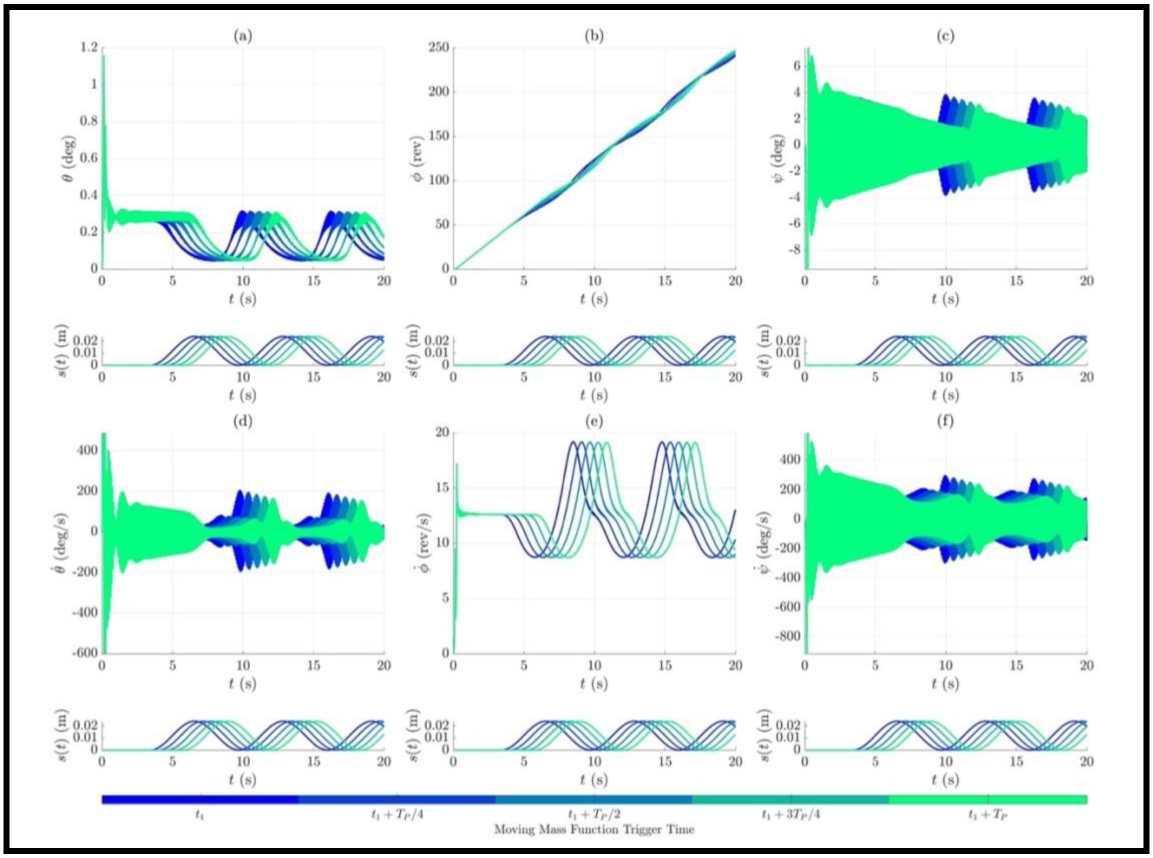

Figure 4-18. Case 1 rotational kinematics over time with varying of moving mass trigger time about the precession cycle: (a) coning angle; (b) autorotational revolutions; (c) roll angle; (d) coning angle rate; (e) rotation frequency; (f) roll rate.

4.3.2. Case 2: Optimal Positional Displacement

Case 2 can be described as a piecewise function that linearly ramps the moving mass to the upper bound of the rail, where it will stay for a designated period before quickly returning to the original position at the seed's center of mass. Case 1 revealed that the positional displacement occurs at the crest of the sinusoidal function. The goal of this case study is to evaluate whether the positional displacement can be more optimally executed by leaving the moving mass at the upper bound of the rail for a longer duration. Equation (4-2) provides the mathematical expression for the function.

$$s(t) = \begin{cases} 0, & t < t_1 \\ R_{ub}(t - t_1)/T_1, & t_1 \le t < t_1 + T_1 \\ R_{ub}, & t_1 + T_1 \le t < t_2 \\ R_{ub} - R_{ub}(t - t_2)/T_2, & t_2 \le t < t_2 + T_2 \\ 0, & t_2 + T_2 \le t \end{cases} \tag{4-2}$$

Table 4-7 defines the values of the parameters used in the time function for Case 2. Figure 4-9(b) gives the graphical depiction of the Case 2 function using these parameters.

Table 4-7. Parameters used for the $s(t)$ time function for Case 2.

$s(t)$ **Parameters**	**Chosen Values for Case Study**
R_{ub}	$3l = 0.036\ m$
T_1	2 s
T_2	0.1 s
t_2	$t_1 + 5\ s$

4.3.2.1. Case 2: Effect of Varying Size of Moving Mass

This section provides the results to the Case 2 moving mass sizing study, which uses the mass ratios defined in Table 4-3. The $s(t)$ function trigger time used was $t_1 = 3.4263$, which is roughly the time it takes for the base model to complete one precession cycle.

Figure 4-19 depicts the resulting trajectories from this study, which seem to show a more smoothed transition to a laterally displaced position. The lighter moving masses seem to have some trouble breaking the precession cycle, which is evident from the curling behavior back toward the initial precession cycle. Once the moving mass is at least 40% of the total mass of the samara, the samara appears to not have any issue breaking the precession cycle. Selecting the run that has the lightest moving mass that still achieves the optimal displacement objective, $m_m = 0.4m$ and $m_s = 0.45m$ are used for the subsequent Case 2 assessments.

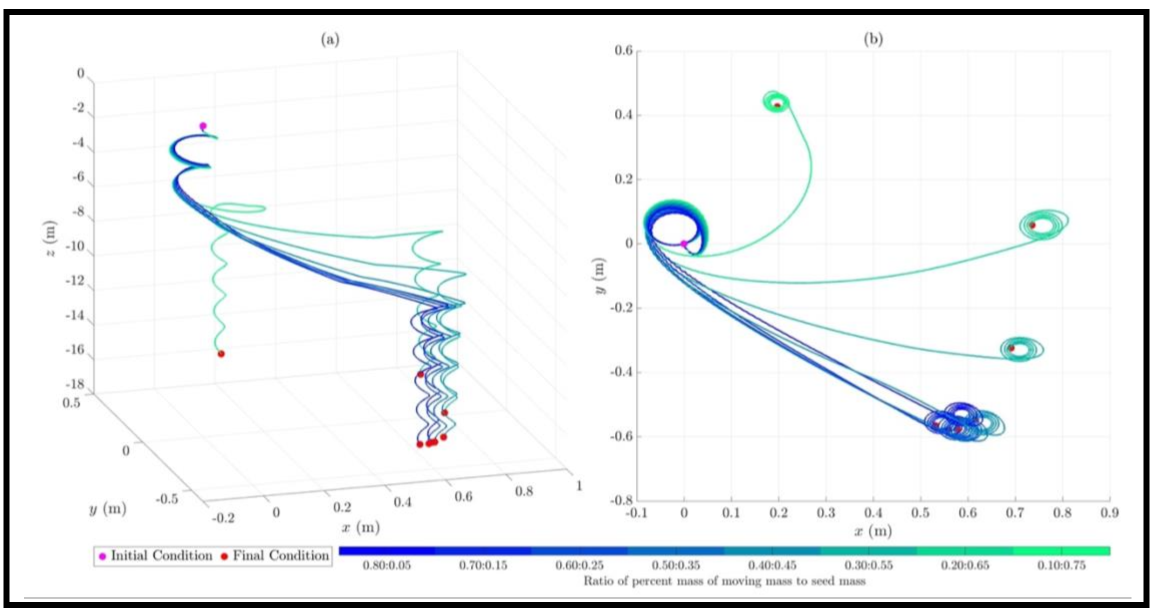

Figure 4-19. Case 2 trajectory with varying of size of moving mass: (a) 3-dimensional view; (b) overhead view of lateral displacement.

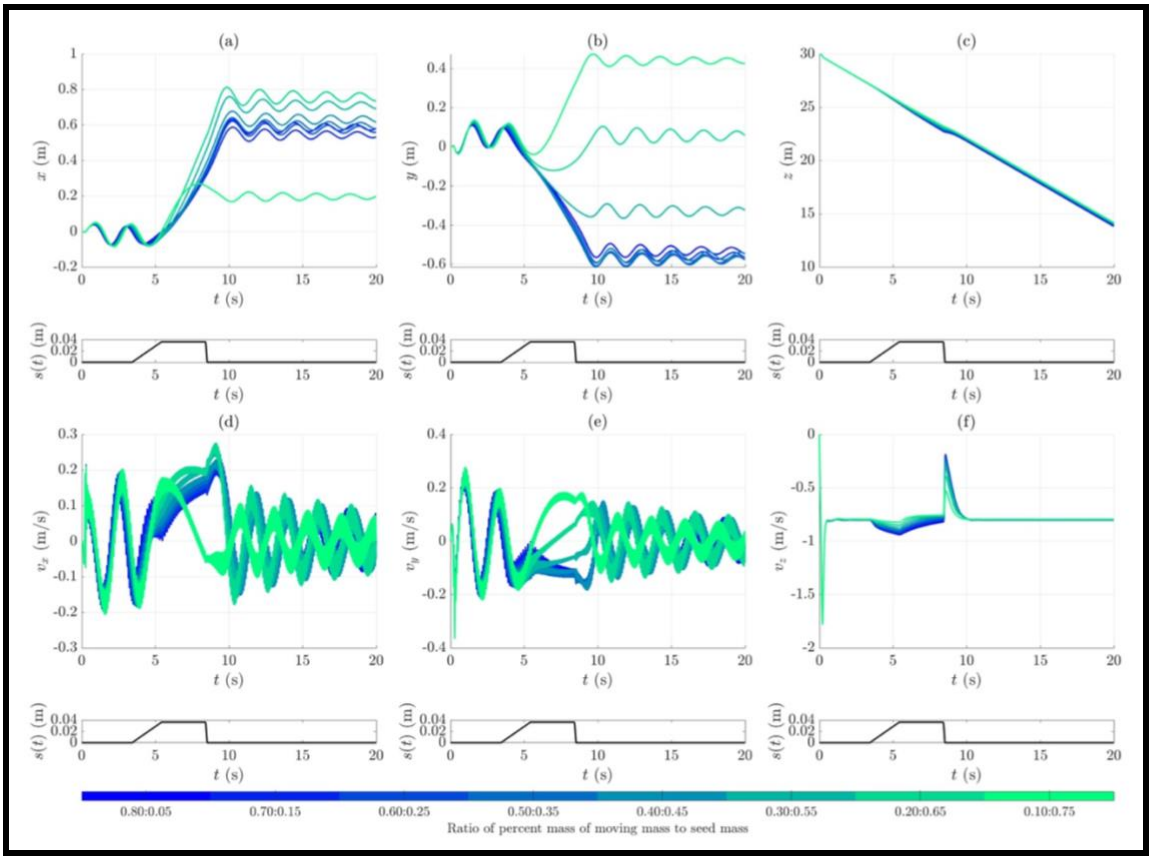

Figure 4-20. Case 2 inertial kinematics over time with varying of size of moving mass: (a) x position; (b) y position; (c) z position; (d) x velocity component; (e) y velocity component; (f) z velocity component.

Figure 4-20 and Figure 4-21 depict the inertial and rotational kinematics, respectively. From the kinematics, the displacement occurs while the moving mass is at the upper bound of the rail. As soon as the moving mass returns to its initial position in the seed, the seed begins a new precession cycle at the displaced location.

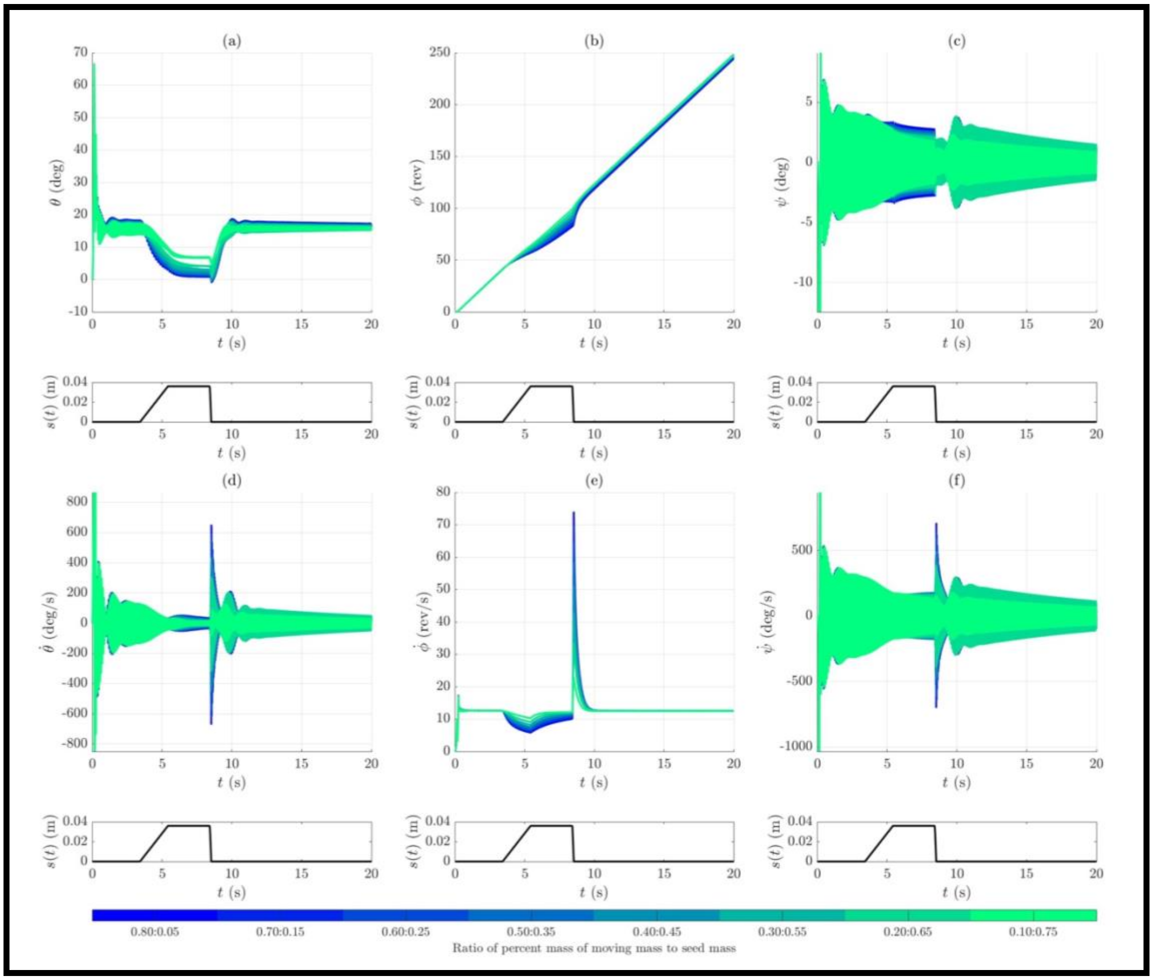

Figure 4-21. Case 2 rotational kinematics over time with varying of size of moving mass: (a) coning angle; (b) autorotational revolutions; (c) roll angle; (d) coning angle rate; (e) rotation frequency; (f) roll rate.

4.3.2.2. Case 2: Effect of Varying Trigger Time about the Samara Rotation

This section provides the results from the assessment of the effect of varying the trigger time t_1 based on varying points in the samara autorotational cycle period (T_ϕ). Table 4-5 in section 4.3.1.2 shows the varying trigger times used for this assessment and the associated ϕ revolution. The t_1 times were selected for the runs such that each run was staggered by approximately a quarter revolution of the samara.

Figure 4-22 depicts the resulting trajectories from the assessment. Like Case 1, the only discernible difference between the trajectories is the slight variation in radial direction that the trajectories are traveling. It is interesting that the last few runs are not evenly spaced, which would indicate that while most of the impact is likely due to the precession cycle, there may be some impact caused by T_ϕ.

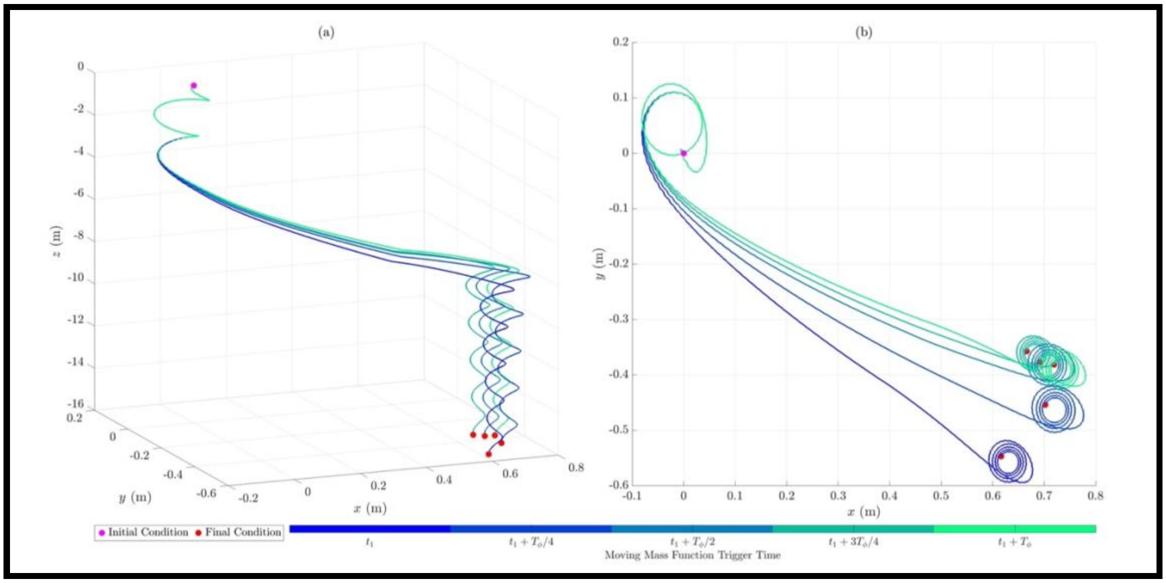

Figure 4-22. Case 2 trajectory with varying of moving mass trigger time about samara autorotation revolution: (a) 3-dimensional view; (b) overhead view of lateral displacement.

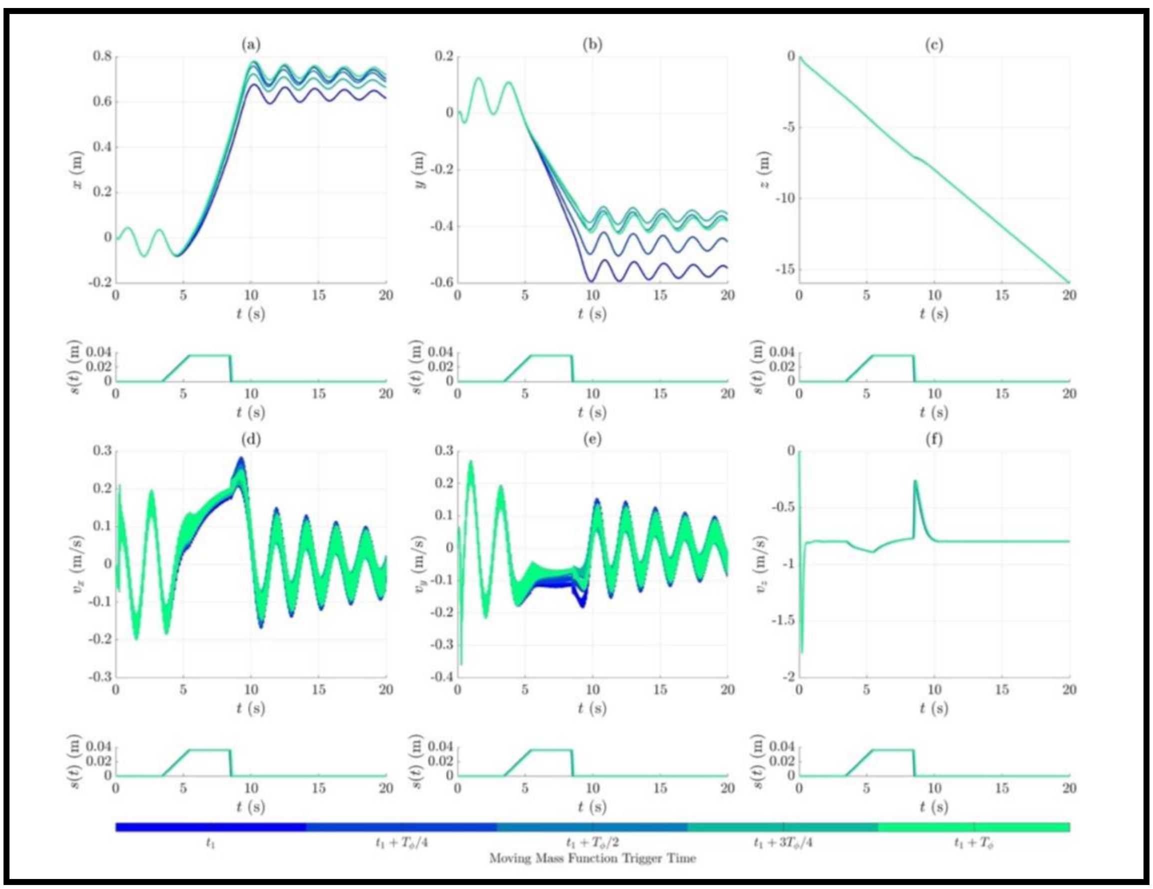

Figure 4-23. Case 2 inertial kinematics over time with varying of moving mass trigger time about samara autorotation revolution: (a) x position; (b) y position; (c) z position; (d) x velocity component; (e) y velocity component; (f) z velocity component.

Figure 4-23 and Figure 4-24 depict the inertial and rotational kinematics, respectively. From the kinematics, the phasing of the time trigger based T_ϕ has negligible influence on the model variables. The only variables that show any significant difference are the x and y position and velocity; however, as will be discussed in section 4.3.2.3, this difference is likely due more to the change in precession cycle than the change in orientation based on the autorotational revolution period.

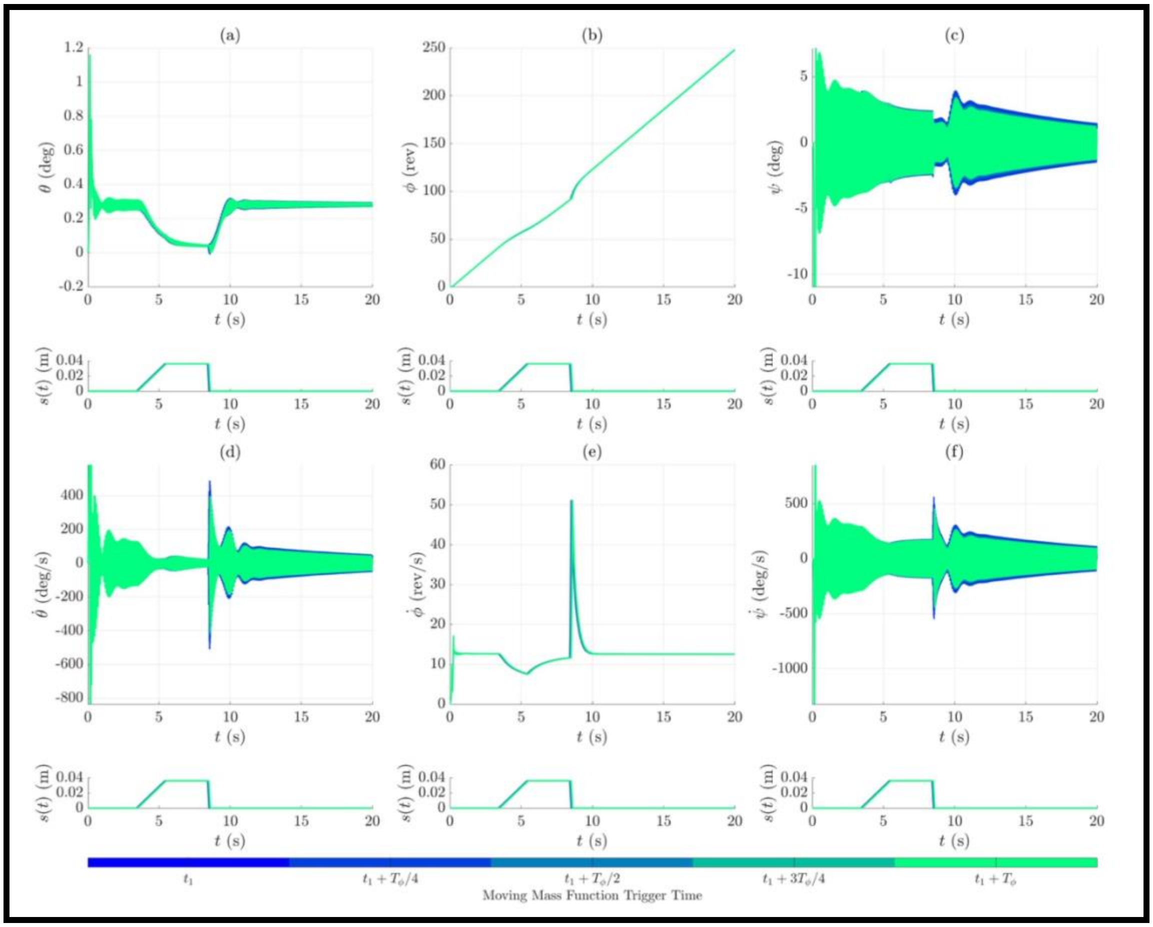

Figure 4-24. Case 2 rotational kinematics over time with varying of moving mass trigger time about samara autorotation revolution: (a) coning angle; (b) autorotational revolutions; (c) roll angle; (d) coning angle rate; (e) rotation frequency; (f) roll rate.

4.3.2.3. Case 2: Effect of Varying Trigger Time about the Precession Cycle

This section provides the results from the assessment of the effect of varying the trigger time t_1 based on varying points in the samara precession cycle period (T_P). Table 4-6 in section 4.3.1.3 shows the varying trigger times used for this assessment and the associated ϕ revolution. It also gives an indication of the phasing of T_P. The t_1 times were selected for the runs such that each run was staggered by approximately a quarter precession cycle.

Figure 4-25 depicts the resulting trajectories from the assessment. The T_P phasing clearly has an impact to where the samara seed is displaced once the $s(t)$ function is activated. The only other notable feature is that the direction of the samara when released at $T_P = 1$ versus $T_P = 2$ is significantly different. Like Case 1, this behavior is probably due to the size of the precession cycles being significantly different and can be explained by a similar phenomenon to the slingshot effect in orbital mechanics. Because the radius of the cycle at $T_P = 2$ is significantly smaller than that of $T_P = 1$, the samara will have less torque, which results in a slower release from the precession cycle once the time function is activated. Figure 4-26 and Figure 4-27 depict the inertial and rotational kinematics, respectively.

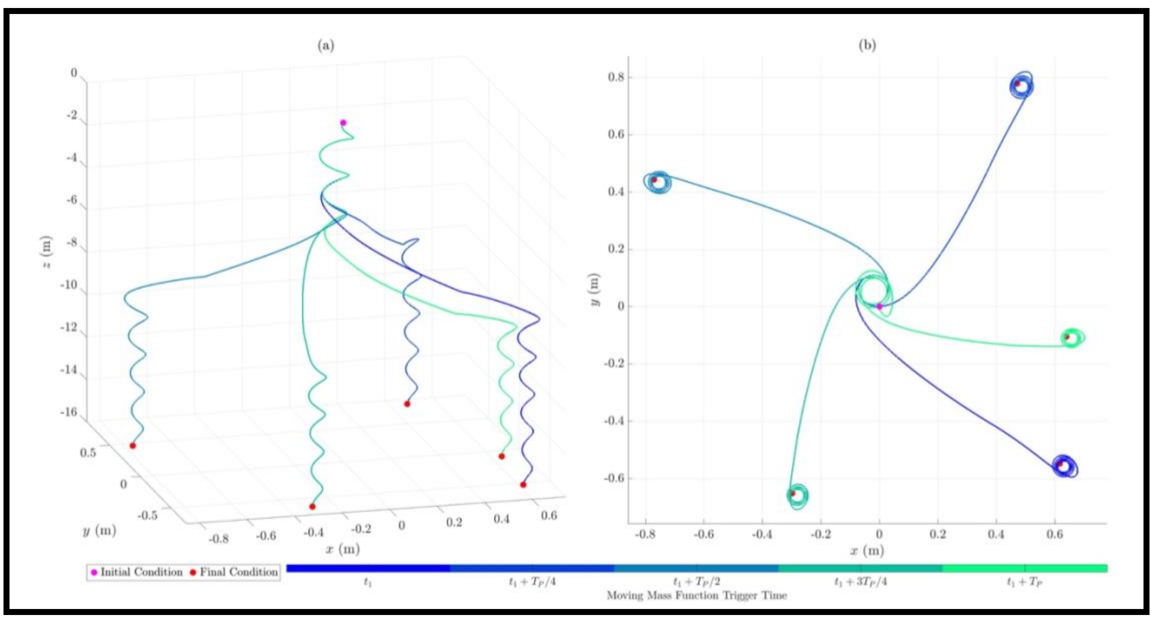

Figure 4-25. Case 2 trajectory with varying of moving mass trigger time about the precession cycle: (a) 3-dimensional view; (b) overhead view of lateral displacement.

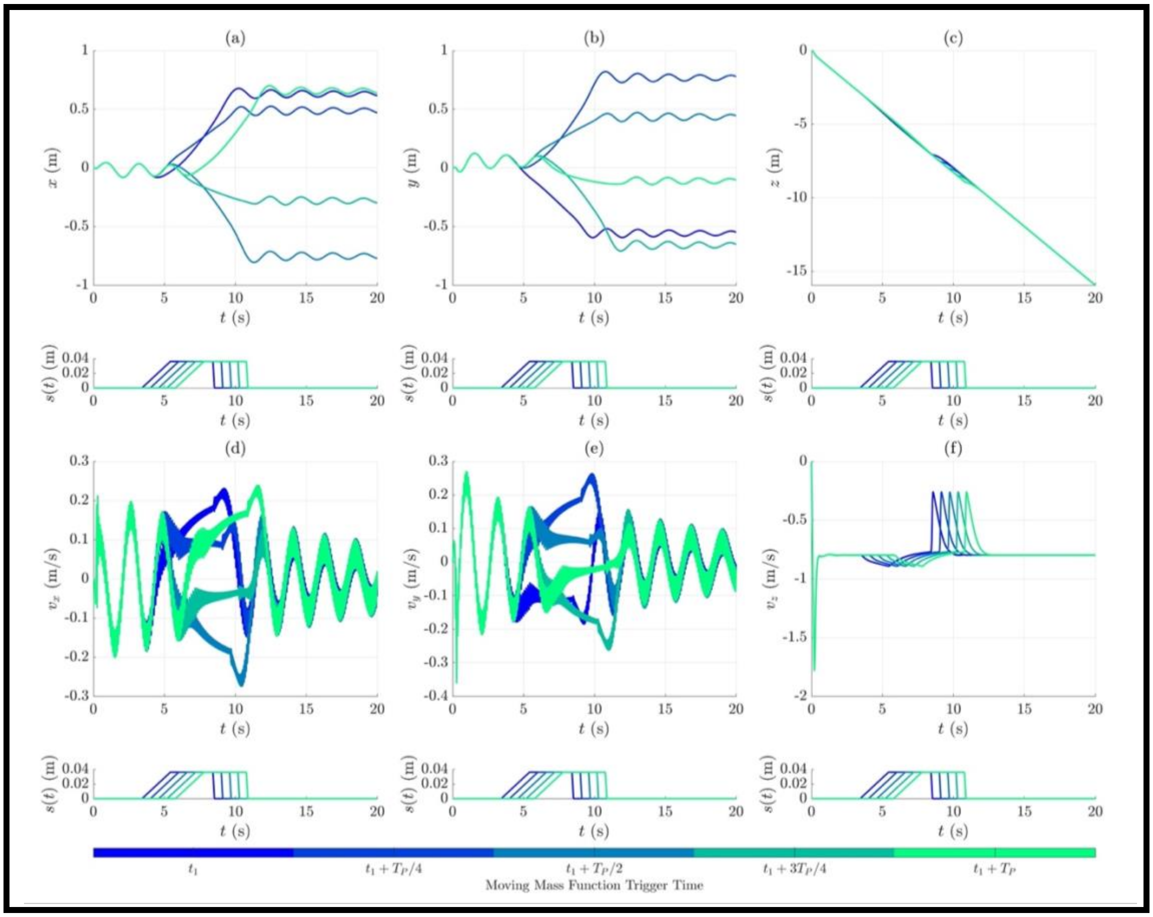

Figure 4-26. Case 2 inertial kinematics over time with varying of moving mass trigger time about the precession cycle: (a) x position; (b) y position; (c) z position; (d) x velocity component; (e) y velocity component; (f) z velocity component.

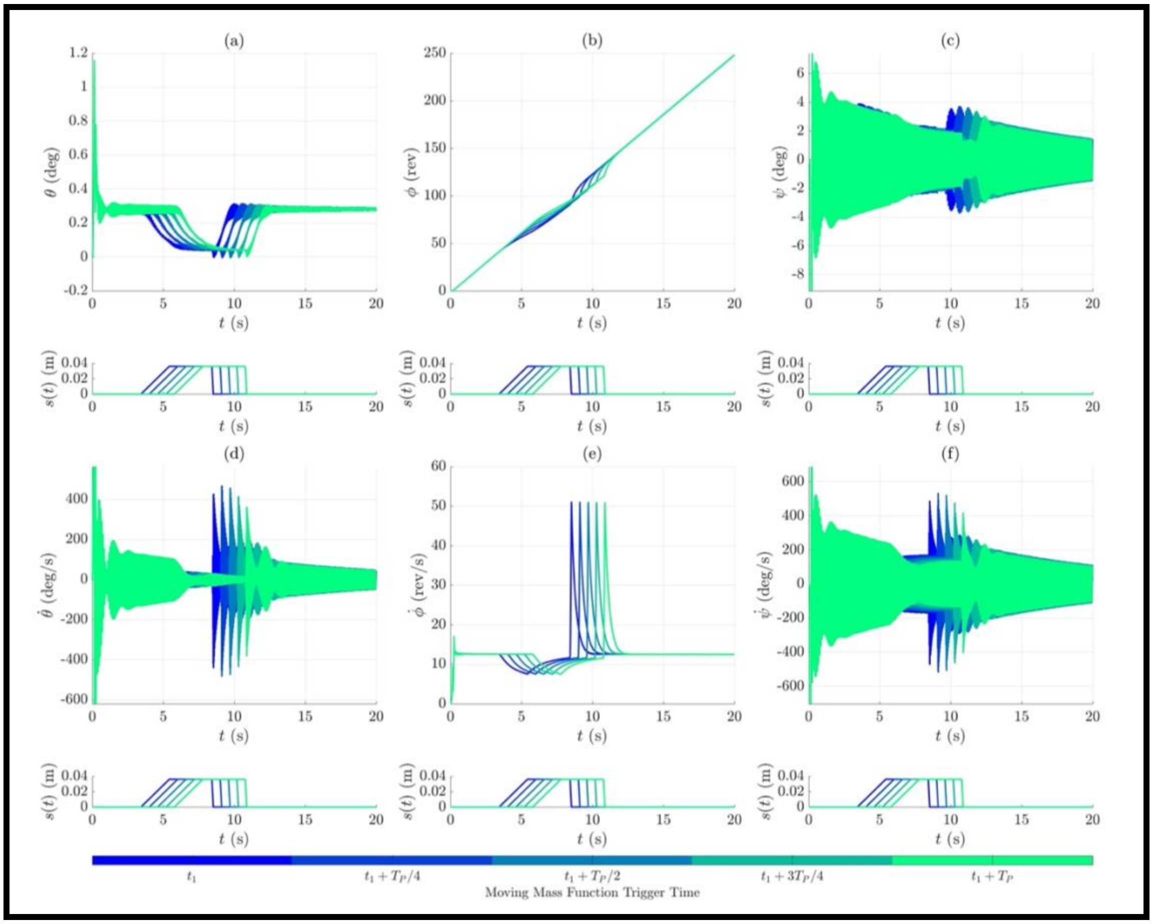

Figure 4-27. Case 2 rotational kinematics over time with varying of moving mass trigger time about the precession cycle: (a) coning angle; (b) autorotational revolutions; (c) roll angle; (d) coning angle rate; (e) rotation frequency; (f) roll rate.

4.3.3. Case 3: Two Step Mass Shift - Opposite End Followed by Center of Geometry

Case 3 can be described as a piecewise function that linearly ramps the moving mass to the upper bound of the rail, where it will stay for a designated period before ramping down to near the center of geometry. Prior work evaluated mass distribution on samara descent behavior and identified four different modes (autorotation, spiral/tumbling, chaotic, and falling) [33]. The goal of this case study was to attempt to trigger the falling mode after displacing the samara in order to create a flight termination function that could be used once the samara reached the intended coordinates. Equation (4-3) provides the mathematical expression for the function.

$$s(t) = \begin{cases} 0, & t < t_1 \\ R_{ub}(t - t_1)/T_1, & t_1 \le t < t_1 + T_1 \\ R_{ub}, & t_1 + T_1 \le t < t_2 \\ R_{ub} - \left(R_{final} - R_{ub}\right)(t - t_2)/T_2, & t_2 \le t < t_2 + T_2 \\ R_{final}, & t_2 + T_2 \le t \end{cases} \tag{4-3}$$

Table 4-8 defines the values of the parameters used in the $s(t)$ function for Case 3. Figure 4-9(c) gives the graphical depiction of the Case 3 function using these parameters.

Table 4-8. Parameters used for the $s(t)$ time function for Case 3.

$s(t)$ **Parameters**	**Chosen Values for Case Study**
R_{ub}	$l/2 + 0.9a = 0.0375\ m$
R_{final}	$l/2 + 0.5a = 0.0235\ m$
T_1	2 s
T_2	2 s
t_2	$t_1 + T_1 + 3\ s$

4.3.3.1. Case 3: Effect of Varying Size of Moving Mass

This section provides the results to the Case 3 moving mass sizing study, which uses the mass ratios defined in Table 4-3. The $s(t)$ function trigger time used was $t_1 = 3.4263$, which is roughly the time it takes for the base model to complete one precession cycle.

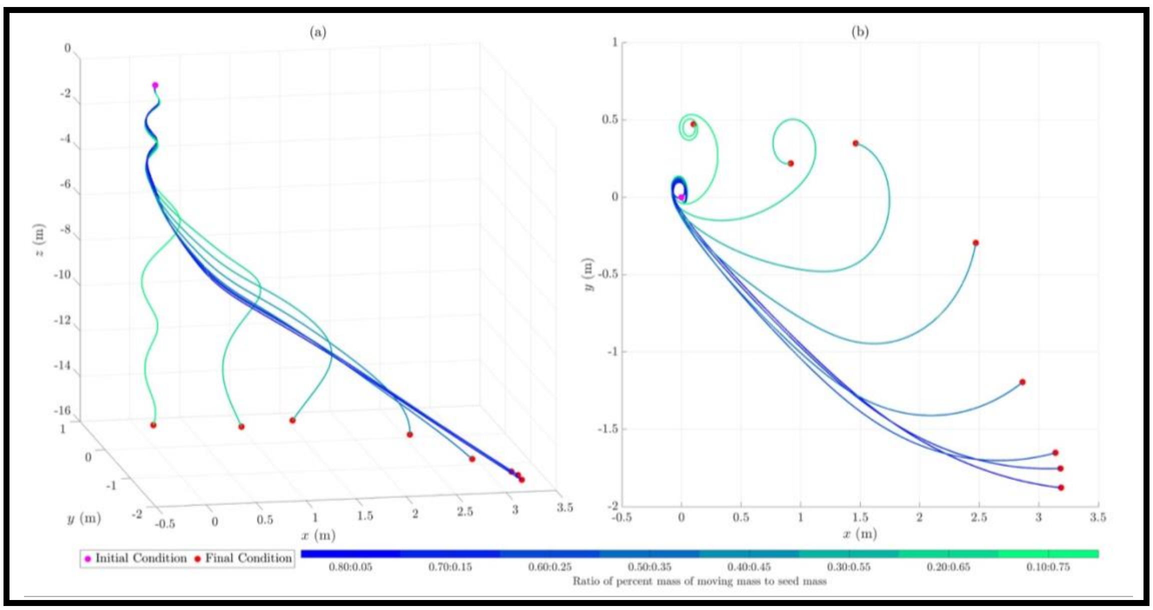

Figure 4-28. Case 3 trajectory with varying of size of moving mass: (a) 3-dimensional view; (b) overhead view of lateral displacement.

Figure 4-28 depicts the resulting trajectories from this study. None of the runs seem to terminate, since all scenarios end with the vertical displacement consistent with the previous two case studies (roughly 16m in the z direction). The lighter moving masses seem to have some trouble breaking the precession cycle, which is evident from the curling behavior back toward the initial precession cycle. The trajectory continues to straighten out with the heavier moving masses, where the straightest trajectory is with the heaviest moving mass (80% of the samara overall mass). Particularly for the heavier cases, the lateral velocity increases the most during the final partially extended position of the moving mass. Based on the chart provided in [33], it is possible that the final moving mass position picked was in line with the chaotic mode, which would explain why the heavier masses continued traveling in the same direction that it started. While this case is showing greater lateral displacement than the previous two cases, the chaotic mode of descent may make the time function difficult to use from controllability and repeatability perspectives. Since none of the runs meet the goal of terminating the flight, the run that optimizes displacement was used. Thus, $m_m = 0.8m$ and $m_s = 0.05m$ are used for the subsequent Case 3 assessments.

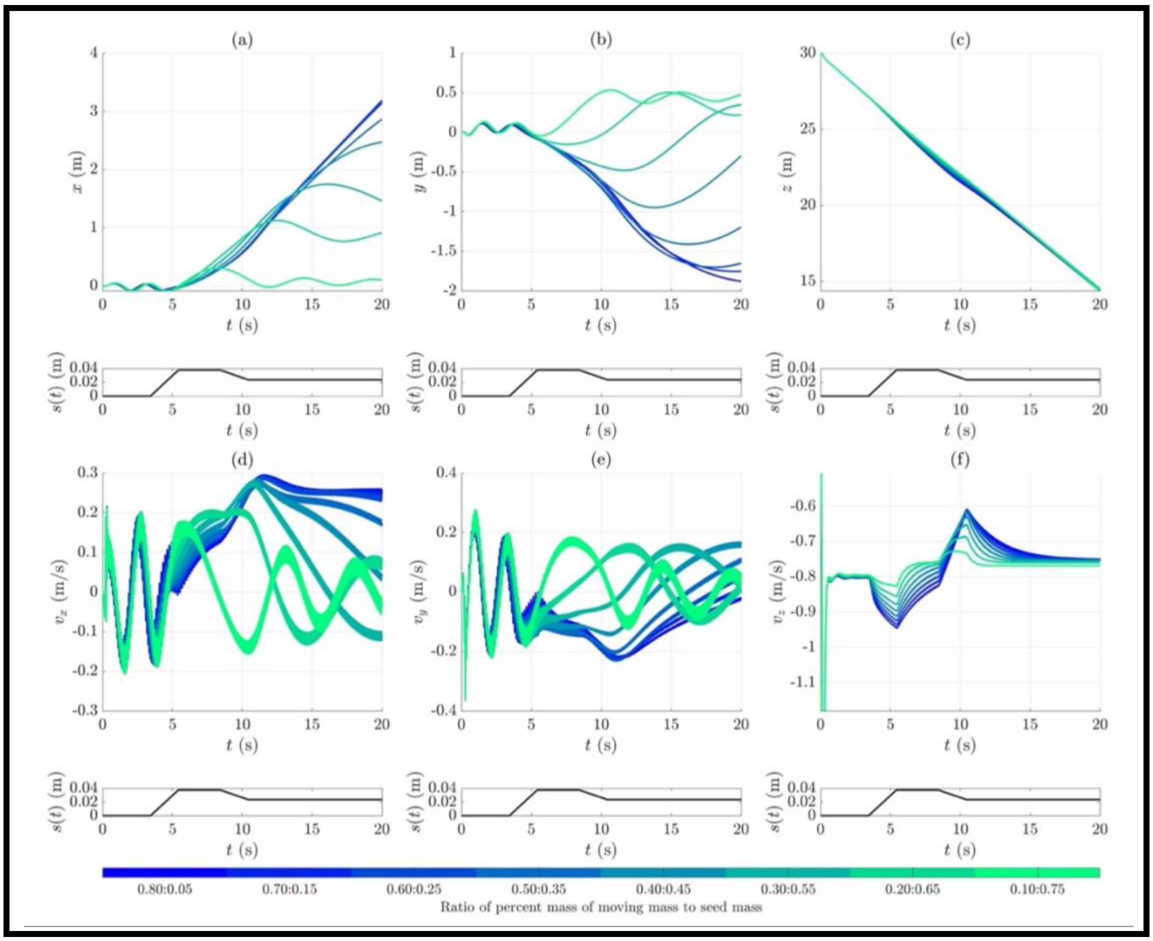

Figure 4-29. Case 3 inertial kinematics over time with varying of size of moving mass: (a) x position; (b) y position; (c) z position; (d) x velocity component; (e) y velocity component; (f) z velocity component.

Figure 4-29 and Figure 4-30 depict the inertial and rotational kinematics, respectively. From the kinematics, the size of the moving mass will drive the level of displacement with this time function. It is also interesting that the roll angle differential increases with the heavier moving masses during the phase of flight after the moving mass reaches its final position at the center of geometry.

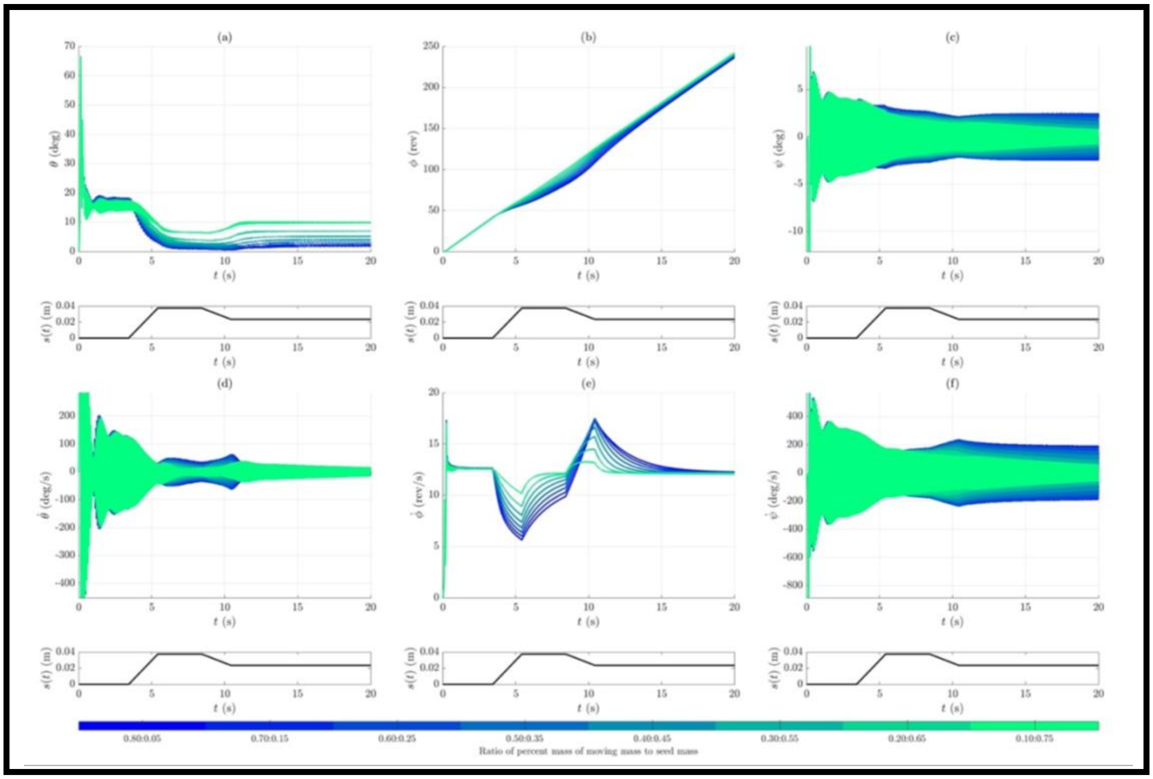

Figure 4-30. Case 3 rotational kinematics over time with varying of size of moving mass: (a) coning angle; (b) autorotational revolutions; (c) roll angle; (d) coning angle rate; (e) rotation frequency; (f) roll rate.

4.3.3.2. Case 3: Effect of Varying Trigger Time about the Samara Rotation

This section provides the results from the assessment of the effect of varying the trigger time t_1 based on varying points in the samara autorotational cycle period (T_ϕ). Table 4-5 in section 4.3.1.2 shows the varying trigger times used for this assessment and the associated ϕ revolution. The t_1 times were selected for the runs such that each run was staggered by approximately a quarter revolution of the samara.

Figure 4-31 depicts the resulting trajectories from the assessment. Like the previous cases, the only discernible difference between the trajectories is the slight variation in radial direction that the trajectories are traveling. Like Case 2 (but arguably more subtle), the trajectories from the runs are not evenly spaced, which would indicate that while most of the impact is likely due to the precession cycle, there may be some impact caused by T_ϕ.

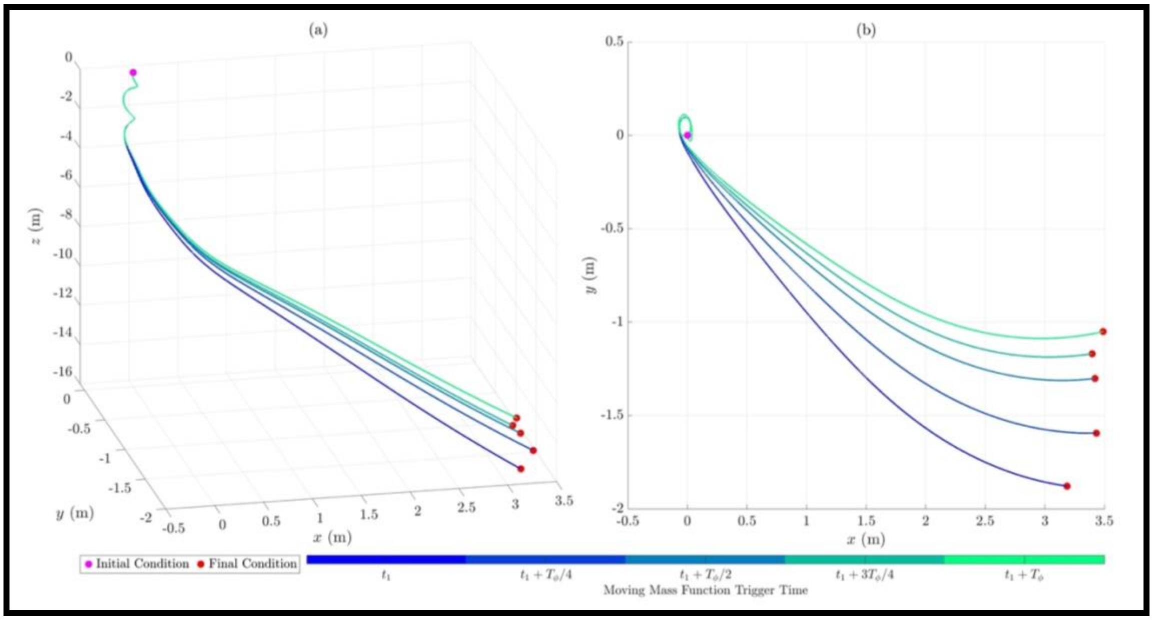

Figure 4-31. Case 3 trajectory with varying of moving mass trigger time about samara autorotation revolution: (a) 3-dimensional view; (b) overhead view of lateral displacement.

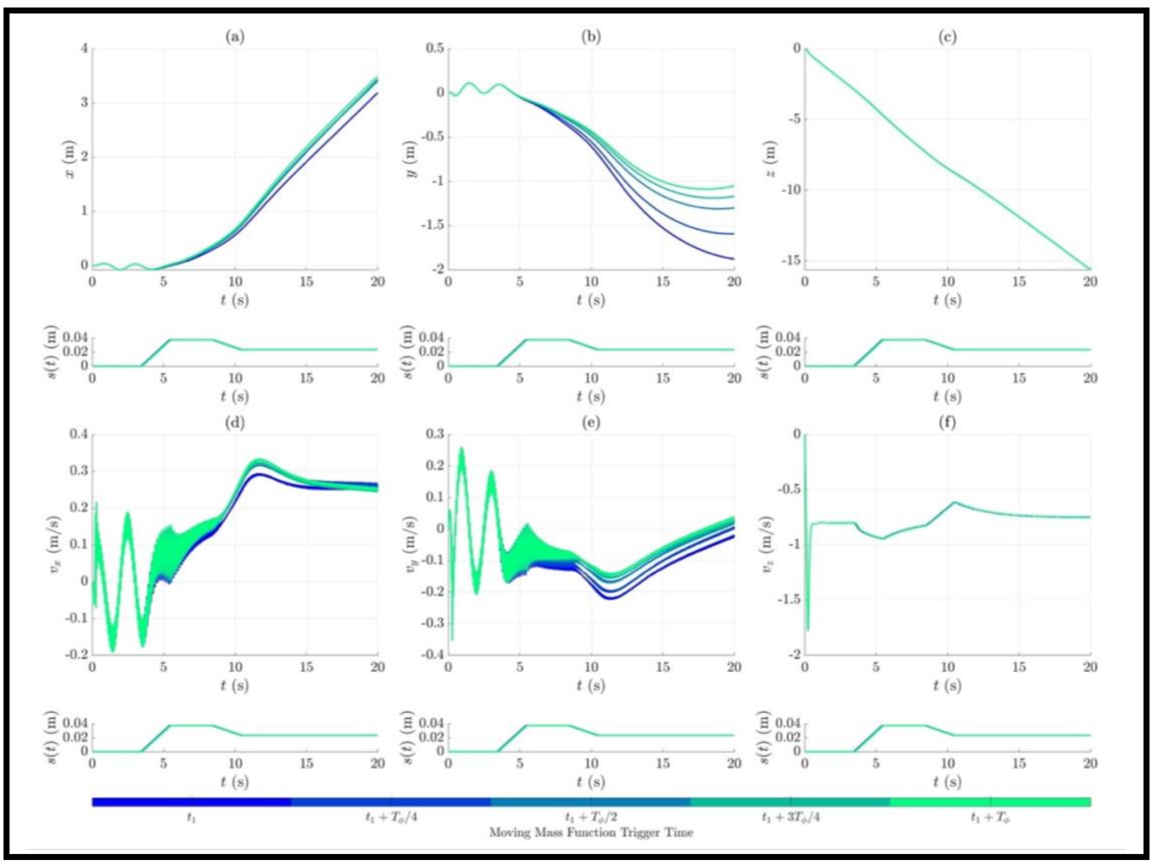

Figure 4-32. Case 3 inertial kinematics over time with varying of moving mass trigger time about samara autorotation revolution: (a) x position; (b) y position; (c) z position; (d) x velocity component; (e) y velocity component; (f) z velocity component.

Figure 4-32 and Figure 4-33 depict the inertial and rotational kinematics, respectively. From the kinematics, the phasing of the time trigger based T_ϕ has negligible influence on the model variables. The only kinematics that shows any appreciable difference are the x and y position and velocity; however, as will be discussed in section 4.3.3.3, this difference is likely due more to the change in precession cycle than the change in orientation based on the autorotational revolution period.

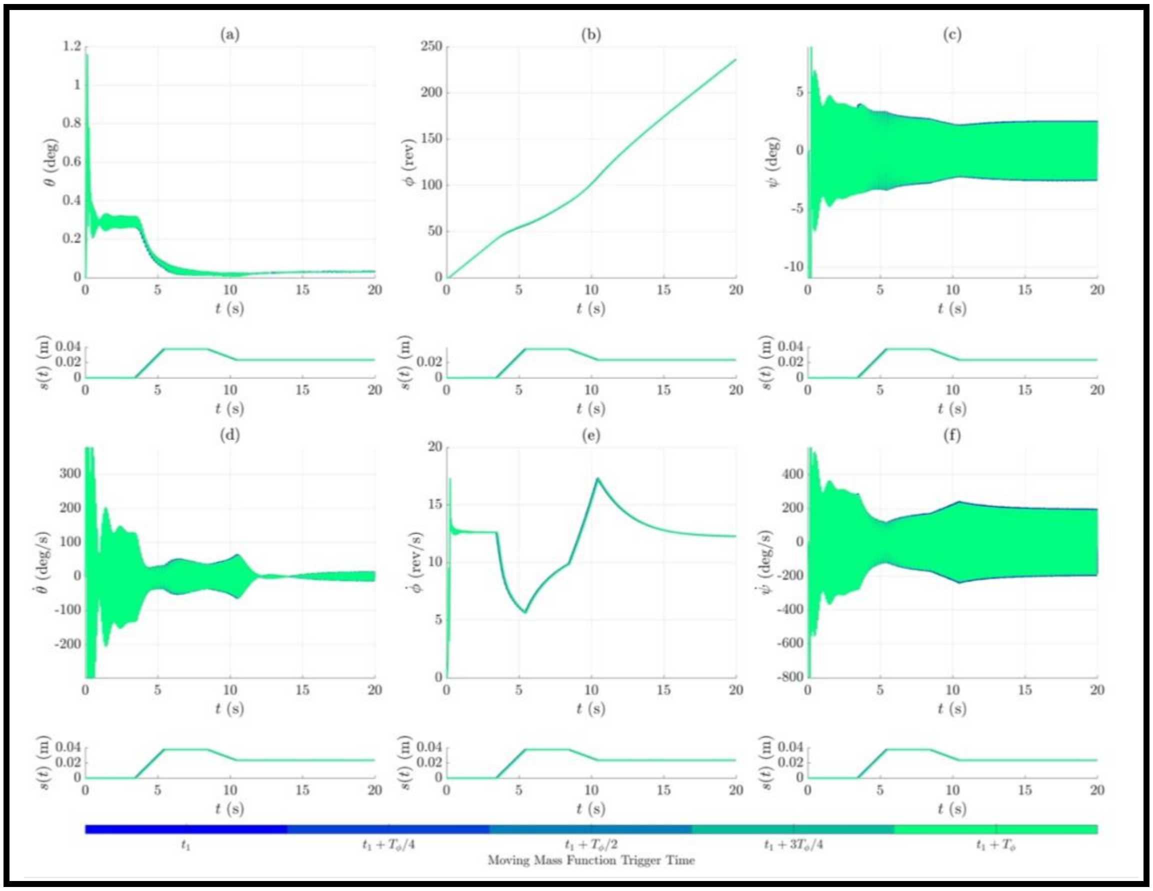

Figure 4-33. Case 3 rotational kinematics over time with varying of moving mass trigger time about samara autorotation revolution: (a) coning angle; (b) autorotational revolutions; (c) roll angle; (d) coning angle rate; (e) rotation frequency; (f) roll rate.

4.3.3.3. Case 3: Effect of Varying Trigger Time about the Precession Cycle

This section provides the results from the assessment of the effect of varying the trigger time t_1 based on varying points in the samara precession cycle period (T_P). Table 4-6 in section 4.3.1.3 shows the varying trigger times used for this assessment and the associated ϕ revolution. It also gives an indication of the phasing of T_P. The t_1 times were selected for the runs such that each run was staggered by approximately a quarter precession cycle.

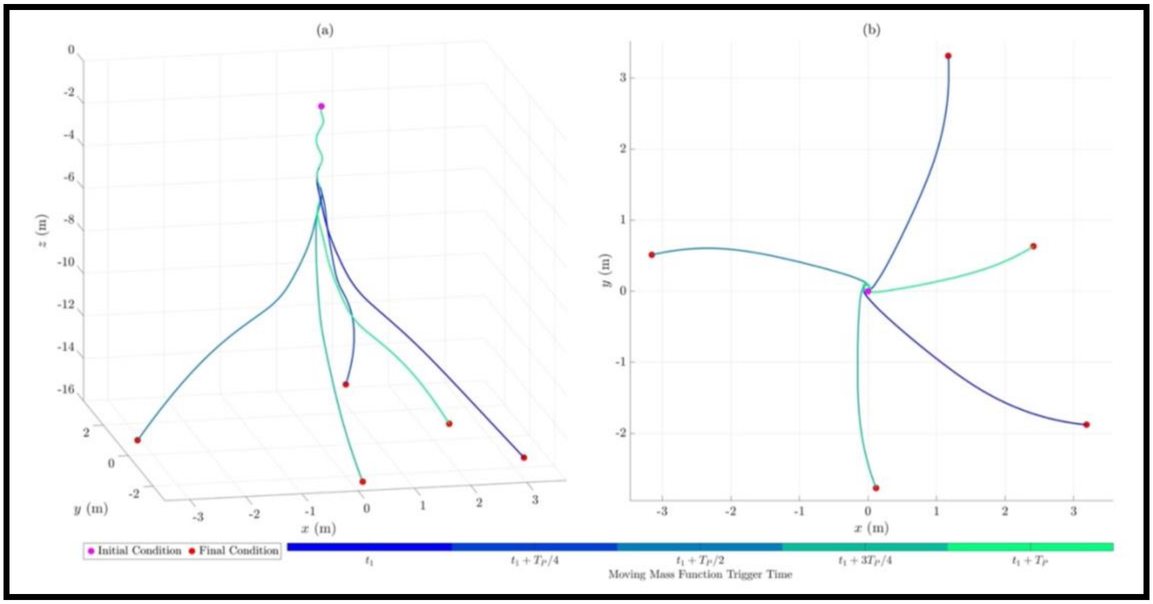

Figure 4-34. Case 3 trajectory with varying of moving mass trigger time about the precession cycle: (a) 3-dimensional view; (b) overhead view of lateral displacement.

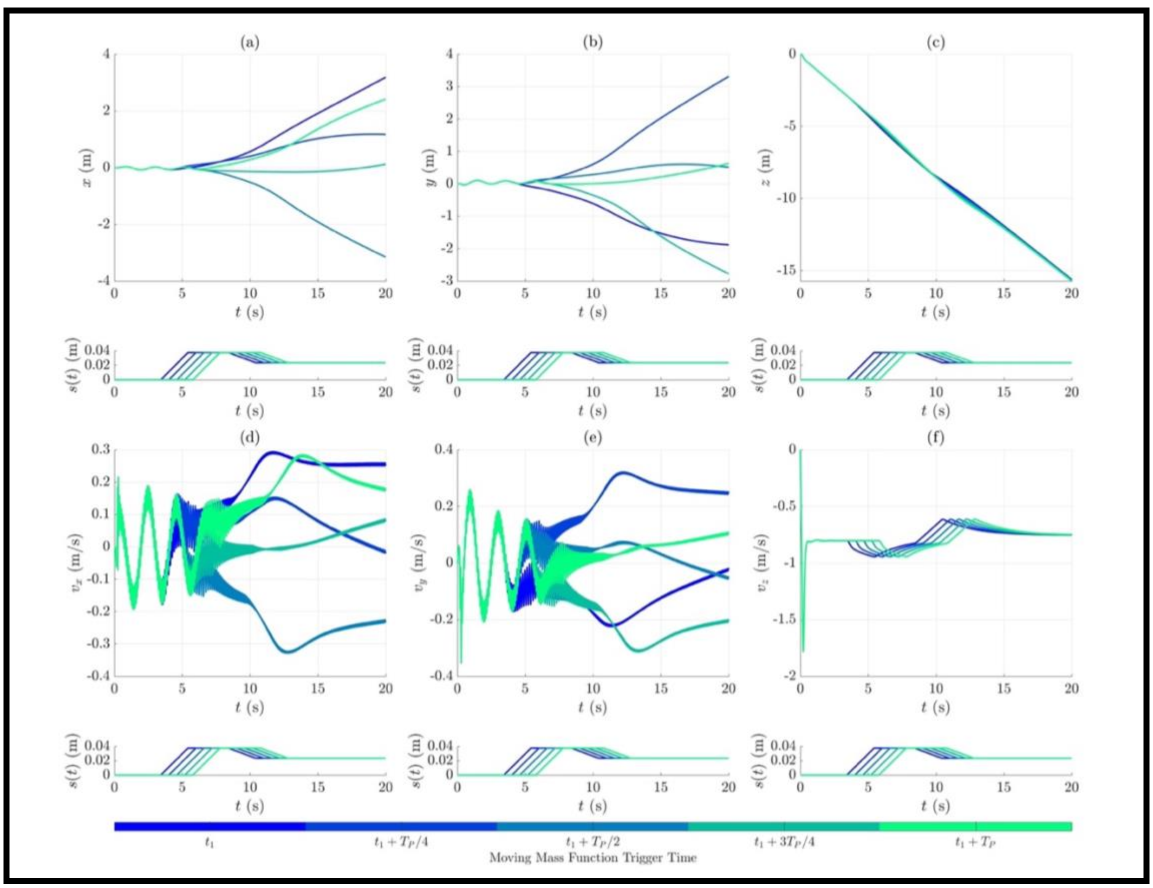

Figure 4-35. Case 3 inertial kinematics over time with varying of moving mass trigger time about the precession cycle: (a) x position; (b) y position; (c) z position; (d) x velocity component; (e) y velocity component; (f) z velocity component.

Figure 4-34 depicts the resulting trajectories from the assessment. The T_P phasing clearly has an impact to where the samara seed is displaced once the time function is activated. The only other notable feature is that the direction of the samara when released at $T_P = 1$ versus $T_P = 2$ is significantly different. Like the previous cases, this behavior is probably due to the size of these precession cycles is significantly different and can be explained by a similar phenomenon to the slingshot effect in orbital mechanics. Because the radius of the cycle at $T_P = 2$ is significantly smaller than that of $T_P = 1$, the samara will have less torque, which results in a slower release from the precession cycle once the time function is activated. Figure 4-35 and Figure 4-36 depict the inertial and rotational kinematics, respectively.

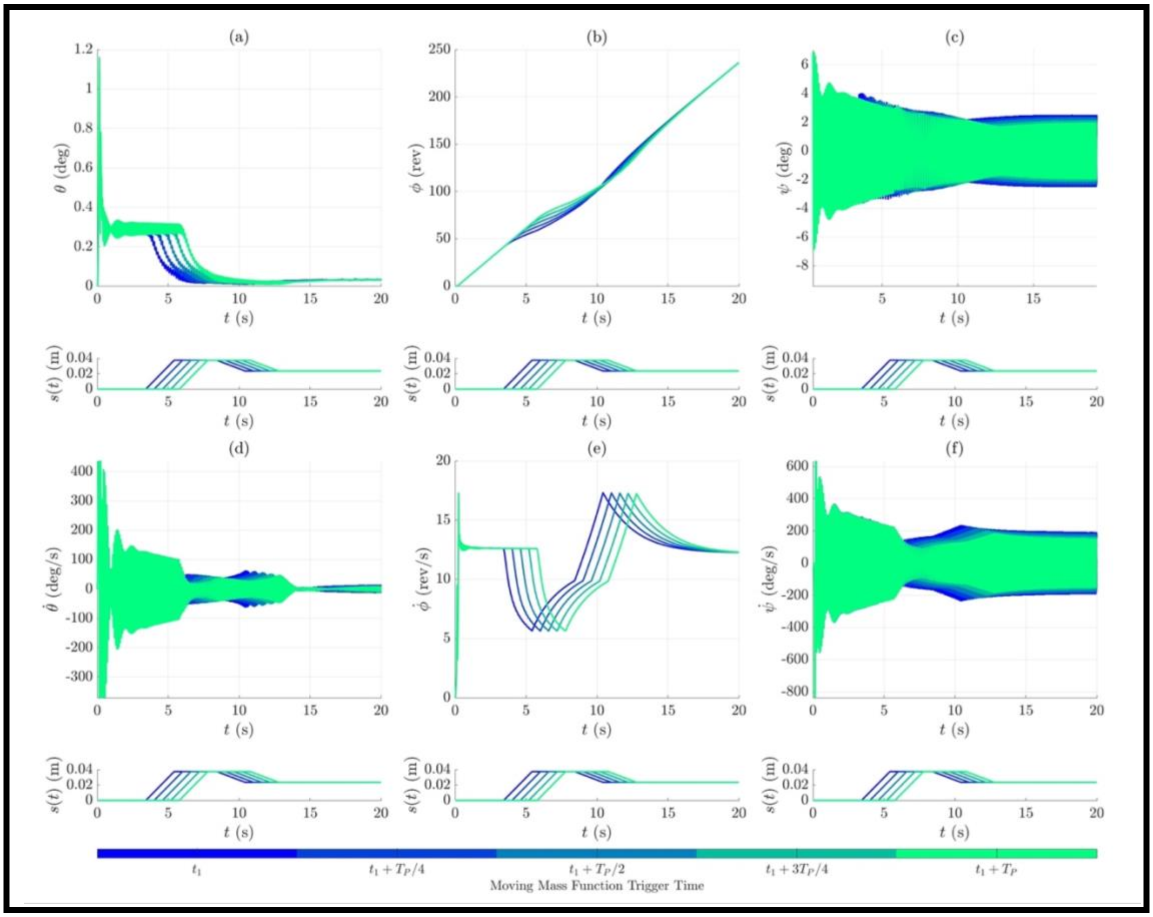

Figure 4-36. Case 3 rotational kinematics over time with varying of moving mass trigger time about the precession cycle: (a) coning angle; (b) autorotational revolutions; (c) roll angle; (d) coning angle rate; (e) rotation frequency; (f) roll rate.

4.3.4. Case 4: Sinusoidal Resonance with Samara Rotation

Case 4 can be described as a high frequency sinusoidal function, where the moving mass is modulated between the lower and upper bound of the linear rail at the rate of the autorotational frequency, attempting to somehow resonate the moving mass with the autorotational cycle. The goal of this case study is to evaluate the impact that the moving mass would have on the system if the movement resonates with the autorotational cycle. Equation (4-4) provides the mathematical expression for the function.

$$s(t) = \begin{cases} 0, & t < t_1 \\ -R_{ub}\sin(\phi - \phi_1 + \pi/2) + R_{ub}\,, & t \geq t_1 \end{cases} \tag{4-4}$$

where R_{ub} is the chosen amplitude of the sine function, t_1 is the activating trigger time for $s(t)$, and ϕ_1 is the ϕ associated with t_1. Since R_{ub} is the amplitude of the sine function, $2R_{ub}$ is the upper bound of the moving mass rail. A shorter rail than what was used in Case 1 was chosen to compensate for the burden the higher frequency oscillation generated in this case would likely have on the physical system.

Table 4-9 defines the values of the parameters used in the time function for Case 4. Figure 4-9(d) gives the graphical depiction of the Case 4 function using these parameters.

Table 4-9. Parameters used for the $s(t)$ time function for Case 4.

$s(t)$ **Parameters**	**Chosen Values for Case Study**
R_{ub}	$l/2 = 0.006$ m

4.3.4.1. Case 4: Effect of Varying Size of Moving Mass

This section provides the results to the Case 4 moving mass sizing study, which uses the mass ratios defined in Table 4-3. The $s(t)$ function trigger time used was $t_1 = 3.4263$, which is roughly the time it takes for the base model to complete one precession cycle.

Figure 4-37 depicts the resulting trajectories from this study, which all exhibit massive lateral and vertical displacement. The different runs did show some moderate difference in the vertical displacement, where the medium sized moving masses seemed to fall the quickest. Run 5 shows the optimal displacement of the samara from its initial position. As such, $m_m = 0.4m$ and $m_s = 0.45m$ are used for the subsequent Case 4 assessments.

Figure 4-38 and Figure 4-39 depict the inertial and rotational kinematics, respectively. The vertical velocity v_z reaches a terminal velocity of near 7m/s. Additionally, the rotational variables have massive spreads in the angles experienced throughout the runs. There is also significant lateral displacement (upwards of 40m from the initial position). These features indicate that the samara is tumbling. Past research has observed that tumbling can create lateral propulsion [40]. The glide ratio for Case 4 was calculated to be at least twice as great as any of the other cases explored, which likely also indicative of lateral propulsion.

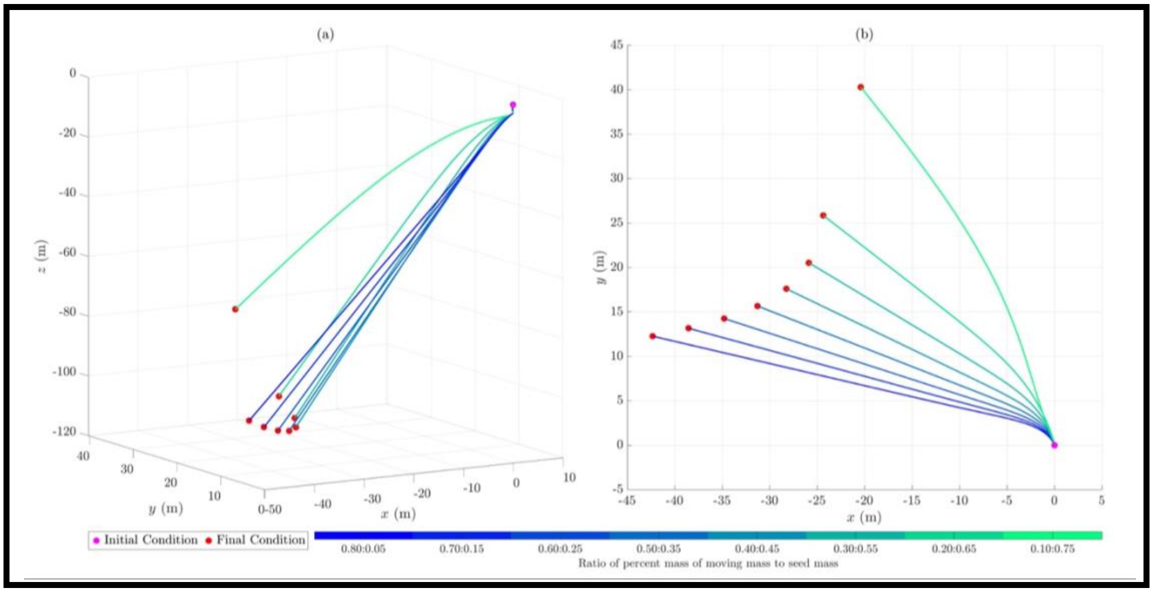

Figure 4-37. Case 4 trajectory with varying of size of moving mass: (a) 3-dimensional view; (b) overhead view of lateral displacement.

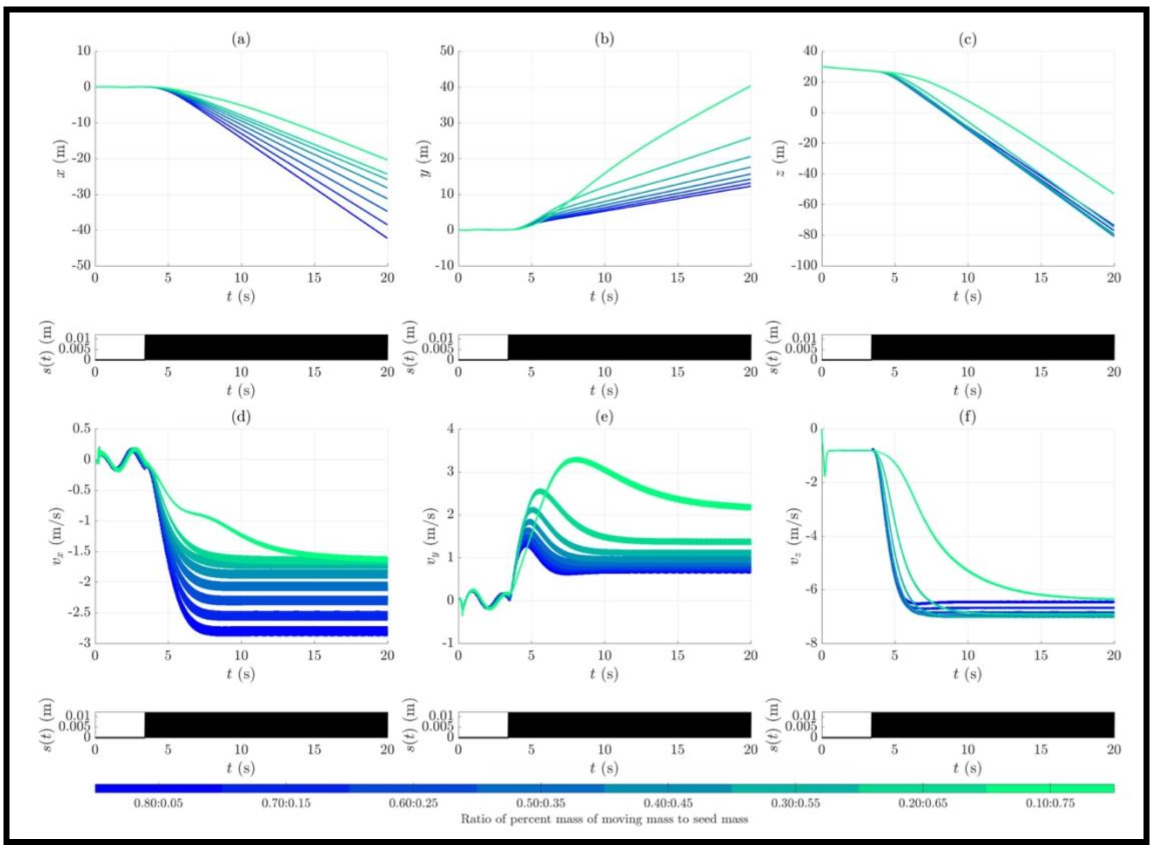

Figure 4-38. Case 4 inertial kinematics over time with varying of size of moving mass: (a) x position; (b) y position; (c) z position; (d) x velocity component; (e) y velocity component; (f) z velocity component.

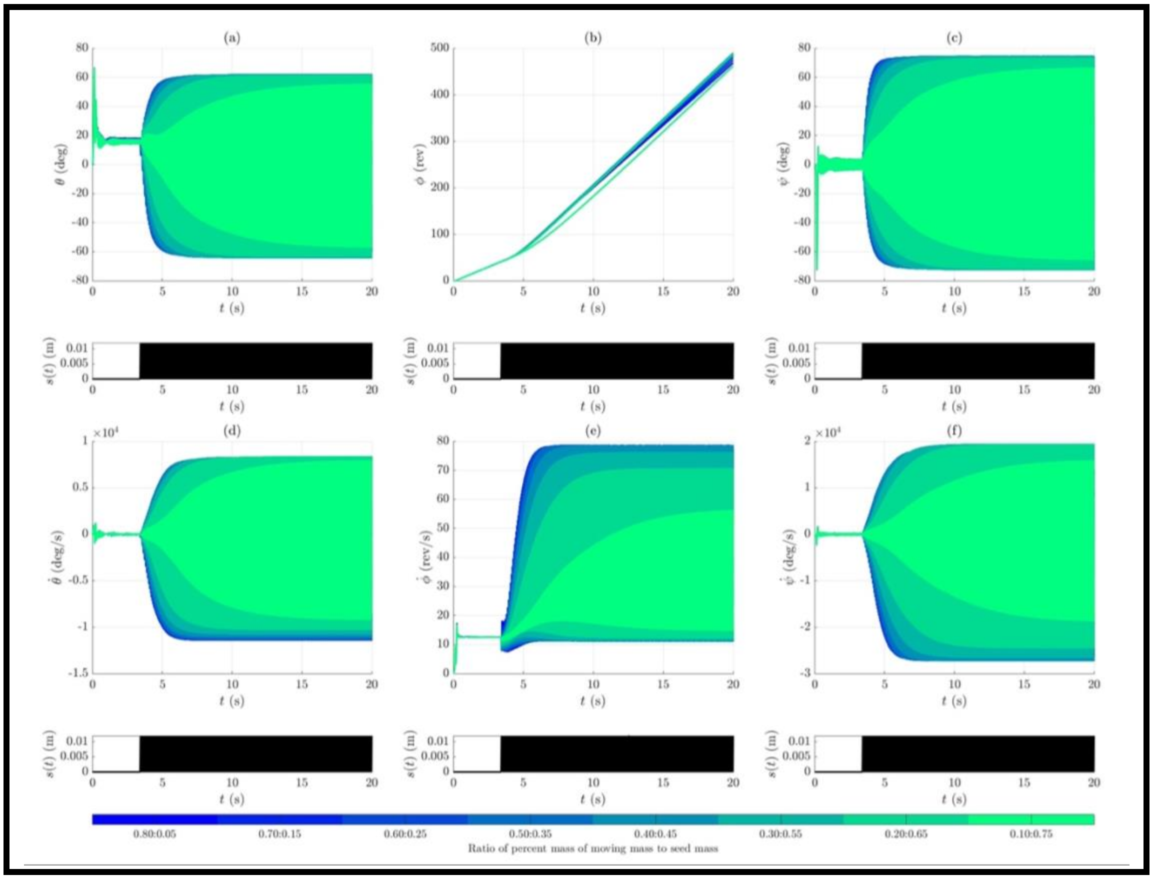

Figure 4-39. Case 4 rotational kinematics over time with varying of size of moving mass: (a) coning angle; (b) autorotational revolutions; (c) roll angle; (d) coning angle rate; (e) rotation frequency; (f) roll rate.

4.3.4.2. Case 4: Effect of Varying Trigger Time about the Samara Rotation

This section provides the results from the assessment of the effect of varying the trigger time t_1 based on varying points in the samara autorotational cycle period (T_ϕ). Table 4-5 in section 4.3.1.2 shows the varying trigger times used for this assessment and the associated ϕ revolution. The t_1 times were selected for the runs such that each run was staggered by approximately a quarter revolution of the samara.

Figure 4-40 depicts the resulting trajectories from the assessment. This is the first case out of the four considered that is impacted by T_ϕ. It appears that the lateral propulsion can be biased by the orientation of the autorotational revolution.

Figure 4-41 and Figure 4-42 depict the inertial and rotational kinematics, respectively. From the kinematics, the phasing of the time trigger based T_ϕ has negligible influence on the model variables. The x and y position and associated velocities show significant variation in the runs. This observation is in line with the trajectory plot that shows the samara being propelled in directions consistent with the quarter autorotational cycle.

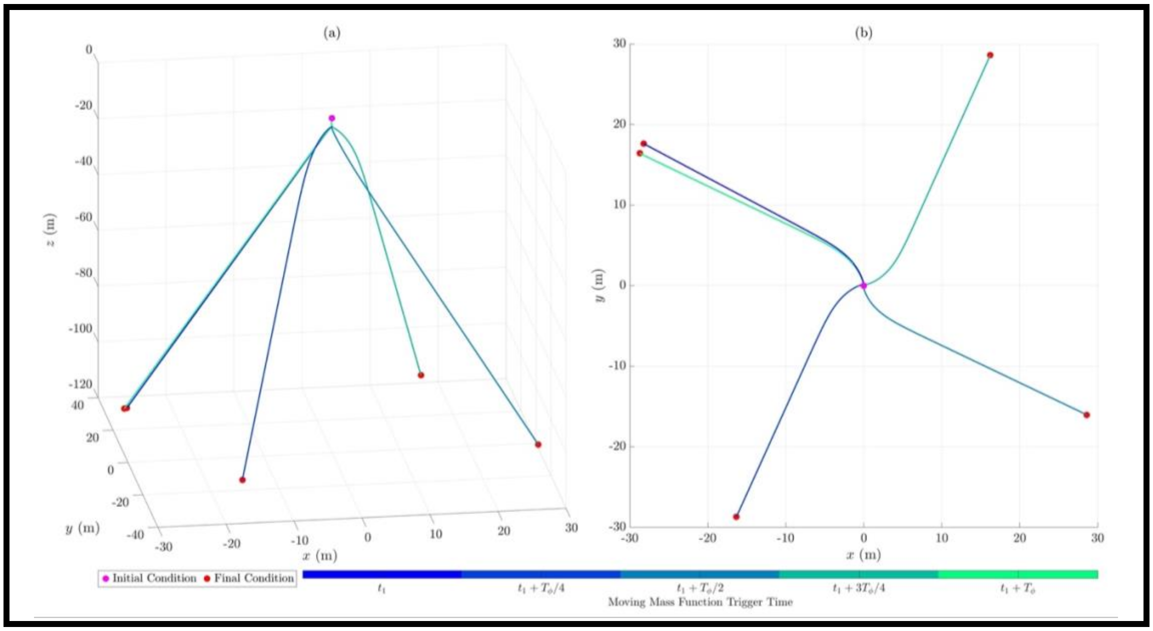

Figure 4-40. Case 4 trajectory with varying of moving mass trigger time about samara autorotation revolution: (a) 3-dimensional view; (b) overhead view of lateral displacement.

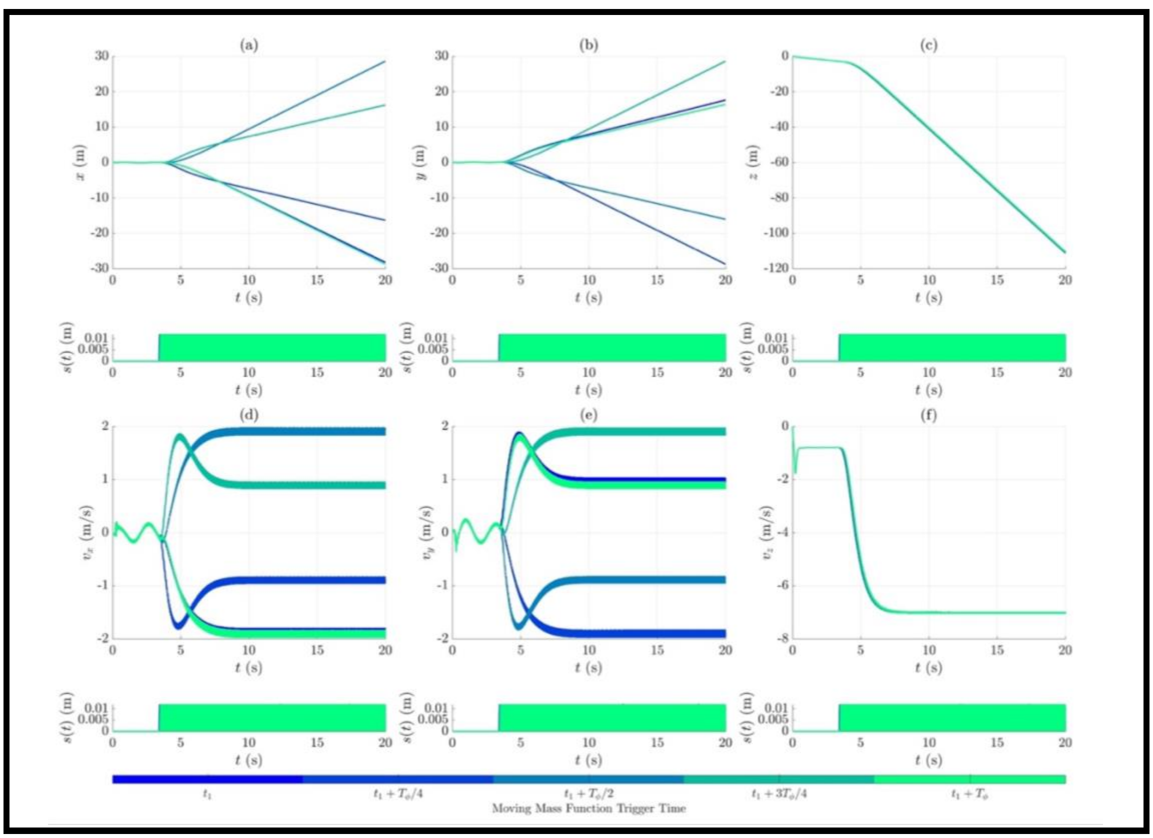

Figure 4-41. Case 4 inertial kinematics over time with varying of moving mass trigger time about samara autorotation revolution: (a) x position; (b) y position; (c) z position; (d) x velocity component; (e) y velocity component; (f) z velocity component.

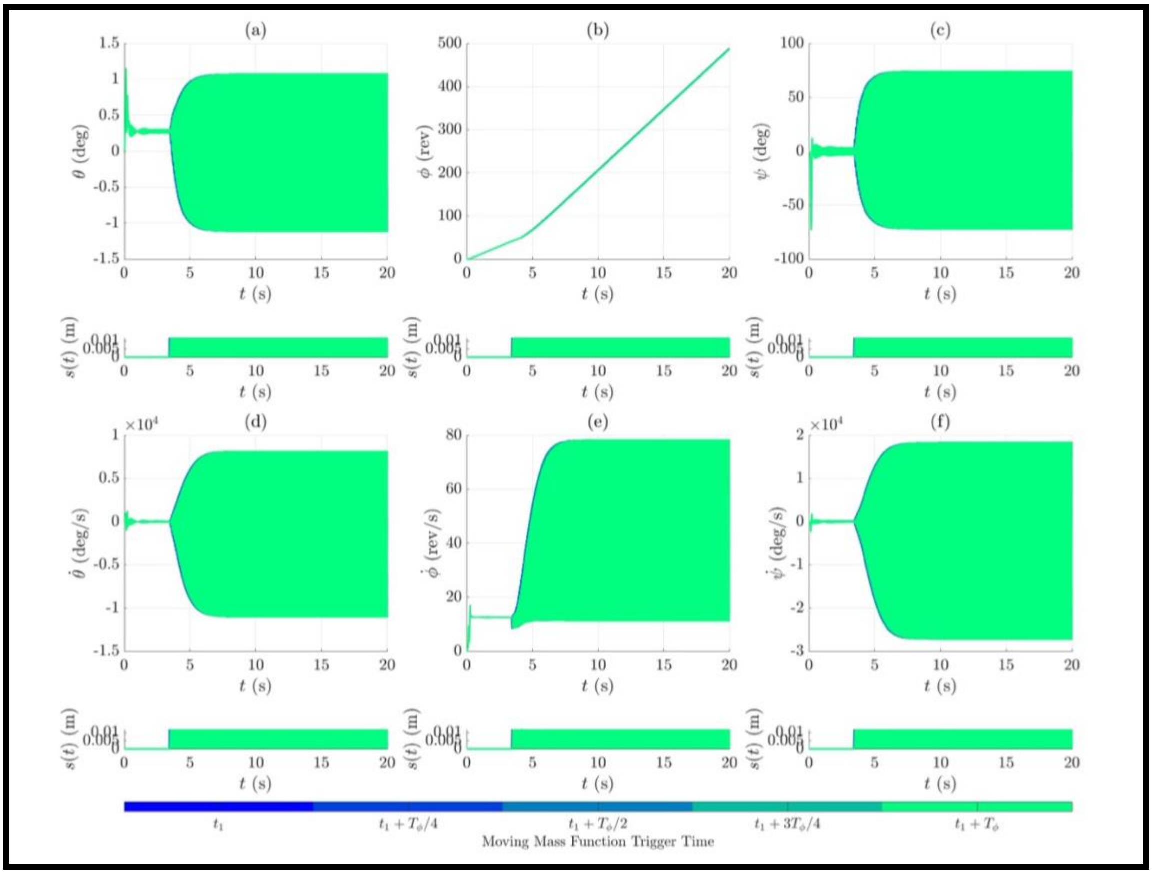

Figure 4-42. Case 4 rotational kinematics over time with varying of moving mass trigger time about samara autorotation revolution: (a) coning angle; (b) autorotational revolutions; (c) roll angle; (d) coning angle rate; (e) rotation frequency; (f) roll rate.

4.3.4.3. Case 4: Effect of Varying Trigger Time about the Precession Cycle

This section provides the results from the assessment of the effect of varying the trigger time t_1 based on varying points in the samara precession cycle period (T_P). Table 4-6 in section 4.3.1.3 shows the varying trigger times used for this assessment and the associated ϕ revolution. It also gives an indication of the phasing of T_P. The t_1 times were selected for the runs such that each run was staggered by approximately a quarter precession cycle.

Figure 4-43 depicts the resulting trajectories from the assessment. The T_P phasing clearly has an impact to where the samara seed is displaced once the time function is activated; however, the direction of lateral displacement is not as intuitive as the phasing of T_ϕ. It is possible that because the phasing of T_ϕ is the dominating factor in determining the direction of lateral displacement, the difference in ϕ_1 values used for the different runs as depicted in Table 4-6 could be driving the direction of lateral displacement. A secondary effect could also be linked to the gradual reduction in precession cycle size, which has shown to have impact on the lateral displacement in the other cases.

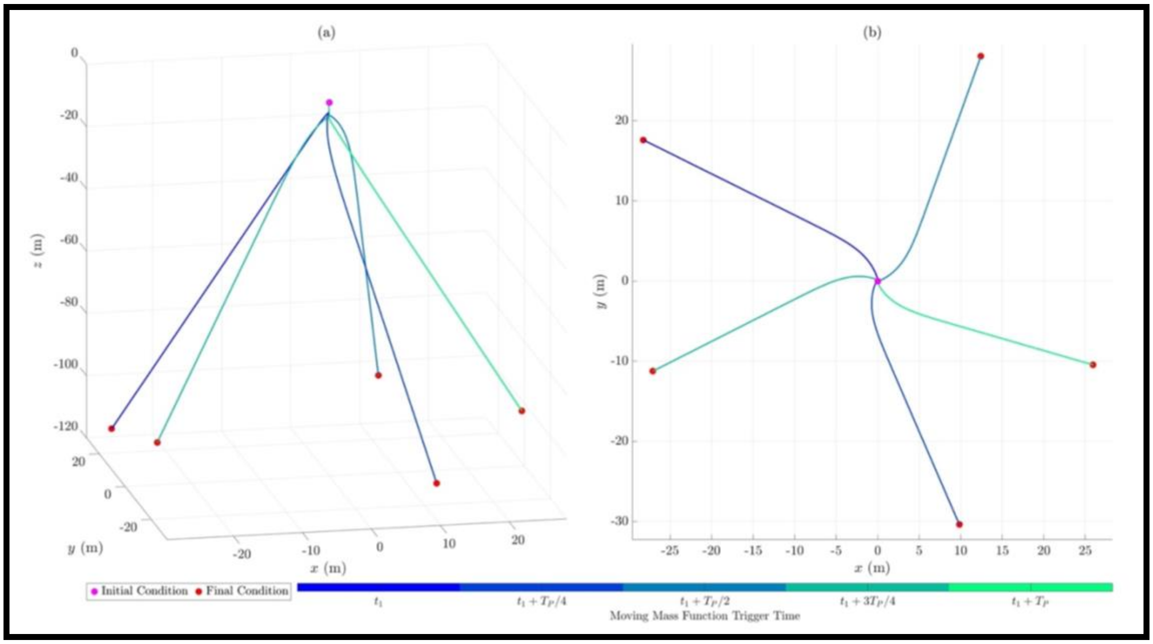

Figure 4-43. Case 4 trajectory with varying of moving mass trigger time about the precession cycle: (a) 3-dimensional view; (b) overhead view of lateral displacement.

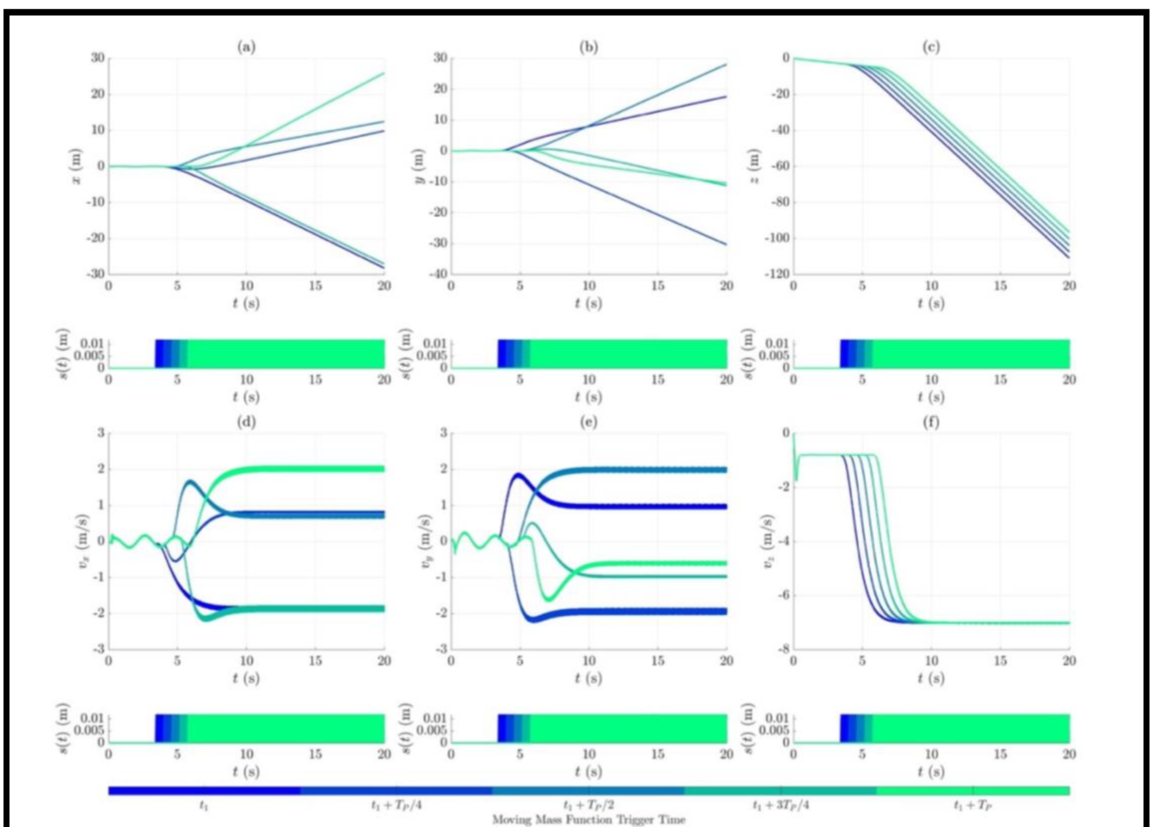

Figure 4-44. Case 4 inertial kinematics over time with varying of moving mass trigger time about the precession cycle: (a) x position; (b) y position; (c) z position; (d) x velocity component; (e) y velocity component; (f) z velocity component.

Figure 4-44 and Figure 4-45 depict the inertial and rotational kinematics, respectively.

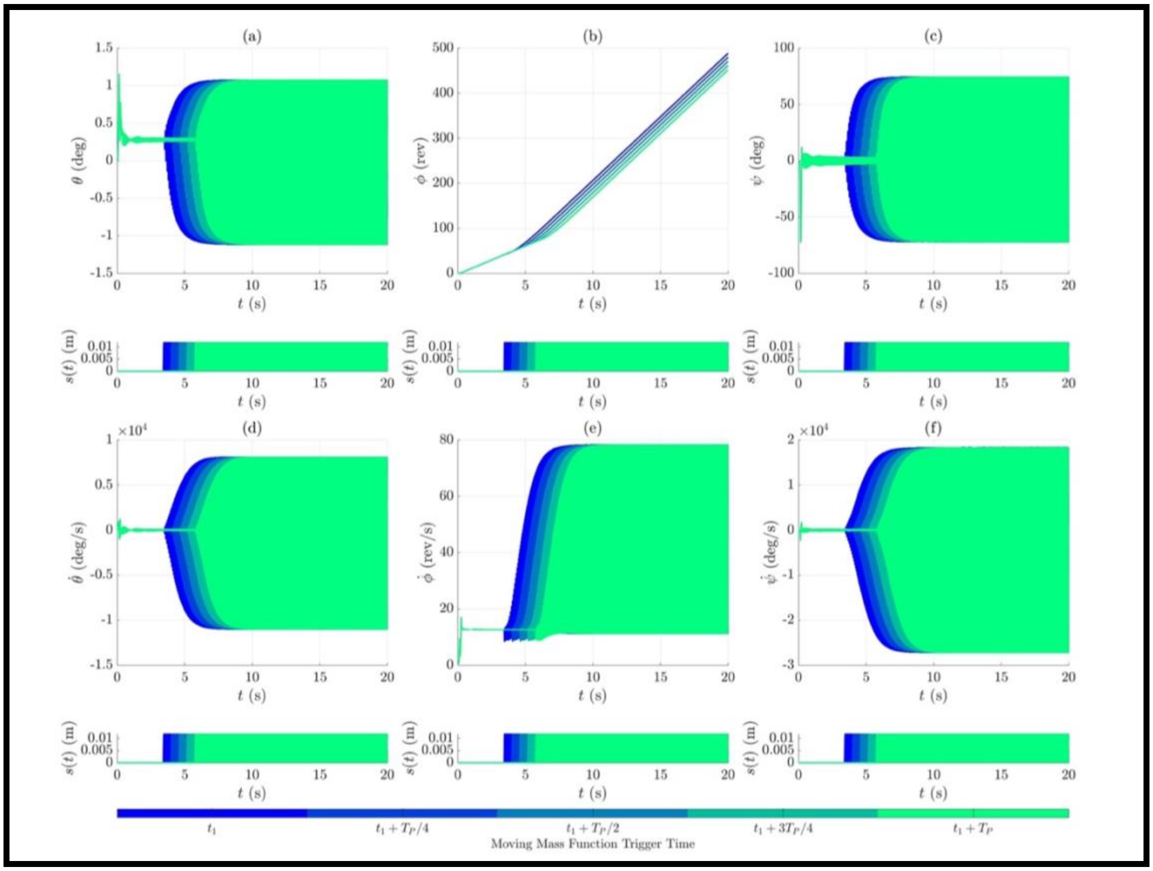

Figure 4-45. Case 4 rotational kinematics over time with varying of moving mass trigger time about the precession cycle: (a) coning angle; (b) autorotational revolutions; (c) roll angle; (d) coning angle rate; (e) rotation frequency; (f) roll rate.

Chapter 5. Discussion of Engineering Application

The findings from the case studies shown in Chapter 4 indicate that varying the mass distribution of an inflight samara can impact both trajectory and rate of descent, which is a positive indication that MMC could work on a samara-inspired vehicle.

Case 1 through Case 3 showed two driving features associated with the time-varying functions that impacted the final lateral position of the samara. First, the duration of time spent at the upper bound of the rail seemed to cause a slow creep in a biased direction. Case 3 showed the greatest lateral displacement, which is reasonable since the moving mass was either partially or fully extended for the greatest amount of time; however, due to the positioning of the moving mass potentially causing the samara to enter a chaotic mode of flight [33], which is likely why the greatest amount of mass needed to be applied to the moving mass in order to keep the direction of the samara somewhat stable. Even with 80% of the mass applied to the moving mass, the trajectory of Case 3 still bent in flight. As a result, there exists a risk that the moving mass function may be challenging to implement as a controller for Case 3. Case 1 made the next largest lateral displacement, and the low-rate sinusoidal extension may provide a more stable controller since the repeated contraction allows the samara to restabilize. As a side effect of the sinusoidal function, a curlicue behavior was introduced that is not ideal for controlling direction, especially because the constant oscillation of the moving mass makes the curlicue less predictable. Case 2 showed the smoothest displacement function, but it also traveled the least amount of distance, although the function was only turned on for approximately 5 seconds. Figure 5-1 shows that increasing the time in the extended position allows for a comparable displacement to the other cases. However, like Case 3, the trajectory experiences a substantial bend, which would create a challenge for vehicle control.

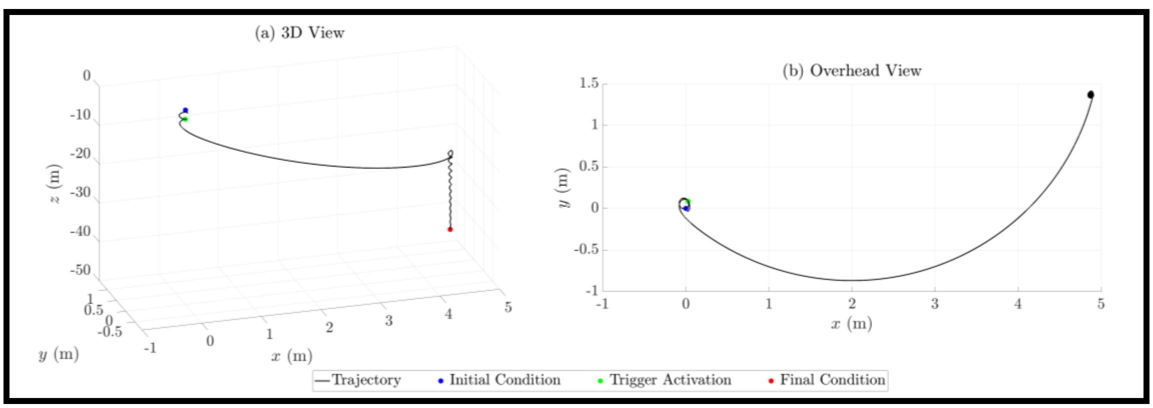

Figure 5-1. Case 2 trajectory with moving mass in extended position for 6x longer duration: (a) 3-dimensional view; (b) overhead view of lateral displacement.

While also experiencing significant lateral translation, Case 4 demonstrated that the relatively slow rate of descent of an autorotating samara can be disrupted by a time-varying mass distribution. The Case 4 simulation indicated that the extremely rapid oscillation of the moving mass likely caused the samara to tumble, reaching a terminal velocity that was nearly $1g$. Despite the high terminal velocity, it is possible in extremely short bursts, Case 4 could be used to displace the vehicle more quickly without losing too much altitude. Separately, this rapid descent has the capability of swiftly terminating flight. The disadvantage to using this function as a termination function is that there is a high level of lateral propulsion as a side effect. The other disadvantage to Case 4 is the extremely rapid modulation frequency of the moving mass. Although the reason this case was originally explored was to characterize the behavior of the moving mass frequency resonating with the autorotational cycle. It is postulated that the same behavior could be accomplished with a more manageable constant frequency sinusoidal function that would reduce burden on the mechanical system.

Ideally, a termination function could cause the samara to enter a quick vertical fall. Past research into the effects of mass distribution on the samara discovered that a vertical fall could be achieved if the mass is distributed appropriately [33]. Although failing to achieve an increased rate of descent, Case 3 would be an ideal candidate to explore the mass distribution sweet spot for a falling mode. Future research could explore tuning the final position of the moving mass. Depending on the success of simply tuning the final position of the Case 3 moving mass time function, it may be necessary to explore changing the orientation of the moving mass linear rail inside the samara vehicle design to optimize which sweet spot across the samara are available to use.

All four cases were able to change the biased direction to where the samara was displaced. Case 1 through Case 3 demonstrated that there is a direct correlation between the lateral direction of biased displacement and where the samara was in the precession cycle when the time-varying function was activated. While still being impacted to some degree by the precession cycle like the other cases, a better indicator of direction for Case 4 was the orientation of the samara in terms of its autorotational cycle when the time-varying function is triggered.

Based on the findings that the position and direction of the samara can be affected by a moving mass, there are two methods of control that can be used to steer the samara in flight: open-loop control and feedback control. Open-loop control is the simpler and least computationally expensive option that could be used and would implement a pre-planned time-varying function. The $s(t)$ function would be programmed in advanced based on mission needs. When the samara inspired vehicle is released, the function would be triggered. This would be an ideal choice for the sensor distribution applications. For this application, multiple seeds are likely dropped at the same time from a high altitude, and the goal would be to optimize the distribution, which could be done by phasing the time-varying function.

For feedback control, some of the samara inspired designs have already used feedback control set-ups, where position and orientation sensors were used to inform the actuation of the vehicles [22]. Implementing feedback control in this context would use the same concept, the only difference is that the moving mass is the actuator for the system. This would be an ideal choice for the package delivery use cases, where the goal would be to airdrop a package from a high altitude and steer the package to a target destination. While many of the samara-inspired vehicles have been on the same size scale as natural samaras, a recent study revealed that the size of the samara can be scaled to a larger size (2x the size for as good or better stability, and up to 8x still being able to autorotate with some degraded performance) [68].

A possible starting point for refining a moving mass function is to use Case 2, which could be used to laterally translate and turn corners depending on how the function is switched on and off. To avoid the bending behavior that is observed in Figure 5-1, the shorter, repeated use of the Case 2 time function demonstrates a more controlled trajectory. While the length of time that the moving mass can spend in the extended position on the rail without causing significant bending in trajectory likely varies with the physical design of the vehicle, it was found with the specific samara design used in this study that the moving mass could last roughly 5 to 8 seconds in the extended position before the samara saw significant deviation in direction. Allowing the samara to settle back into a steady state precession cycle enables the samara to have subsequent short iterative lateral movements, either in the same direction or turning to a new direction depending on when the time triggers are initiated.

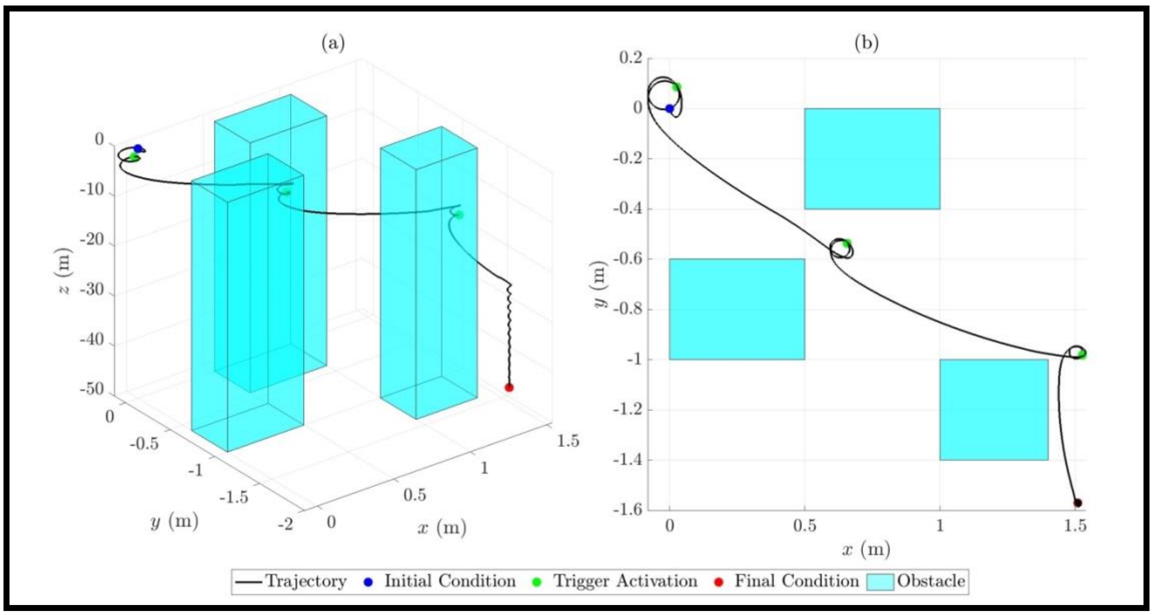

Figure 5-2. Example programmed time function that navigates samara vehicle through a series of obstacles: (a) 3-dimensional view; (b) overhead view of lateral displacement.

Figure 5-2 demonstrates how this approach can navigate the samara through a series of obstacles, which shows three consecutive time triggers. The first two moving mass triggers push the samara in the same direction, allowing the samara to travel farther in a controlled direction than what would be possible with one longer time function. The third moving mass trigger shows that the samara making a sharp turn. A primary disadvantage to this design is that the lateral displacement achieved is relatively small compared to the significant vertical displacement that is needed. Past samara vehicle designs have leveraged thrusters [23] [24] [25] and propellers [26] [57] on the wing to aid in vertical lift, which could help this design travel farther without losing too much altitude.

The last consideration that needs to be examined for future design trades is the size of the moving mass. It could be seen from the four case studies that the time function selected has varying impacts on the size of the moving mass needed. Case 3 required moving mass to have the largest percentage of the overall mass of the samara out of the four cases with 80% of the mass allocated to the moving mass. Case 1 needed less with 60% of the total samara mass being allocated to the moving mass. Case 2 and Case 4 required the least with 40% of the total samara mass being allocated to the moving mass. Particularly for the package delivery use case, mass needs to be reserved for the material being delivered in the package. Additionally, for any design, there is likely going to be avionics hardware that needs to be accounted for in the mass budget. Therefore, the goal in this design trade would be to minimize the size of the moving mass while still being able to accomplish the intended mission.

Chapter 6. Conclusion

A six degree of freedom time-varying triple-mass rigid body model was derived for a samara-inspired vehicle with a moving mass actuator on a linear rail to assess the possible use of MMC in future samara autorotating wing vehicle design. For the model, BET was used to define the forces and moments used for the equations of motion. The model was then verified against existing published literature. The results of four case studies demonstrated the ability to laterally displace the samara as well as affect the biased direction of the displacement. Case 4 also showed a rough first pass at a termination function, but future work would be needed to find a function that causes the samara to quickly fall vertically versus a lateral tumble. Based on the results, MMC should be considered as a future design option for samara-inspired vehicles.

With this being the first documented work studying the dynamics of a moving mass actuator on a samara inspired vehicle, there is plenty of opportunity for future work. First, additional work can be done to make the dynamic model more robust. Many of the simplifying assumptions used by McConnell and Das were carried over to this model; however, there is a significant amount of research available that could be leveraged to improve the model, to include more sophisticated lift and drag coefficients that better incorporate LEV. A more sophisticated computer aided design of the samara could also be developed and used to define more precise moments of inertia. Additionally, a wind profile function could be added to start to evaluate how the moving mass could perform outside a benign environment. The second area of future work could focus on the case studies, looking for ways to optimize performance, potentially looking for better moving mass functions, changing parameters like length of the rail, speed of ramps, and where to place the moving mass to trigger different descent modes. Lastly, a third area of future work could be focused on designing and prototyping a samara inspired vehicle with a moving mass actuator in order to validate this model.

References

[1] J. McConnell, "A Study of Autorotation: Samara Seed Pods and Tethered Autogyros," Orlando, FL, 2022.

[2] J. McConnell and T. Das, "Control Oriented Modeling, Experimentation, and Stability Analysis of an Autorotating Samara," *Journal of Dynamic Systems, Measurement, and Control,* vol. 145, no. 6, 15 May 2023.

[3] J. McConnell and T. Das, "Reduced Order Modeling of an Autorotating Samara for Steady-State and Dynamic Analysis," *IFAC-PapersOnLine,* vol. 55, no. 37, pp. 68-73, 2022.

[4] K. Varshney, S. Chang and Z. J. Wang, "The kinematics of falling maple seeds andthe initial transition to a helical motion," *Nonlinearity,* vol. 25, no. 1, 15 December 2011.

[5] G. Arranz, M. Moriche, M. Uhlmann, O. Flores and M. García-Villalba, "Kinematics and dynamics of the auto-rotation of a model winged seed," *Bioinspiration & Biomimetics,* vol. 13, no. 3, 2018.

[6] G. K. J. Nave, N. Hall, K. Somers, B. Davis, H. Gruszewski, C. Powers, M. Collver, D. G. Schmale, III and S. D. Ross, "Wind Dispersal of Natural and Biomimetic Maple Samaras," *Biomimetics,* vol. 6, no. 2, 2021.

[7] P. Pounds and S. Singh, "Samara: Biologically Inspired Self-Deploying Sensor Networks," *IEEE Potentials,* vol. 34, no. 2, pp. 10-14, 2015.

[8] P. B. Chilson, T. M. Bell, K. A. Brewster, G. B. Hupsel de Azevedo, F. H. Carr, K. Carson, W. Doyle, C. A. Fiebrich, B. R. Greene, J. L. Grimsley, S. T. Kanneganti, J. Martin and A. Moore, "Moving towards a Network of Autonomous UAS Atmospheric Profiling Stations for Observations in the Earth's Lower Atmosphere: The 3D Mesonet Concept," *Sesors (Basel),* vol. 19, no. 12, 17 June 2019.

[9] L. Barbieri, S. T. Kral, S. C. C. Bailey, A. E. Frazier, J. D. Jacob, J. Reuder, D. Brus, P. B. Chilson, C. Crick, C. Detweiler, A. Doddi, J. Elston, H. Foroutan, J. González-Rocha and Green, "Intercomparison of Small Unmanned Aircraft System (sUAS) Measurements for Atmospheric Science during the LAPSE-RATE Campaign," *Sensors,* vol. 19, no. 9, 2019.

[10] T. R. Lee, M. Buban, E. Dumas and B. Baker, "On the Use of Rotary-Wing Aircraft to Sample Near-Surface Thermodynamic Fields: Results from Recent Field Campaigns," *Sensors,* vol. 19, no. 1, 2019.

[11] S. Rabinovich, R. E. Curry and G. H. Elkaim, "Toward Dynamic Monitoring and Suppressing Uncertainty in Wildfire by Multiple Unmanned Air Vehicle System," *Journal of Robotics,* vol. 2018, 2018.

[12] F. T. Al-Dhief, N. Sabri, S. Fouad, N. A. Latiff and M. A. A. Albader, "A review of forest fire surveillance technologies: Mobile ad-hoc network routing protocols perspective," *Journal of King Saud University - Computer and Information Science,* vol. 31, no. 2, pp. 135-146, 2019.

[13] T. F. Villa, F. Gonzalez, B. Miljievic, Z. D. Ristovski and L. Morazska, "An Overview of Small Unmanned Aerial Vehicles for Air Quality Measurements: Present Applications and Future Prospectives," *Sensors,* vol. 16, no. 7, 2016.

[14] V. Carranza, T. Rafiq, I. Frausto-Vicencio, F. M. Hopkins, K. R. Verhulst, P. Rao, R. M. Duren and C. E. Miller, "Vista-LA: Mapping methane-emitting infrastructure in the Los Angeles megacity," *Earth System Science Data,* vol. 10, no. 1, 2018.

[15] D. G. Schmale, III, A. P. Ault, W. Saad, D. T. Scott and J. A. Westrick, "Perspectives on Harmful Algal Blooms (HABs) and the Cyberbiosecurity of Freshwater Systems," *Frontiers in Bioengineering and Biotechnology,* vol. 7, 2019.

[16] J. K. Hart and K. Martinez, "Environmental Sensor Networks: A revolution in the earth system science?," *Earth-Science Reviews,* vol. 78, no. 3, pp. 177-191, 2006.

[17] A. Barrientos, J. Colorado, J. del Cerro, A. Martinez, C. Rossi, D. Sanz and J. Valente, "Aerial remote sensing in agriculture: A practical approach to area coverage and path planning for fleets of mini aerial robots," *Journal of Field Robots,* vol. 28, no. 5, pp. 667-689, 2011.

[18] NASA, "Titan Aerial Research Vehicle for Scientific Exploration," 22 January 2026. [Online]. Available: https://techport.nasa.gov/projects/102052. [Accessed 11 April 2026].

[19] C. Pandolfi and D. Izzo, "Biomimetics on seed dispersal: survey and insights for space exploration," *Bioinspiration & Biomimetics,* vol. 8, no. 2, 2013.

[20] N. Pilling, "Following an earthquake, could the supplies you need be delivered by a cardboard copter?," 25 October 2023. [Online]. Available: https://www.kitsapsun.com/story/news/local/2023/10/25/seattle-startup-five-forces-airwing-system-natural-disaster-delivery/71293165007/. [Accessed 20 April 2026].

[21] five forces, "We Solve Logistic Problems for Humanitarian Relief," [Online]. Available: https://www.fiveforces.co/. [Accessed 20 April 2026].

[22] A. Kellas, "The Guided Samara: Design and Development of a Controllable Single-Bladed Autorotating Vehicle," Cambridge, MA, 2007.

[23] K. Fregene and C. Bolden, "Dynamics and control of a biomimetic single-wing nano air vehicle," in *Proceedings of the 2010 American Control Conference*, 2010.

[24] H. Youngren, S. Jameson and B. Satterfield, "Design of the SAMARAI Monowing Rotorcraft Nano Air Vehicle," 27 May 2009. [Online]. Available: https://api.semanticscholar.org/CorpusID:15922154. [Accessed 11 April 2026].

[25] S. Jameson, B. Satterfield, C. Bolden, N. Allen and H. Youngren, "SAMARAI Nano Air Vehicle – A Revolution in Flight," [Online]. Available: https://assets.newatlas.com/archive/1448.pdf. [Accessed 11 April 2026].

[26] J. Houghton and W. Hoburg, "Fly-by-wire Control of a Monocopter," 2008.

[27] E. R. Ulrich, D. J. Pines and J. S. Humbert, "From falling to flying: the path to powered flight of a robotic samara nano air vehicle," *Bioinspiration & Biomimetics,* vol. 5, no. 4, 2010.

[28] E. R. Ulrich, J. S. Humbert and D. J. Pines, "Pitch and Heave Control of Robotic Samara Micro Air Vehicles," *Journal of Aircraft,* vol. 47, no. 4, pp. 1290-1299, 2010.

[29] S. K. H. Win, L. S. T. Win, G. S. Soh and S. Foong, "Design, modelling and control of collaborative samara autorotating wings (SAW)," *International Journal of Intelligent Robotics and Applications Online,* vol. 3, no. 2, p. 144–157, 2019.

[30] S. K. H. Win, L. S. T. Win, D. Sufiyan, G. S. Soh and S. Foong, " An Agile Samara-Inspired Single-Actuator Aerial Robot Capable of Autorotation and Diving," *IEEE Transactions on Robotics,* vol. 38, no. 2, p. 1033–1046, 2022.

[31] S. K. H. Win, L. S. T. Win, D. Sufiyan and S. Foong, "Design and control of the first foldable single-actuator rotary wing micro aerial vehicle," *Bioinspiration & Biomimetics,* vol. 16, no. 6, 2021.

[32] X. Cai, S. Zhong, T. M. Tan, W. J. Ang and S. Foong, "Design and Optimization of a Samara-Inspired Lightweight Monocopter for Extended Endurance," *IEEE Robotics and Automation Letters,* vol. 10, no. 7, p. 7214–7221, 2025.

[33] Z.-B. Hou, J.-D. Zhang, Y.-D. Li, Y.-X. Jia and W.-X. Huang, " Aerodynamic significance of mass distribution on diverse samara descent behaviors," *Communications engineering,* vol. 4, no. 1, 2025.

[34] B.-G. Kwon and M.-H. Sohn, "Effects of the CG Positions on the Autorotative Flight of Maple Seeds," *International Journal of Aeronautical and Space Sciences,* vol. 23, no. 2, p. 241–254, 2022.

[35] E. H. Smith, "AUTOROTATING WINGS: AN EXPERIMENTAL INVESTIGATION," University Microfilms, Inc., Ann Arbor, 1970.

[36] Å. R. Norberg, "AUTOROTATION, SELF-STABILITY, AND STRUCTURE OF SINGLE-WINGED FRUITS AND SEEDS (SAMARAS) WITH COMPARATIVE REMARKS ON ANIMAL FLIGHT," *Biological Reviews,* vol. 48, no. 4, pp. 561-596, 1973.

[37] C. K. Augspurger, "MORPHOLOGY AND DISPERSAL POTENTIAL OF WIND-DISPERSED DIASPORES OF NEOTROPICAL TREES," *American Journal of Botany,* vol. 73, no. 3, pp. 353-363, 1986.

[38] C. K. Augspurger and S. E. Franson, "Wind Dispersal of Artifical Fruits Varying in Mass, Area, and Morphology," *Ecology,* vol. 68, no. 1, pp. 27-42, 1987.

[39] D. S. Green, "The Terminal Velocity and Dispersal of Spinning Samaras," *American Journal of Botany,* vol. 67, no. 8, pp. 1218-1224, 1980.

[40] B. M. Schaeffer and A. K. Dickerson, "Precession dynamics and morphology of rolling samaras," *Journal of the Royal Society Interface,* vol. 230, no. 22, 2025.

[41] E. R. Ulrich and D. J. Pines, "Effects of Planform Geometry on Mechanical Samara Autorotation Efficiency and Rotational Dynamics," *Journal of the American Helicopter Society,* vol. 57, no. 1, pp. 1-10, 2012.

[42] B. M. Schaeffer, S. S. Truman, T. T. Truscott and A. K. Dickerson, "Maple samara flight is robust to morphological perturbation and united by a classic drag model," *Communications biology,* vol. 7, no. 2, 2024.

[43] S. Sparsh, "Data Driven Analysis of Samara Seed Kinematics and Dynamics," San Luis Obispo, 2025.

[44] B. K. Jung and D. Rezgui, "Experimental study into the effects of pitch and coning angles on the flight performance of the natural samara," *Royal Society Open Science,* vol. 11, no. 9, 2024.

[45] E.-J. Lee and S.-J. Lee, "Effect of initial attitude on autorotation flight of maple samaras (Acer palmatum)," *Journal of Mechanical Science and Technology,* vol. 30, no. 2, p. 741–747, 2016.

[46] V. M. Ortega-Jimenez, N. S.-W. Kim and R. Dudley, " Superb autorotator: rapid decelerations in impulsively launched samaras," *Journal of the Royal Society Interface,* vol. 16, no. 150, 2019.

[47] L. Dong, G. Wen and A. Rinoshika, " Particle image velocimetry measurements of the flow structures induced by the free-falling spin flight of maple seeds," *Transactions of the Institute of Measurement and Control,* vol. 45, no. 4, pp. 700-710, 2023.

[48] G. Yogeshwaran, S. M. Rao and G. Jagadeesh, "Dynamics of wingtip vortex in natural samaras," *Physics of fluids ,* vol. 36, no. 12, 2024.

[49] S. J. Lee, E. J. Lee and M. H. Sohn, "Mechanism of autorotation flight of maple samaras (Acer palmatum)," *Experiments in Fluids,* vol. 55, no. 4, 2014.

[50] H. Seifi Davari, R. M. Botez, M. Seify Davari and H. Chowdhury, "Wind Turbine Optimization by Blade Element Momentum Method and Particle Swarm Optimization Technique," *Journal of Engineering,* vol. 2025, no. 1, 2025.

[51] W. Z. Stepniewski and C. N. Keys, "Momentum Theory," in *Rotary-Wing Aerodynamics*, vol. I, New York, NY: Dover Publications, Inc., 1984, pp. 44-90.

[52] E. Limacher, "Samara-Seed Aerodynamics," Calgary, Alberta, 2015.

[53] I. Lee, "Numerical study of a freely-falling maple seed," 2016.

[54] W. Z. Stepniewski and C. N. Keys, "Blade Element Theory," in *Rotary-Wing Aerodynamics*, 1st Edition ed., vol. I, New York, NY: Dover Publications, Inc., 1984, pp. 91-140.

[55] S. Liu, P. Niu, Y. Li, C. Jiao, M. Li, Y. Yang, S. Wang and T. J. Lu, "Maple-seed-inspired rotochute," *Physics of Fluids ,* vol. 38, no. 3, 2026.

[56] S. K. H. Win, L. S. T. Win, D. Sufiyan, G. S. Soh and S. Foong, "Dynamics and Control of a Collaborative and Separating Descent of Samara Autorotating Wings," *IEEE Robotics and Automation Letters,* vol. 4, no. 3, p. 3067–3074, 2019.

[57] S. K. H. Win, L. S. T. Win, D. Sufiyan, G. S. Soh and S. Foong, "Concurrent Optimization of Mechanical Design and Control for Flapless Samara-Inspired Autorotating Aerial Robot," in *IEEE/ASME International Conference on Advanced Intelligent Mechatronics*, Boston, MA, 2020.

[58] A. Rosen and D. Seter, "Vertical Autorotation of a Single-Winged Samara," *Journal of Applied Mechanics,* vol. 58, no. 4, December 1991.

[59] D. Seter and A. Rosen, "Study of the vertical autorotation of a single-winged Samara," *Biological Reviews of the Cambridge Philosophical Society,* vol. 67, no. 2, p. 175–197, 1992.

[60] D. Seter and A. Rosen, "Stability of the Vertical Autorotation of a Single-Winged Samara," *Journal of Applied Mechanics,* vol. 59, no. 4, pp. 1000-1008, 1992.

[61] A. Azuma and K. Yasuda, "Flight Performance of Rotary Seeds," *Journal of Theoretical Biology,* vol. 138, no. 1, p. 23–53, 1989.

[62] B. K. Jung and D. Rezgui, "Sectional Leading Edge Vortex Lift and Drag Coefficients of Autorotating Samaras," *Aerospace,* vol. 10, no. 5, 2023.

[63] H. Li, C. Cai, L. Jia and Y. Liu, "Aerodynamics of autorotating samaras in Ventilago leiocarpa," *Physics of Fluids,* vol. 38, no. 2, 2026.

[64] D. Lentink, W. B. Dickson, J. L. van Leeuwen and M. H. Dickinson, "Leading-Edge Vortices Elevate Lift of Autorotating Plant Seeds," *Science (American Association for the Advancement of Science),* vol. 324, no. 5933, p. 1438–1440, 2009.

[65] M. E. Çalışkan, F. Kaya, M. U. Sabırlı and I. Karagoz, "Design of a biomimetic wing from maple samara and investigation of the aerodynamic performance," *Physics of Fluids,* vol. 35, no. 9, 2023.

[66] W. Z. Stepniewski and C. N. Keys, "Vortex Theory," in *Rotary-Wing Aerodynamics*, New York, Dover Publications, Inc., 1984, pp. 141-232.

[67] J. R. Holden, "Experimental Testing and Computational Fluid Dynamics Simulation of Maple Seeds and Performance Analysis as a Wind Turbine," Cincinnati, OH, 2016.

[68] A. Lolli, G. Corsi, B. Mazzolai and A. De Simone, "Aerodynamic performance of autorotating seeds: scaling by size," *Bioinspiration & Biomimetics,* 2026.

[69] G. Arranz, M. Moriche, M. Uhlmann, O. Flores and M. García-Villalba, "Kinematics and dynamics of the auto-rotation of a model winged seed," *Bioinspiration & Biomimetics,* vol. 13, no. 3, 2018.

[70] G. Arranz, M. Moriche, M. Uhlmann, O. Flores and M. García-Villalba, "The Influence of the Reynolds Number on the Auto-Rotation of Samaras," in *Direct and Large-Eddy Simulation*, vol. 25, M. V. Salvetti, V. Armenio, H. Kuerten, J. öhlich and B. J. Geurts, Eds., Springer International Publishing AG, 2019, pp. 411-416.

[71] C. Liu, T. Wang, J. Li and X. Shao, " Effects of wing loading on the aerodynamic characteristics of autorotating maple seeds," *Physics of Fluids,* vol. 36, no. 3, 2024.

[72] P. Shukla, R. Mishra, U. A. Sardar and B. Mohapatra, "Satellite Design for CANSAT with Autorotatig payloads," in *2022 4th International Conference on Advances in Computing, Communication Control and Networking*, 2022.

[73] J. Zheng, K. A. Neusypin and M. S. Selezneva, " Auto-Landing of Moving-Mass Actuated Unmanned Aerial Vehicles Based on Linear Active Disturbance Rejection Control," *Drones (Basel),* vol. 7, no. 8, 2023.

[74] S. A. Erturk and A. Dogan, " Trim Analyses of Mass-Actuated Airplane in Cruise and Steady-State Turn," *Journal of Aircraft,* vol. 54, no. 4, p. 1587–1594, 2017.

[75] M. Idrissi, M. Salami and F. Annaz, " Modelling, simulation and control of a novel structure varying quadrotor," *Aerospace Science and Technology,* vol. 119, 2021.

[76] L. Chen, G. Zhou, X. J. Yan and D. P. Duan, "Composite Control Strategy of Stratospheric Airships with Moving Masses," *Journal of Aircraft,* vol. 49, no. 3, p. 794–801, 2012.

[77] Q. Du, Y. Hu, W. Jing and C. Gao, "Dynamics and Moving-Mass Parameter Design of Single Moving-Mass Roll and Trim Control Hypersonic Vehicle," *IEEE Transactions on Aerospace and Electronic Systems,* vol. 61, no. 2, p. 1298–1312, 2025.

[78] C. Gao, P. Wei and W. Jing, "Dynamics modeling and control system design for the reentry warhead controlled by single moving mass," in *013 10th IEEE International Conference on Control and Automation (ICCA)*, Hangzhou, China, 2013.

[79] R. D. Robinett, III, B. R. Sturgis and S. A. Kerr, "Moving mass trim control for aerospace vehicles," *Journal of Guidance, Control, and Dynamics,* vol. 19, no. 5, p. 1064–1070, 1996.

[80] Q. Zheng, Z. Zhou and A. Swierniak, "Stability of Moving Mass Control Spinning Missiles with Angular Rate Loop," *Mathematical Problems in Engineering,* vol. 2019, no. 2019, pp. 1-10, 2019.

[81] D. T. Greenwood, "Introduction to Particle Dynamics," in *Advanced Dynamics*, Cambridge, Cambridge University Press., 2003, pp. 1-72.

[82] J. D. Anderson, Jr., Fundamentals of Aerodynamics, 6th Edition ed., Boston, MA: McGraw-Hill Higher Education, 2017.

[83] A.-A.-M. Gheorghiu, I. Bunescu, M.-V. Hothazie, M.-F. Negoita and M.-V. Pricop, "Estimation of rotor aerodynamics using blade element theory," *INCAS Bulletin,* vol. 18, no. 1, pp. 21-35, 2026.

[84] S. Gudmundsson, "The Anatomy of the Propeller," in *General Aviation Aircraft Design*, Boston, MA: Butterworth-Heinemann, 2014, pp. 581-659.

[85] S. Tong, Z. Shi, T. Yun and Y. Dong, "Longitudinal flight dynamics modeling and a flight stability analysis of a monocopter," *AIP Advances,* vol. 12, no. 11, 2022.

[86] J. Walker, "The Amateur Scientist: The aerodynamics of the samara: winged seed of the maple, the ash and other trees," *Scientific American,* vol. 245, no. 4, 1981.

[87] D. T. Greenwood, "Kinematics and dynamics of a rigid body," in *Advanced Dynamics*, Cambridge, Cambridge University Press, 2003, pp. 140-216.

Appendix A. Rotation Matrix Calculations

Using a *Z-Y-X* sequence of rotations defined in Chapter 3, the following calculation is used to derive the rotation matrix that relates $\mathcal{F}_i$ to $\mathcal{F}_b$.

$$\{\hat{\boldsymbol{b}}\} = \boldsymbol{R}\{\hat{\boldsymbol{e}}\} \tag{A-1}$$

where

$$\boldsymbol{R} = \boldsymbol{R}_X(\psi)\boldsymbol{R}_Y(\vartheta)\boldsymbol{R}_Z(\phi) \tag{A-2}$$

Defining the individual rotations as follows,

$$\boldsymbol{R}_X(\psi) = \begin{bmatrix} 1 & 0 & 0 \\ 0 & \cos\psi & \sin\psi \\ 0 & -\sin\psi & \cos\psi \end{bmatrix} \tag{A-3}$$

$$\boldsymbol{R}_Y(\vartheta) = \begin{bmatrix} \cos\vartheta & 0 & -\sin\vartheta \\ 0 & 1 & 0 \\ \sin\vartheta & 0 & \cos\vartheta \end{bmatrix} = \begin{bmatrix} \cos(-\theta) & 0 & -\sin(-\theta) \\ 0 & 1 & 0 \\ \sin(-\theta) & 0 & \cos(-\theta) \end{bmatrix} = \begin{bmatrix} \cos\theta & 0 & \sin\theta \\ 0 & 1 & 0 \\ -\sin\theta & 0 & \cos\theta \end{bmatrix} \tag{A-4}$$

$$\boldsymbol{R}_Z(\phi) = \begin{bmatrix} \cos\phi & \sin\phi & 0 \\ -\sin\phi & \cos\phi & 0 \\ 0 & 0 & 1 \end{bmatrix} \tag{A-5}$$

Substituting into the initial equation,

$$\boldsymbol{R} = \begin{bmatrix} 1 & 0 & 0 \\ 0 & \cos\psi & \sin\psi \\ 0 & -\sin\psi & \cos\psi \end{bmatrix} \begin{bmatrix} \cos\theta & 0 & \sin\theta \\ 0 & 1 & 0 \\ -\sin\theta & 0 & \cos\theta \end{bmatrix} \begin{bmatrix} \cos\phi & \sin\phi & 0 \\ -\sin\phi & \cos\phi & 0 \\ 0 & 0 & 1 \end{bmatrix} \tag{A-6}$$

which simplifies to the following,

$$\boldsymbol{R} = \begin{bmatrix} \cos\phi\cos\theta & \sin\phi\cos\theta & \sin\theta \\ -\sin\phi\cos\psi - \cos\phi\sin\theta\sin\psi & \cos\phi\cos\psi - \sin\phi\sin\theta\sin\psi & \cos\theta\sin\psi \\ \sin\phi\sin\psi - \cos\phi\sin\theta\cos\psi & -\cos\phi\sin\psi - \sin\phi\sin\theta\cos\psi & \cos\theta\cos\psi \end{bmatrix} \tag{A-7}$$

Since the inverse of a rotation matrix is equal to its transpose, we can easily find the following relationship. While McConnell and Das did not include a rotation matrix in their papers, the following relationship yields consistent results with the translational equation of motion used in [1] [2] [3].

$$\boxed{\begin{bmatrix}\hat{e}_x\\ \hat{e}_y\\ \hat{e}_z\end{bmatrix}=\begin{bmatrix}\cos\phi\cos\theta & -\sin\phi\cos\psi-\cos\phi\sin\theta\sin\psi & \sin\phi\sin\psi-\cos\phi\sin\theta\cos\psi\\ \sin\phi\cos\theta & \cos\phi\cos\psi-\sin\phi\sin\theta\sin\psi & -\cos\phi\sin\psi-\sin\phi\sin\theta\cos\psi\\ \sin\theta & \cos\theta\sin\psi & \cos\theta\cos\psi\end{bmatrix}\begin{bmatrix}\hat{b}_x\\ \hat{b}_y\\ \hat{b}_z\end{bmatrix}} \tag{A-8}$$

Appendix B. Derivation of Angular Velocity

Using the Euler transformation defined in Chapter 3, the first rotation about the Z_i-axis with angular magnitude of ϕ can be expressed by the following,

$$\boldsymbol{\omega}_{i}^{i'i} = [0 \quad 0 \quad \dot{\phi}]^T \quad \boldsymbol{\omega}_{i'}^{i'i} = [0 \quad 0 \quad \dot{\phi}]^T \tag{B-1}$$

where $\boldsymbol{\omega}_{i}^{i'i} \equiv \boldsymbol{\omega}_{i'}^{i'i}$ is the angular velocity of the rotation between $\mathcal{F}_i$ and $\mathcal{F}_{i'}$ as seen from these reference frames, respectively. The second rotation about the $Y_{i'}$-axis with angular magnitude of ϑ can be expressed by the following,

$$\boldsymbol{\omega}_{i'}^{i''i'} = [0 \quad \dot{\vartheta} \quad 0]^T \qquad \boldsymbol{\omega}_{i''}^{i''i'} = [0 \quad \dot{\vartheta} \quad 0]^T \tag{B-2}$$

where $\boldsymbol{\omega}_{i'}^{i''i'} \equiv \boldsymbol{\omega}_{i''}^{i''i'}$ is the angular velocity of the rotation between $\mathcal{F}_{i'}$ and $\mathcal{F}_{i''}$ as seen from these reference frames, respectively. The coning angle relationship, $\vartheta = -\theta$, as described in Chapter 3, yields the following time derivative: $\dot{\vartheta} = -\dot{\theta}$. Therefore, the angular velocity can be modified to the following,

$$\boldsymbol{\omega}_{i'}^{i''i'} = [0 \quad -\dot{\theta} \quad 0]^T \qquad \boldsymbol{\omega}_{i''}^{i''i'} = [0 \quad -\dot{\theta} \quad 0]^T \tag{B-3}$$

The third and final rotation about the $X_{i''}$-axis with angular magnitude of ψ can be expressed by the following,

$$\boldsymbol{\omega}_{i''}^{bi''} = [\dot{\psi} \quad 0 \quad 0]^T \qquad \boldsymbol{\omega}_{b}^{bi''} = [\dot{\psi} \quad 0 \quad 0]^T \tag{B-4}$$

where $\boldsymbol{\omega}_{i''}^{bi''} \equiv \boldsymbol{\omega}_{b}^{bi''}$ is the angular velocity of the rotation between $\mathcal{F}_{i''}$ and $\mathcal{F}_b$ as seen from these reference frames, respectively.

The angular velocity vectors representing these three rotations can be added together to find the total angular velocity of the fixed body frame with respect to the inertial reference frame,

$$\boldsymbol{\omega}^{bi} = \boldsymbol{\omega}^{bi''} + \boldsymbol{\omega}^{i''i'} + \boldsymbol{\omega}^{i'i} \tag{B-5}$$

To add these vectors together, they must be expressed in the same reference frame. Using the following rotation matrices all the vectors can be transformed into $\mathcal{F}_b$, which is the reference frame of choice,

$$\boldsymbol{\omega}^{bi''} = \boldsymbol{\omega}_b^{bi''} = \begin{bmatrix} \dot{\psi} \\ 0 \\ 0 \end{bmatrix} \tag{B-6}$$

$$\boldsymbol{\omega}^{i''i'} = \boldsymbol{R}_{bi''}(\psi)\boldsymbol{\omega}_{i''}^{i''i'} = \begin{bmatrix} 1 & 0 & 0 \\ 0 & \cos\psi & \sin\psi \\ 0 & -\sin\psi & \cos\psi \end{bmatrix} \begin{bmatrix} 0 \\ -\dot{\theta} \\ 0 \end{bmatrix} = \begin{bmatrix} 0 \\ -\dot{\theta}\cos\psi \\ \dot{\theta}\sin\psi \end{bmatrix} \tag{B-7}$$

$$\begin{aligned} \boldsymbol{\omega}^{i'i} = \boldsymbol{R}_{bi''}(\psi)\boldsymbol{R}_{i''i'}(\theta)\boldsymbol{\omega}_{i'}^{i'i} &= \begin{bmatrix} 1 & 0 & 0 \\ 0 & \cos\psi & \sin\psi \\ 0 & -\sin\psi & \cos\psi \end{bmatrix} \begin{bmatrix} \cos\theta & 0 & \sin\theta \\ 0 & 1 & 0 \\ -\sin\theta & 0 & \cos\theta \end{bmatrix} \begin{bmatrix} 0 \\ 0 \\ \dot{\phi} \end{bmatrix} \\ &= \begin{bmatrix} \dot{\phi}\sin\theta \\ \dot{\phi}\cos\theta\sin\psi \\ \dot{\phi}\cos\theta\cos\psi \end{bmatrix} \end{aligned} \tag{B-8}$$

Substituting these fixed body frame angular velocity terms back into the absolute angular velocity equation,

$$\boxed{\boldsymbol{\omega}^{bi} = \boldsymbol{\omega}_b^{bi} = \begin{bmatrix} \dot{\psi} \\ 0 \\ 0 \end{bmatrix} + \begin{bmatrix} 0 \\ -\dot{\theta}\cos\psi \\ \dot{\theta}\sin\psi \end{bmatrix} + \begin{bmatrix} \dot{\phi}\sin\theta \\ \dot{\phi}\cos\theta\sin\psi \\ \dot{\phi}\cos\theta\cos\psi \end{bmatrix} = \begin{bmatrix} \dot{\psi} + \dot{\phi}\sin\theta \\ \dot{\phi}\cos\theta\sin\psi - \dot{\theta}\cos\psi \\ \dot{\phi}\cos\theta\cos\psi + \dot{\theta}\sin\psi \end{bmatrix}} \tag{B-9}$$

Now, finding the first order time derivative of $\boldsymbol{\omega}^{bi}$,

$$\boxed{\dot{\boldsymbol{\omega}}^{bi} = \begin{bmatrix} \ddot{\psi} + \ddot{\phi}\sin\theta + \dot{\phi}\dot{\theta}\cos\theta \\ \ddot{\phi}\cos\theta\sin\psi - \ddot{\theta}\cos\psi - \dot{\phi}\dot{\theta}\sin\theta\sin\psi + \dot{\phi}\dot{\psi}\cos\theta\cos\psi + \dot{\theta}\dot{\psi}\sin\psi \\ \ddot{\phi}\cos\theta\cos\psi + \ddot{\theta}\sin\psi - \dot{\phi}\dot{\theta}\sin\theta\cos\psi - \dot{\phi}\dot{\psi}\cos\theta\sin\psi + \dot{\theta}\dot{\psi}\cos\psi \end{bmatrix}} \tag{B-10}$$

Appendix C. Derivation of Moments of Inertia

Assuming the seed, wing, and moving mass all have constant density, the respective rigid body centers of mass would be located at their respective physical centers. The location of the center of mass of the composite model with respect to the origin can then be found to be the following,

$$\boldsymbol{\rho}_{comp}^{QC} = \frac{m_s \begin{bmatrix} 0 \\ 0 \\ 0 \end{bmatrix} + m_w \begin{bmatrix} (l+a)/2 \\ 0 \\ 0 \end{bmatrix} + m_m \begin{bmatrix} s(t) \\ 0 \\ 0 \end{bmatrix}}{m_{comp}} = \frac{1}{m_{comp}} \begin{bmatrix} m_w \dfrac{(l+a)}{2} + m_m(s(t)) \\ 0 \\ 0 \end{bmatrix} \tag{C-1}$$

where m represents mass with the subscripts consistent with what has previously been defined for the different geometric components of the model. Anything with the subscript "$comp$" designates the composite model, which includes the seed, wing, and moving mass. The superscripts used throughout this section are used to help determine the direction of the vectors that they reference, where Q denotes the fixed body origin, C denotes the referenced center of mass, and QC denotes that the vector is traveling from the fixed body origin to the center of mass. Any use of the superscript T denotes a vector transpose. For each rigid body, the inertial matrices in the respective principle centroidal reference frames can be found below,

$$\boldsymbol{I}_s^C = \boldsymbol{I}_s^Q = \begin{bmatrix} 0 & 0 & 0 \\ 0 & \dfrac{m_s l^2}{12} & 0 \\ 0 & 0 & \dfrac{m_s l^2}{12} \end{bmatrix} \tag{C-2}$$

$$\boldsymbol{I}_w^C = \begin{bmatrix} \dfrac{m_w b^2}{12} & 0 & 0 \\ 0 & \dfrac{m_w a^2}{12} & 0 \\ 0 & 0 & \dfrac{m_w(a^2+b^2)}{12} \end{bmatrix} \tag{C-3}$$

where the moment can be translated to the origin using the parallel axis theorem,

$$\boldsymbol{I}_w^Q = \boldsymbol{I}_w^C + m_w\left[\boldsymbol{\rho}_w^{QCT} \boldsymbol{\rho}_w^{QC} \mathbf{1} - \boldsymbol{\rho}_w^{QC} \boldsymbol{\rho}_w^{QCT}\right] \tag{C-4}$$

$$\boldsymbol{I}_w^Q = \boldsymbol{I}_w^C + m_w\left(\begin{bmatrix}\left(\frac{l+a}{2}\right)^2 & 0 & 0\\ 0 & \left(\frac{l+a}{2}\right)^2 & 0\\ 0 & 0 & \left(\frac{l+a}{2}\right)^2\end{bmatrix} - \begin{bmatrix}\left(\frac{l+a}{2}\right)^2 & 0 & 0\\ 0 & 0 & 0\\ 0 & 0 & 0\end{bmatrix}\right) \tag{C-5}$$

$$\boldsymbol{I}_w^Q = \begin{bmatrix}\frac{m_w b^2}{12} & 0 & 0\\ 0 & m_w\left(\frac{a^2}{12} + \left(\frac{l+a}{2}\right)^2\right) & 0\\ 0 & 0 & m_w\left(\frac{a^2+b^2}{12} + \left(\frac{l+a}{2}\right)^2\right)\end{bmatrix} \tag{C-6}$$

The moments of inertia of a single mass relative to the origin can be defined by the general inertia dyadic of a rigid body [87],

$$\boldsymbol{I}_m^Q = \int [(\boldsymbol{\rho}_m \cdot \boldsymbol{\rho}_m)\mathbf{1} - \boldsymbol{\rho}_m^T \boldsymbol{\rho}_m] dm \tag{C-7}$$

where

$$\boldsymbol{\rho}_m = \begin{bmatrix} s(t) \\ 0 \\ 0 \end{bmatrix} \tag{C-8}$$

which results in the following,

$$\boldsymbol{I}_m^Q = \begin{bmatrix} 0 & 0 & 0 \\ 0 & m_m[s(t)]^2 & 0 \\ 0 & 0 & m_m[s(t)]^2 \end{bmatrix} \tag{C-9}$$

To find the composite moments of inertia, the three individual moments about the origin are added together,

$$\boldsymbol{I}_{comp}^Q = \boldsymbol{I}_s^Q + \boldsymbol{I}_w^Q + \boldsymbol{I}_m^Q \tag{C-10}$$

which results in the following,

$$\boldsymbol{I}_{comp}^{Q} = \text{diag}\begin{bmatrix} \dfrac{m_w b^2}{12} \\ \dfrac{m_s l^2}{12} + m_w\left(\dfrac{a^2}{12} + \left(\dfrac{l+a}{2}\right)^2\right) + m_m[s(t)]^2 \\ \dfrac{m_s l^2}{12} + m_w\left(\dfrac{a^2+b^2}{12} + \left(\dfrac{l+a}{2}\right)^2\right) + m_m[s(t)]^2 \end{bmatrix} \tag{C-11}$$

Now using the parallel axis theorem, the moments about the system center of mass can be found to be the following [87],

$$\boldsymbol{I}_{comp}^{C} = \boldsymbol{I}_{comp}^{Q} + m_{comp}\left[\boldsymbol{\rho}_{comp}^{QCT}\boldsymbol{\rho}_{comp}^{QC}\mathbf{1} - \boldsymbol{\rho}_{comp}^{QC}\boldsymbol{\rho}_{comp}^{QCT}\right] \tag{C-12}$$

where

$$m_{comp}\left[\boldsymbol{\rho}_{comp}^{QCT}\boldsymbol{\rho}_{comp}^{QC}\mathbf{1} - \boldsymbol{\rho}_{comp}^{QC}\boldsymbol{\rho}_{comp}^{QCT}\right] = \text{diag}\begin{bmatrix} 0 \\ \dfrac{1}{m_{comp}}\left(\dfrac{m_w(l+a)}{2} + m_m s(t)\right)^2 \\ \dfrac{1}{m_{comp}}\left(\dfrac{m_w(l+a)}{2} + m_m s(t)\right)^2 \end{bmatrix} \tag{C-13}$$

which leads to the following moments of inertia,

$$\boxed{\begin{gathered} I_{xx} = \frac{m_w b^2}{12} \\ I_{yy} = \frac{m_s l^2}{12} + m_w\left(\frac{a^2}{12} + \left(\frac{l+a}{2}\right)^2\right) + m_m[s(t)]^2 + \frac{1}{m_{comp}}\left(\frac{m_w(l+a)}{2} + m_m s(t)\right)^2 \\ I_{zz} = \frac{m_s l^2}{12} + m_w\left(\frac{a^2+b^2}{12} + \left(\frac{l+a}{2}\right)^2\right) + m_m[s(t)]^2 + \frac{1}{m_{comp}}\left(\frac{m_w(l+a)}{2} + m_m s(t)\right) \end{gathered}} \tag{C-14}$$

First order time derivatives of moments of inertia,

$$\boxed{\begin{gathered} \dot{I}_{xx} = 0 \\ \dot{I}_{yy} = 2m_m s(t)s'(t) + \frac{2m_m}{m_{comp}}\left(\frac{m_w(l+a)}{2} + m_m s(t)\right)s'(t) \\ \dot{I}_{zz} = 2m_m s(t)s'(t) + \frac{2m_m}{m_{comp}}\left(\frac{m_w(l+a)}{2} + m_m s(t)\right)s'(t) \end{gathered}} \tag{C-15}$$

Appendix D. Derivation of Rotational Equations of Motion

Appendix D derives the rotational equations of motion used in this report. Since the dynamic model used in this analysis is exploring a time-varying mass distribution of the samara, special care must be given to the derivation of the rotational equations of motion. Because of the changing mass distribution, the center of mass cannot be used as the point of reference of the fixed body reference frame. Alternatively, to establish time-varying equations of motion with an arbitrary fixed body reference point, more generalized equations must be developed from particle dynamics. To begin, Figure D-1 is based on a figure in [87] and depicts a generalized rigid body. This figure is used to graphically define the terms used throughout this derivation.

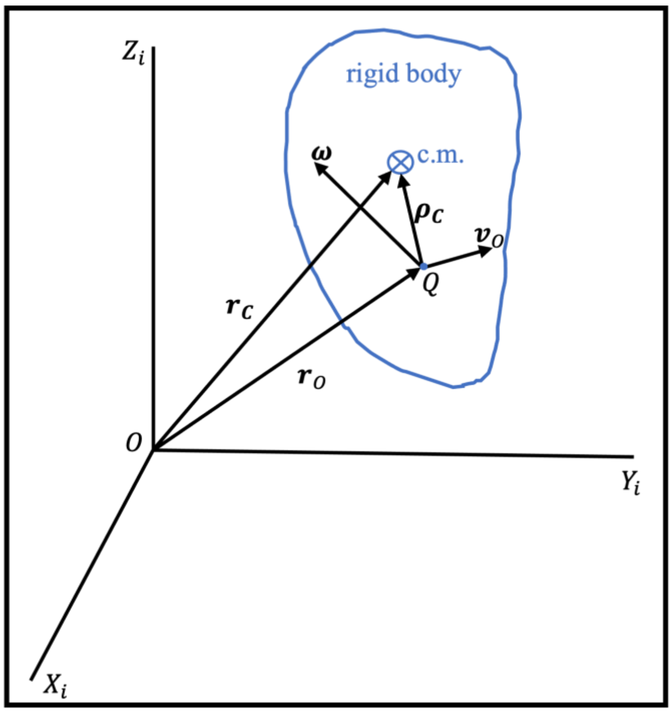

Figure D-1. General diagram relating an arbitrary rigid body to the inertial reference frame [87].

For reference point Q which is fixed to in the body but not the center of mass or a fixed point in space [81],

$$\dot{\boldsymbol{H}}_Q = \boldsymbol{M}_C + \boldsymbol{\rho}^{QC} \times (\boldsymbol{F} - m(\dot{\boldsymbol{v}}_O)_r) \tag{D-1}$$

where $\dot{\boldsymbol{H}}_Q$ is the time derivative of the angular momentum of the samara, $\boldsymbol{M}_C$ is the applied moment about the center of mass, $\boldsymbol{\rho}_C$ is the position vector from the reference point Q to the center of mass C, $\boldsymbol{F}$ is the external force acting on the samara, and $(\dot{\boldsymbol{v}}_O)_r$ is the absolute acceleration of the samara relative to a rotating fixed body reference frame.

Introducing the definition of the angular momentum $\boldsymbol{H}$ at reference point Q [87]:

$$\boldsymbol{H}_Q = \boldsymbol{I}_Q \cdot \boldsymbol{\omega} \tag{D-2}$$

where $\boldsymbol{I}_Q$ is the moment of inertia of the rigid body about an arbitrary point Q. Using the product rule to find the time derivative of $\boldsymbol{H}_Q$,

$$\dot{\boldsymbol{H}}_Q = \boldsymbol{I}_Q \cdot \dot{\boldsymbol{\omega}} + \dot{\boldsymbol{I}}_Q \cdot \boldsymbol{\omega} \tag{D-3}$$

This derivative differs from [87], which assumed the moments of inertia to be composed of constant scalar quantities and would cause the second term to equal zero. Since this derivation is considering a time-varying inertial tensor, the second term must be included.

Combining this derivation with the general equation of motion provided at the beginning of this section,

$$\boldsymbol{M}_C + \boldsymbol{\rho}_C \times (\boldsymbol{F} - m(\dot{\boldsymbol{v}}_O)_r) = \boldsymbol{I}_Q \cdot \dot{\boldsymbol{\omega}} + \dot{\boldsymbol{I}}_Q \cdot \boldsymbol{\omega} \tag{D-4}$$

Introducing an equation that defines the absolute acceleration at point P, $\dot{\boldsymbol{v}}_P$ and the acceleration at the center of mass [81],

$$(\dot{\boldsymbol{v}}_O)_r = \dot{\boldsymbol{v}}_O + \underbrace{\dot{\boldsymbol{\omega}} \times \boldsymbol{\rho}_C}_{\substack{\text{tangential} \\ \text{acceleration}}} + \underbrace{\boldsymbol{\omega} \times (\boldsymbol{\omega} \times \boldsymbol{\rho}_C)}_{\substack{\text{centripetal} \\ \text{acceleration}}} + (\ddot{\boldsymbol{\rho}}_C)_r + \underbrace{2\boldsymbol{\omega} \times (\dot{\boldsymbol{\rho}}_C)_r}_{\substack{\text{Coriolis acceleration due to a} \\ \text{velocity relative to rotation frame}}} \tag{D-5}$$

where $\dot{\boldsymbol{v}}_O$ is the inertial acceleration of the samara fixed body origin and $(\ddot{\boldsymbol{\rho}}_C)_r$ is the acceleration of the center of mass relative to the fixed body reference frame.

Introducing the parallel axis theorem, a relationship between the moment of inertia about Q and the moment of inertia about the center of mass can be defined [87],

$$\boldsymbol{I}_Q = \boldsymbol{I}_C + m((\boldsymbol{\rho}_C^T)^{\circ 2}\mathbf{1} - \boldsymbol{\rho}_C\boldsymbol{\rho}_C^T) \tag{D-6}$$

where $(\boldsymbol{\rho}_C^T)^{\circ 2}$ is a Hadamard power, denotes an element-wise squared vector, and is equivalent to the vector magnitude squared. The Hadamard notation varies from what is used in [87] and was adopted for this use since it simplifies the derivative found in the following equation,

$$\dot{\boldsymbol{I}}_Q = \dot{\boldsymbol{I}}_C + m\big(2(\boldsymbol{\rho}_C^T \odot \dot{\boldsymbol{\rho}}_C^T)\mathbf{1} - (\boldsymbol{\rho}_C\dot{\boldsymbol{\rho}}_C^T + \dot{\boldsymbol{\rho}}_C\boldsymbol{\rho}_C^T)\big) \tag{D-7}$$

where $(\boldsymbol{\rho}_C^T \odot \dot{\boldsymbol{\rho}}_C^T)$ denotes the Hadamard product, an element-wise product of the two vectors. Introducing the general definition of $\boldsymbol{I}_C$,

$$\boldsymbol{I}_C = \sum_{i=1}^{3}\sum_{j=1}^{3} I_{C_{ij}} \hat{b}_i \hat{b}_j \tag{D-8}$$

where $\hat{b}_i$ and $\hat{b}_j$ represent unit dyads that are mutually orthogonal and rotate with the body. The term $I_{C_{ij}}$ represent the 9 terms of the inertia dyadic about the center of mass.

Using product rule, the time derivative of $\boldsymbol{I}_C$ can be defined as follows [87],

$$\dot{\boldsymbol{I}}_C = \sum_{i=1}^{3}\sum_{j=1}^{3} \left(\dot{I}_{C_{ij}} \hat{b}_i \hat{b}_j + I_{C_{ij}} \dot{\hat{b}}_i \hat{b}_j + I_{C_{ij}} \hat{b}_i \dot{\hat{b}}_j \right) \tag{D-9}$$

Leveraging mathematical properties presented in [87], the second and third terms of the derivative can be rewritten as follows using dyadic operations,

$$\dot{\boldsymbol{I}}_C = \sum_{i=1}^{3}\sum_{j=1}^{3} \left(\dot{I}_{C_{ij}} \hat{b}_i \hat{b}_j \right) + \boldsymbol{\omega} \times \boldsymbol{I}_C - \boldsymbol{I}_C \times \boldsymbol{\omega} \tag{D-10}$$

Substituting Equation (D-10) back into Equation (D-7),

$$\dot{\boldsymbol{I}}_Q = \sum_{i=1}^{3}\sum_{j=1}^{3} \left(\dot{I}_{C_{ij}} \hat{b}_i \hat{b}_j \right) + \boldsymbol{\omega} \times \boldsymbol{I}_C - \boldsymbol{I}_C \times \boldsymbol{\omega} + m\big(2(\boldsymbol{\rho}_C^T \odot \dot{\boldsymbol{\rho}}_C^T)\boldsymbol{1} - (\boldsymbol{\rho}_C \dot{\boldsymbol{\rho}}_C^T + \dot{\boldsymbol{\rho}}_C \boldsymbol{\rho}_C^T)\big) \tag{D-11}$$

Now, substituting Equations (D-5), (D-6), and (D-11) into Equation (D-4),

$$\begin{aligned} \boldsymbol{M}_c + \boldsymbol{\rho}_{\boldsymbol{C}} \times \big(\boldsymbol{F} - m(\dot{\boldsymbol{v}}_O + \dot{\boldsymbol{\omega}} \times \boldsymbol{\rho}_C + \boldsymbol{\omega} \times (\boldsymbol{\omega} \times \boldsymbol{\rho}_C) + (\ddot{\boldsymbol{\rho}}_C)_r + 2\boldsymbol{\omega} \times (\dot{\boldsymbol{\rho}}_C)_r)\big) \\ = \big(\boldsymbol{I}_C + m((\boldsymbol{\rho}_C^T)^{\circ 2}\boldsymbol{1} - \boldsymbol{\rho}_C \boldsymbol{\rho}_C^T)\big) \cdot \dot{\boldsymbol{\omega}} \\ + \left(\sum_{i=1}^{3}\sum_{j=1}^{3} \left(\dot{I}_{C_{ij}} \hat{b}_i \hat{b}_j \right) + \boldsymbol{\omega} \times \boldsymbol{I}_C - \boldsymbol{I}_C \times \boldsymbol{\omega} \right. \\ \left. + m\big(2(\boldsymbol{\rho}_C^T \odot \dot{\boldsymbol{\rho}}_C^T)\boldsymbol{1} - (\boldsymbol{\rho}_C \dot{\boldsymbol{\rho}}_C^T + \dot{\boldsymbol{\rho}}_C \boldsymbol{\rho}_C^T)\big) \right) \cdot \boldsymbol{\omega} \end{aligned} \tag{D-12}$$

Expanding the equation yields the following,

$$\begin{aligned}\boldsymbol{M}_C + \boldsymbol{\rho_C} \times \boldsymbol{F} - \boldsymbol{\rho_C} \times m\dot{\boldsymbol{v}}_O - \boldsymbol{\rho_C} \times m(\dot{\boldsymbol{\omega}} \times \boldsymbol{\rho}_C) - \boldsymbol{\rho_C} \times m\big(\boldsymbol{\omega} \times (\boldsymbol{\omega} \times \boldsymbol{\rho}_C)\big) \\ - \boldsymbol{\rho_C} \times m(\ddot{\boldsymbol{\rho}}_C)_r - \boldsymbol{\rho_C} \times m(2\boldsymbol{\omega} \times (\dot{\boldsymbol{\rho}}_C)_r) \\ = \boldsymbol{I}_C \cdot \dot{\boldsymbol{\omega}} + m((\boldsymbol{\rho}_C^T)^{\circ 2}\mathbf{1} - \boldsymbol{\rho}_C\boldsymbol{\rho}_C^T) \cdot \dot{\boldsymbol{\omega}} + \sum_{i=1}^{3}\sum_{j=1}^{3}\left(\dot{I}_{C_{ij}} b_i b_j\right) \cdot \boldsymbol{\omega} + \boldsymbol{\omega} \times \boldsymbol{I}_C \\ \cdot \boldsymbol{\omega} - \boldsymbol{I}_C \times \boldsymbol{\omega} \cdot \boldsymbol{\omega} + m\big(2(\boldsymbol{\rho}_C^T \odot \dot{\boldsymbol{\rho}}_C^T)\mathbf{1} - (\boldsymbol{\rho}_C\dot{\boldsymbol{\rho}}_C^T + \dot{\boldsymbol{\rho}}_C\boldsymbol{\rho}_C^T)\big) \cdot \boldsymbol{\omega}\end{aligned} \tag{D-13}$$

Using Newton's second law, $\boldsymbol{F} = \boldsymbol{m}\dot{\boldsymbol{v}}_O$ and using the dyadic property, $(\boldsymbol{I} \times \boldsymbol{\omega}) \cdot \boldsymbol{\omega} = \mathbf{0}$ [87], the equation can be simplified to the following,

$$\begin{aligned}\boldsymbol{M}_C - \boldsymbol{\rho_C} \times m(\dot{\boldsymbol{\omega}} \times \boldsymbol{\rho}_C) - \boldsymbol{\rho_C} \times m\big(\boldsymbol{\omega} \times (\boldsymbol{\omega} \times \boldsymbol{\rho}_C)\big) - \boldsymbol{\rho_C} \times m(\ddot{\boldsymbol{\rho}}_C)_r \\ - \boldsymbol{\rho_C} \times m(2\boldsymbol{\omega} \times (\dot{\boldsymbol{\rho}}_C)_r) \\ = \boldsymbol{I}_C \cdot \dot{\boldsymbol{\omega}} + m((\boldsymbol{\rho}_C^T)^{\circ 2}\mathbf{1} - \boldsymbol{\rho}_C\boldsymbol{\rho}_C^T) \cdot \dot{\boldsymbol{\omega}} + \sum_{i=1}^{3}\sum_{j=1}^{3}\left(\dot{I}_{C_{ij}} b_i b_j\right) \cdot \boldsymbol{\omega} + \boldsymbol{\omega} \times \boldsymbol{I}_C \cdot \boldsymbol{\omega} \\ + m\big(2(\boldsymbol{\rho}_C^T \odot \dot{\boldsymbol{\rho}}_C^T)\mathbf{1} - (\boldsymbol{\rho}_C\dot{\boldsymbol{\rho}}_C^T + \dot{\boldsymbol{\rho}}_C\boldsymbol{\rho}_C^T)\big) \cdot \boldsymbol{\omega}\end{aligned} \tag{D-14}$$

Rearranging terms, where the bracketed terms are a result of using an arbitrary point of reference,

$$\begin{aligned}\boldsymbol{M}_C = \boldsymbol{I}_C \cdot \dot{\boldsymbol{\omega}} + \sum_{i=1}^{3}\sum_{j=1}^{3}\left(\dot{I}_{C_{ij}} b_i b_j\right) \cdot \boldsymbol{\omega} + \boldsymbol{\omega} \times \boldsymbol{I}_C \cdot \boldsymbol{\omega} \\ + \big[m((\boldsymbol{\rho}_C^T)^{\circ 2}\mathbf{1} - \boldsymbol{\rho}_C\boldsymbol{\rho}_C^T) \cdot \dot{\boldsymbol{\omega}} + m\big(2(\boldsymbol{\rho}_C^T \odot \dot{\boldsymbol{\rho}}_C^T)\mathbf{1} - (\boldsymbol{\rho}_C\dot{\boldsymbol{\rho}}_C^T + \dot{\boldsymbol{\rho}}_C\boldsymbol{\rho}_C^T)\big) \\ \cdot \boldsymbol{\omega} + \boldsymbol{\rho_C} \times m(\dot{\boldsymbol{\omega}} \times \boldsymbol{\rho}_C) + \boldsymbol{\rho_C} \times m\big(\boldsymbol{\omega} \times (\boldsymbol{\omega} \times \boldsymbol{\rho}_C)\big) + \boldsymbol{\rho_C} \times m(\ddot{\boldsymbol{\rho}}_C)_r \\ + \boldsymbol{\rho_C} \times m(2\boldsymbol{\omega} \times (\dot{\boldsymbol{\rho}}_C)_r)\big]\end{aligned} \tag{D-15}$$

Applying dyadic operations and vector operations to the terms of the equation,

a) $\boldsymbol{I}_C \cdot \dot{\boldsymbol{\omega}}$

$$\begin{bmatrix} I_{xx} & I_{xy} & I_{xz} \\ I_{xy} & I_{yy} & I_{yz} \\ I_{xz} & I_{yz} & I_{zz} \end{bmatrix} \cdot \begin{bmatrix} \dot{\omega}_x \\ \dot{\omega}_y \\ \dot{\omega}_z \end{bmatrix} = \begin{bmatrix} I_{xx}\dot{\omega}_x + I_{xy}\dot{\omega}_y + I_{xz}\dot{\omega}_z \\ I_{xy}\dot{\omega}_x + I_{yy}\dot{\omega}_y + I_{yz}\dot{\omega}_z \\ I_{xz}\dot{\omega}_x + I_{yz}\dot{\omega}_y + I_{zz}\dot{\omega}_z \end{bmatrix} \tag{D-16}$$

b) $\sum_{i=1}^{3}\sum_{j=1}^{3}\left(\dot{I}_{C_{ij}} b_i b_j\right) \cdot \boldsymbol{\omega}$

$$\begin{bmatrix} \dot{I}_{xx} & \dot{I}_{xy} & \dot{I}_{xz} \\ \dot{I}_{xy} & \dot{I}_{yy} & \dot{I}_{yz} \\ \dot{I}_{xz} & \dot{I}_{yz} & \dot{I}_{zz} \end{bmatrix} \cdot \begin{bmatrix} \omega_x \\ \omega_y \\ \omega_z \end{bmatrix} = \begin{bmatrix} \dot{I}_{xx}\omega_x + \dot{I}_{xy}\omega_y + \dot{I}_{xz}\omega_z \\ \dot{I}_{xy}\omega_x + \dot{I}_{yy}\omega_y + \dot{I}_{yz}\omega_z \\ \dot{I}_{xz}\omega_x + \dot{I}_{yz}\omega_y + \dot{I}_{zz}\omega_z \end{bmatrix} \tag{D-17}$$

c) $\boldsymbol{\omega} \times \boldsymbol{I}_C \cdot \boldsymbol{\omega}$

$$\begin{vmatrix} \hat{\imath} & \hat{\jmath} & \hat{k} \\ \omega_x & \omega_y & \omega_z \\ I_{xx} & I_{xy} & I_{xz} \end{vmatrix} = \begin{bmatrix} I_{xz}\omega_y - I_{xy}\omega_z \\ I_{xx}\omega_z - I_{xz}\omega_x \\ I_{xy}\omega_x - I_{xx}\omega_y \end{bmatrix}, \qquad \begin{vmatrix} \hat{\imath} & \hat{\jmath} & \hat{k} \\ \omega_x & \omega_y & \omega_z \\ I_{xy} & I_{yy} & I_{yz} \end{vmatrix} = \begin{bmatrix} I_{yz}\omega_y - I_{yy}\omega_z \\ I_{xy}\omega_z - I_{yz}\omega_x \\ I_{yy}\omega_x - I_{xy}\omega_y \end{bmatrix},$$
$$\begin{vmatrix} \hat{\imath} & \hat{\jmath} & \hat{k} \\ \omega_x & \omega_y & \omega_z \\ I_{xz} & I_{yz} & I_{zz} \end{vmatrix} = \begin{bmatrix} I_{zz}\omega_y - I_{yz}\omega_z \\ I_{xz}\omega_z - I_{zz}\omega_x \\ I_{yz}\omega_x - I_{xz}\omega_y \end{bmatrix} \tag{D-18}$$

Compiling the components from the resulting cross-product and evaluating the dot products,

$$\begin{gathered} \begin{bmatrix} I_{xz}\omega_y - I_{xy}\omega_z \\ I_{yz}\omega_y - I_{yy}\omega_z \\ I_{zz}\omega_y - I_{yz}\omega_z \end{bmatrix}_{\hat{\imath}} \cdot \begin{bmatrix} \omega_x \\ \omega_y \\ \omega_z \end{bmatrix} \\ \begin{bmatrix} I_{xx}\omega_z - I_{xz}\omega_x \\ I_{xy}\omega_z - I_{yz}\omega_x \\ I_{xz}\omega_z - I_{zz}\omega_x \end{bmatrix}_{\hat{\jmath}} \cdot \begin{bmatrix} \omega_x \\ \omega_y \\ \omega_z \end{bmatrix} \\ \begin{bmatrix} I_{xy}\omega_x - I_{xx}\omega_y \\ I_{yy}\omega_x - I_{xy}\omega_y \\ I_{yz}\omega_x - I_{xz}\omega_y \end{bmatrix}_{\hat{k}} \cdot \begin{bmatrix} \omega_x \\ \omega_y \\ \omega_z \end{bmatrix} \\ \Longrightarrow \begin{bmatrix} \omega_x(I_{xz}\omega_y - I_{xy}\omega_z) + \omega_y(I_{yz}\omega_y - I_{yy}\omega_z) + \omega_z(I_{zz}\omega_y - I_{yz}\omega_z) \\ \omega_x(I_{xx}\omega_z - I_{xz}\omega_x) + \omega_y(I_{xy}\omega_z - I_{yz}\omega_x) + \omega_z(I_{xz}\omega_z - I_{zz}\omega_x) \\ \omega_x(I_{xy}\omega_x - I_{xx}\omega_y) + \omega_y(I_{yy}\omega_x - I_{xy}\omega_y) + \omega_z(I_{yz}\omega_x - I_{xz}\omega_y) \end{bmatrix} \end{gathered} \tag{D-19}$$

d) $m((\boldsymbol{\rho}_C^T)^{\circ 2}\mathbf{1} - \boldsymbol{\rho}_C\boldsymbol{\rho}_C^T) \cdot \dot{\boldsymbol{\omega}}$

$$m\left(\begin{bmatrix} \rho_x^2 & 0 & 0 \\ 0 & \rho_y^2 & 0 \\ 0 & 0 & \rho_z^2 \end{bmatrix} - \begin{bmatrix} \rho_x^2 & \rho_x\rho_y & \rho_x\rho_z \\ \rho_x\rho_y & \rho_y^2 & \rho_y\rho_z \\ \rho_x\rho_z & \rho_y\rho_z & \rho_z^2 \end{bmatrix}\right) = \begin{bmatrix} 0 & -m\rho_x\rho_y & -m\rho_x\rho_z \\ -m\rho_x\rho_y & 0 & -m\rho_y\rho_z \\ -m\rho_x\rho_z & -m\rho_y\rho_z & 0 \end{bmatrix} \tag{D-20}$$

$$\begin{bmatrix} 0 & -m\rho_x\rho_y & -m\rho_x\rho_z \\ -m\rho_x\rho_y & 0 & -m\rho_y\rho_z \\ -m\rho_x\rho_z & -m\rho_y\rho_z & 0 \end{bmatrix} \cdot \begin{bmatrix} \dot{\omega}_x \\ \dot{\omega}_y \\ \dot{\omega}_z \end{bmatrix} = \begin{bmatrix} -m\rho_x\rho_y\dot{\omega}_y - m\rho_x\rho_z\dot{\omega}_z \\ -m\rho_x\rho_y\dot{\omega}_x - m\rho_y\rho_z\dot{\omega}_z \\ -m\rho_x\rho_z\dot{\omega}_x - m\rho_y\rho_z\dot{\omega}_y \end{bmatrix} \tag{D-21}$$

e) $m\big(2(\boldsymbol{\rho}_C^T \odot \dot{\boldsymbol{\rho}}_C^T)\mathbf{1} - (\boldsymbol{\rho}_C\dot{\boldsymbol{\rho}}_C^T + \dot{\boldsymbol{\rho}}_C\boldsymbol{\rho}_C^T)\big) \cdot \boldsymbol{\omega}$

$$m\left(\begin{bmatrix} 2\rho_x\dot{\rho}_x & 0 & 0 \\ 0 & 2\rho_y\dot{\rho}_y & 0 \\ 0 & 0 & 2\rho_z\dot{\rho}_z \end{bmatrix} - \begin{bmatrix} 2\rho_x\dot{\rho}_x & \rho_x\dot{\rho}_y + \dot{\rho}_x\rho_y & \rho_x\dot{\rho}_z + \dot{\rho}_x\rho_z \\ \rho_x\dot{\rho}_y + \dot{\rho}_x\rho_y & 2\rho_y\dot{\rho}_y & \rho_y\dot{\rho}_z + \dot{\rho}_y\rho_z \\ \rho_x\dot{\rho}_z + \dot{\rho}_x\rho_z & \rho_y\dot{\rho}_z + \dot{\rho}_y\rho_z & 2\rho_z\dot{\rho}_z \end{bmatrix}\right)$$
$$= \begin{bmatrix} 0 & -m\big(\rho_x\dot{\rho}_y + \dot{\rho}_x\rho_y\big) & -m(\rho_x\dot{\rho}_z + \dot{\rho}_x\rho_z) \\ -m\big(\rho_x\dot{\rho}_y + \dot{\rho}_x\rho_y\big) & 0 & -m\big(\rho_y\dot{\rho}_z + \dot{\rho}_y\rho_z\big) \\ -m(\rho_x\dot{\rho}_z + \dot{\rho}_x\rho_z) & -m\big(\rho_y\dot{\rho}_z + \dot{\rho}_y\rho_z\big) & 0 \end{bmatrix} \tag{D-22}$$

$$\begin{bmatrix} 0 & -m\big(\rho_x\dot{\rho}_y + \dot{\rho}_x\rho_y\big) & -m(\rho_x\dot{\rho}_z + \dot{\rho}_x\rho_z) \\ -m\big(\rho_x\dot{\rho}_y + \dot{\rho}_x\rho_y\big) & 0 & -m\big(\rho_y\dot{\rho}_z + \dot{\rho}_y\rho_z\big) \\ -m(\rho_x\dot{\rho}_z + \dot{\rho}_x\rho_z) & -m\big(\rho_y\dot{\rho}_z + \dot{\rho}_y\rho_z\big) & 0 \end{bmatrix} \cdot \begin{bmatrix} \omega_x \\ \omega_y \\ \omega_z \end{bmatrix}$$
$$= \begin{bmatrix} -m\omega_y\big(\rho_x\dot{\rho}_y + \dot{\rho}_x\rho_y\big) - m\omega_z(\rho_x\dot{\rho}_z + \dot{\rho}_x\rho_z) \\ -m\omega_x\big(\rho_x\dot{\rho}_y + \dot{\rho}_x\rho_y\big) - m\omega_z\big(\rho_y\dot{\rho}_z + \dot{\rho}_y\rho_z\big) \\ -m\omega_x(\rho_x\dot{\rho}_z + \dot{\rho}_x\rho_z) - m\omega_y\big(\rho_y\dot{\rho}_z + \dot{\rho}_y\rho_z\big) \end{bmatrix} \tag{D-23}$$

f) $\boldsymbol{\rho}_C \times m(\dot{\boldsymbol{\omega}} \times \boldsymbol{\rho}_C)$

$$m(\dot{\boldsymbol{\omega}} \times \boldsymbol{\rho}_C) = m\begin{vmatrix} \hat{\imath} & \hat{\jmath} & \hat{k} \\ \dot{\omega}_x & \dot{\omega}_y & \dot{\omega}_z \\ \rho_x & \rho_y & \rho_z \end{vmatrix} = \begin{bmatrix} m\big(\dot{\omega}_y\rho_z - \dot{\omega}_z\rho_y\big) \\ m(\dot{\omega}_z\rho_x - \dot{\omega}_x\rho_z) \\ m\big(\dot{\omega}_x\rho_y - \dot{\omega}_y\rho_x\big) \end{bmatrix} \tag{D-24}$$

$$\begin{vmatrix} \hat{\imath} & \hat{\jmath} & \hat{k} \\ \rho_x & \rho_y & \rho_z \\ m\big(\dot{\omega}_y\rho_z - \dot{\omega}_z\rho_y\big) & m(\dot{\omega}_z\rho_x - \dot{\omega}_x\rho_z) & m\big(\dot{\omega}_x\rho_y - \dot{\omega}_y\rho_x\big) \end{vmatrix} =$$

$$\begin{bmatrix} m\rho_y\big(\dot{\omega}_x\rho_y - \dot{\omega}_y\rho_x\big) - m\rho_z(\dot{\omega}_z\rho_x - \dot{\omega}_x\rho_z) \\ m\rho_z\big(\dot{\omega}_y\rho_z - \dot{\omega}_z\rho_y\big) - m\rho_x\big(\dot{\omega}_x\rho_y - \dot{\omega}_y\rho_x\big) \\ m\rho_x(\dot{\omega}_z\rho_x - \dot{\omega}_x\rho_z) - m\rho_y\big(\dot{\omega}_y\rho_z - \dot{\omega}_z\rho_y\big) \end{bmatrix} \tag{D-25}$$

g) $\boldsymbol{\rho}_C \times m\big(\boldsymbol{\omega} \times (\boldsymbol{\omega} \times \boldsymbol{\rho}_C)\big)$

$$(\boldsymbol{\omega} \times \boldsymbol{\rho}_C) = \begin{vmatrix} \hat{\imath} & \hat{\jmath} & \hat{k} \\ \omega_x & \omega_y & \omega_z \\ \rho_x & \rho_y & \rho_z \end{vmatrix} = \begin{bmatrix} \omega_y\rho_z - \omega_z\rho_y \\ \omega_z\rho_x - \omega_x\rho_z \\ \omega_x\rho_y - \omega_y\rho_x \end{bmatrix} \tag{D-26}$$

$$\begin{aligned} m\big(\boldsymbol{\omega} \times (\boldsymbol{\omega} \times \boldsymbol{\rho}_C)\big) &= m\begin{vmatrix} \hat{\imath} & \hat{\jmath} & \hat{k} \\ \omega_x & \omega_y & \omega_z \\ \omega_y\rho_z - \omega_z\rho_y & \omega_z\rho_x - \omega_x\rho_z & \omega_x\rho_y - \omega_y\rho_x \end{vmatrix} \\ &= \begin{bmatrix} m\omega_y\big(\omega_x\rho_y - \omega_y\rho_x\big) - m\omega_z(\omega_z\rho_x - \omega_x\rho_z) \\ m\omega_z\big(\omega_y\rho_z - \omega_z\rho_y\big) - m\omega_x\big(\omega_x\rho_y - \omega_y\rho_x\big) \\ m\omega_x(\omega_z\rho_x - \omega_x\rho_z) - m\omega_y\big(\omega_y\rho_z - \omega_z\rho_y\big) \end{bmatrix} \end{aligned} \tag{D-27}$$

$$\begin{vmatrix} \hat{\imath} & \hat{\jmath} & \hat{k} \\ \rho_x & \rho_y & \rho_z \\ m\omega_y\big(\omega_x\rho_y - \omega_y\rho_x\big) - m\omega_z(\omega_z\rho_x - \omega_x\rho_z) & m\omega_z\big(\omega_y\rho_z - \omega_z\rho_y\big) - m\omega_x\big(\omega_x\rho_y - \omega_y\rho_x\big) & m\omega_x(\omega_z\rho_x - \omega_x\rho_z) - m\omega_y\big(\omega_y\rho_z - \omega_z\rho_y\big) \end{vmatrix} \tag{D-28}$$

$$\begin{bmatrix} \rho_y\Big(m\omega_x(\omega_z\rho_x - \omega_x\rho_z) - m\omega_y\big(\omega_y\rho_z - \omega_z\rho_y\big)\Big) - \rho_z\Big(m\omega_z\big(\omega_y\rho_z - \omega_z\rho_y\big) - m\omega_x\big(\omega_x\rho_y - \omega_y\rho_x\big)\Big) \\ \rho_z\Big(m\omega_y\big(\omega_x\rho_y - \omega_y\rho_x\big) - m\omega_z(\omega_z\rho_x - \omega_x\rho_z)\Big) - \rho_x\Big(m\omega_x(\omega_z\rho_x - \omega_x\rho_z) - m\omega_y\big(\omega_y\rho_z - \omega_z\rho_y\big)\Big) \\ \rho_x\Big(m\omega_z\big(\omega_y\rho_z - \omega_z\rho_y\big) - m\omega_x\big(\omega_x\rho_y - \omega_y\rho_x\big)\Big) - \rho_y\Big(m\omega_y\big(\omega_x\rho_y - \omega_y\rho_x\big) - m\omega_z(\omega_z\rho_x - \omega_x\rho_z)\Big) \end{bmatrix} \tag{D-29}$$

h) $\boldsymbol{\rho}_C \times m(\ddot{\boldsymbol{\rho}}_C)_r$

$$\boldsymbol{\rho}_{\boldsymbol{c}} \times m(\ddot{\boldsymbol{\rho}}_c)_r = \begin{vmatrix} \hat{\imath} & \hat{\jmath} & \hat{k} \\ \rho_x & \rho_y & \rho_z \\ m(\ddot{\rho}_x)_r & m\big(\ddot{\rho}_y\big)_r & m(\ddot{\rho}_z)_r \end{vmatrix} \tag{D-30}$$

i) $\boldsymbol{\rho}_C \times m(2\boldsymbol{\omega} \times (\dot{\boldsymbol{\rho}}_C)_r)$

$$m(2\boldsymbol{\omega} \times (\dot{\boldsymbol{\rho}}_C)_r) = m\begin{vmatrix} \hat{\imath} & \hat{\jmath} & \hat{k} \\ \omega_x & \omega_y & \omega_z \\ (\dot{\rho}_x)_r & \big(\dot{\rho}_y\big)_r & (\dot{\rho}_z)_r \end{vmatrix} = \begin{bmatrix} m\omega_y(\dot{\rho}_z)_r - m\omega_z\big(\dot{\rho}_y\big)_r \\ m\omega_z(\dot{\rho}_x)_r - m\omega_x(\dot{\rho}_z)_r \\ m\omega_x\big(\dot{\rho}_y\big)_r - m\omega_y(\dot{\rho}_x)_r \end{bmatrix} \tag{D-31}$$

$$\begin{vmatrix} \hat{\imath} & \hat{\jmath} & \hat{k} \\ \rho_x & \rho_y & \rho_z \\ m\omega_y(\dot{\rho}_z)_r - m\omega_z(\dot{\rho}_y)_r & m\omega_z(\dot{\rho}_x)_r - m\omega_x(\dot{\rho}_z)_r & m\omega_x(\dot{\rho}_y)_r - m\omega_y(\dot{\rho}_x)_r \end{vmatrix}$$

$$= \begin{bmatrix} \rho_y\left(m\omega_x(\dot{\rho}_y)_r - m\omega_y(\dot{\rho}_x)_r\right) - \rho_z(m\omega_z(\dot{\rho}_x)_r - m\omega_x(\dot{\rho}_z)_r) \\ \rho_z\left(m\omega_y(\dot{\rho}_z)_r - m\omega_z(\dot{\rho}_y)_r\right) - \rho_x\left(m\omega_x(\dot{\rho}_y)_r - m\omega_y(\dot{\rho}_x)_r\right) \\ \rho_x(m\omega_z(\dot{\rho}_x)_r - m\omega_x(\dot{\rho}_z)_r) - \rho_y\left(m\omega_y(\dot{\rho}_z)_r - m\omega_z(\dot{\rho}_y)_r\right) \end{bmatrix}$$

(D-32)

Substituting the results from Equations (D-16) through (D-32), these operations yields the following general equations of motion,

$$\begin{aligned} M_x = {} & \left(I_{xx}\dot{\omega}_x + I_{xy}\dot{\omega}_y + I_{xz}\dot{\omega}_z\right) + \left(\dot{I}_{xx}\omega_x + \dot{I}_{xy}\omega_y + \dot{I}_{xz}\omega_z\right) \\ & + \left(\omega_x\left(I_{xz}\omega_y - I_{xy}\omega_z\right) + \omega_y\left(I_{yz}\omega_y - I_{yy}\omega_z\right) + \omega_z\left(I_{zz}\omega_y - I_{yz}\omega_z\right)\right) \\ & + \Big[\left(-m\rho_x\rho_y\dot{\omega}_y - m\rho_x\rho_z\dot{\omega}_z\right) \\ & + \left(-m\omega_y\left(\rho_x\dot{\rho}_y + \dot{\rho}_x\rho_y\right) - m\omega_z(\rho_x\dot{\rho}_z + \dot{\rho}_x\rho_z)\right) \\ & + \left(m\rho_y\left(\dot{\omega}_x\rho_y - \dot{\omega}_y\rho_x\right) - m\rho_z(\dot{\omega}_z\rho_x - \dot{\omega}_x\rho_z)\right) \\ & + \Big(\rho_y\left(m\omega_x(\omega_z\rho_x - \omega_x\rho_z) - m\omega_y\left(\omega_y\rho_z - \omega_z\rho_y\right)\right) \\ & - \rho_z\left(m\omega_z\left(\omega_y\rho_z - \omega_z\rho_y\right) - m\omega_x\left(\omega_x\rho_y - \omega_y\rho_x\right)\right)\Big) \\ & + \left(m\rho_y(\ddot{\rho}_z)_r - m\rho_z(\ddot{\rho}_y)_r\right) \\ & + \left(\rho_y\left(m\omega_x(\dot{\rho}_y)_r - m\omega_y(\dot{\rho}_x)_r\right) - \rho_z(m\omega_z(\dot{\rho}_x)_r - m\omega_x(\dot{\rho}_z)_r)\right)\Big] \end{aligned}$$

(D-33)

$$
\begin{aligned}
M_y = {} & \left(I_{xy}\dot{\omega}_x + I_{yy}\dot{\omega}_y + I_{yz}\dot{\omega}_z\right) + \left(\dot{I}_{xy}\omega_x + \dot{I}_{yy}\omega_y + \dot{I}_{yz}\omega_z\right) \\
& + \left(\omega_x(I_{xx}\omega_z - I_{xz}\omega_x) + \omega_y\left(I_{xy}\omega_z - I_{yz}\omega_x\right) + \omega_z(I_{xz}\omega_z - I_{zz}\omega_x)\right) \\
& + \Big[\left(-m\rho_x\rho_y\dot{\omega}_x - m\rho_y\rho_z\dot{\omega}_z\right) \\
& + \left(-m\omega_x\left(\rho_x\dot{\rho}_y + \dot{\rho}_x\rho_y\right) - m\omega_z\left(\rho_y\dot{\rho}_z + \dot{\rho}_y\rho_z\right)\right) \\
& + \left(m\rho_z\left(\dot{\omega}_y\rho_z - \dot{\omega}_z\rho_y\right) - m\rho_x\left(\dot{\omega}_x\rho_y - \dot{\omega}_y\rho_x\right)\right) \\
& + \Big(\rho_z\left(m\omega_y\left(\omega_x\rho_y - \omega_y\rho_x\right) - m\omega_z(\omega_z\rho_x - \omega_x\rho_z)\right) \\
& - \rho_x\left(m\omega_x(\omega_z\rho_x - \omega_x\rho_z) - m\omega_y\left(\omega_y\rho_z - \omega_z\rho_y\right)\right)\Big) \\
& + \left(m\rho_z(\ddot{\rho}_x)_r - m\rho_x(\ddot{\rho}_z)_r\right) \\
& + \left(\rho_z\left(m\omega_y(\dot{\rho}_z)_r - m\omega_z\left(\dot{\rho}_y\right)_r\right) - \rho_x\left(m\omega_x\left(\dot{\rho}_y\right)_r - m\omega_y(\dot{\rho}_x)_r\right)\right)\Big]
\end{aligned}
\tag{D-34}
$$

$$
\begin{aligned}
M_z = {} & \left(I_{xz}\dot{\omega}_x + I_{yz}\dot{\omega}_y + I_{zz}\dot{\omega}_z\right) + \left(\dot{I}_{xz}\omega_x + \dot{I}_{yz}\omega_y + \dot{I}_{zz}\omega_z\right) \\
& + \left(\omega_x\left(I_{xy}\omega_x - I_{xx}\omega_y\right) + \omega_y\left(I_{yy}\omega_x - I_{xy}\omega_y\right) + \omega_z\left(I_{yz}\omega_x - I_{xz}\omega_y\right)\right) \\
& + \Big[\left(-m\rho_x\rho_z\dot{\omega}_x - m\rho_y\rho_z\dot{\omega}_y\right) \\
& + \left(-m\omega_x(\rho_x\dot{\rho}_z + \dot{\rho}_x\rho_z) - m\omega_y\left(\rho_y\dot{\rho}_z + \dot{\rho}_y\rho_z\right)\right) \\
& + \left(m\rho_x(\dot{\omega}_z\rho_x - \dot{\omega}_x\rho_z) - m\rho_y\left(\dot{\omega}_y\rho_z - \dot{\omega}_z\rho_y\right)\right) \\
& + \Big(\rho_x\left(m\omega_z\left(\omega_y\rho_z - \omega_z\rho_y\right) - m\omega_x\left(\omega_x\rho_y - \omega_y\rho_x\right)\right) \\
& - \rho_y\left(m\omega_y\left(\omega_x\rho_y - \omega_y\rho_x\right) - m\omega_z(\omega_z\rho_x - \omega_x\rho_z)\right)\Big) \\
& + \left(m\rho_x\left(\ddot{\rho}_y\right)_r - m\rho_y(\ddot{\rho}_x)_r\right) \\
& + \left(\rho_x(m\omega_z(\dot{\rho}_x)_r - m\omega_x(\dot{\rho}_z)_r) - \rho_y\left(m\omega_y(\dot{\rho}_z)_r - m\omega_z\left(\dot{\rho}_y\right)_r\right)\right)\Big]
\end{aligned}
\tag{D-35}
$$

Expanding Equations (D-33), (D-34), and (D-35),

$$
\begin{aligned}
M_x = {} & I_{xx}\dot{\omega}_x + I_{xy}\dot{\omega}_y + I_{xz}\dot{\omega}_z + \dot{I}_{xx}\omega_x + \dot{I}_{xy}\omega_y + \dot{I}_{xz}\omega_z + I_{xz}\omega_x\omega_y - I_{xy}\omega_x\omega_z \\
& + I_{yz}\omega_y^2 - I_{yy}\omega_y\omega_z + I_{zz}\omega_y\omega_z - I_{yz}\omega_z^2 \\
& + \Big[-m\dot{\omega}_y\rho_x\rho_y - m\dot{\omega}_z\rho_x\rho_z - m\omega_y\rho_x\dot{\rho}_y - m\omega_y\dot{\rho}_x\rho_y - m\omega_z\rho_x\dot{\rho}_z \\
& - m\omega_z\dot{\rho}_x\rho_z + m\dot{\omega}_x\rho_y^2 - m\dot{\omega}_y\rho_x\rho_y - m\dot{\omega}_z\rho_x\rho_z + m\dot{\omega}_x\rho_z^2 \\
& + m\omega_x\omega_z\rho_x\rho_y - m\omega_x^2\rho_y\rho_z - m\omega_y^2\rho_y\rho_z + m\omega_y\omega_z\rho_y^2 - m\omega_y\omega_z\rho_z^2 \\
& + m\omega_z^2\rho_y\rho_z + m\omega_x^2\rho_y\rho_z - m\omega_x\omega_y\rho_x\rho_z + m\rho_y(\ddot{\rho}_z)_r - m\rho_z\left(\ddot{\rho}_y\right)_r \\
& + m\omega_x\rho_y\left(\dot{\rho}_y\right)_r - m\omega_y\rho_y(\dot{\rho}_x)_r - m\omega_z\rho_z(\dot{\rho}_x)_r + m\omega_x\rho_z(\dot{\rho}_z)_r\Big]
\end{aligned}
\tag{D-36}
$$

$$
\begin{aligned}
M_y = {} & I_{xy}\dot{\omega}_x + I_{yy}\dot{\omega}_y + I_{yz}\dot{\omega}_z + \dot{I}_{xy}\omega_x + \dot{I}_{yy}\omega_y + \dot{I}_{yz}\omega_z + I_{xx}\omega_x\omega_z - I_{xz}\omega_x^2 \\
& + I_{xy}\omega_y\omega_z - I_{yz}\omega_x\omega_y + I_{xz}\omega_z^2 - I_{zz}\omega_x\omega_z \\
& + \Big[-m\dot{\omega}_x\rho_x\rho_y - m\rho_y\rho_z\dot{\omega}_z - m\omega_x\rho_x\dot{\rho}_y - m\omega_x\dot{\rho}_x\rho_y - m\omega_z\rho_y\dot{\rho}_z \\
& - m\omega_z\dot{\rho}_y\rho_z + m\dot{\omega}_y\rho_z^2 - m\dot{\omega}_z\rho_y\rho_z - m\dot{\omega}_x\rho_x\rho_y + m\dot{\omega}_y\rho_x^2 \\
& + m\omega_x\omega_y\rho_y\rho_z - m\omega_y^2\rho_x\rho_z - m\omega_z^2\rho_x\rho_z + m\omega_x\omega_z\rho_z^2 - m\omega_x\omega_z\rho_x^2 \\
& + m\omega_x^2\rho_x\rho_z + m\omega_y^2\rho_x\rho_z - m\omega_y\omega_z\rho_x\rho_y + m\rho_z(\ddot{\rho}_x)_r - m\rho_x(\ddot{\rho}_z)_r \\
& + m\omega_y\rho_z(\dot{\rho}_z)_r - m\omega_z\rho_z(\dot{\rho}_y)_r - m\omega_x\rho_x(\dot{\rho}_y)_r + m\omega_y\rho_x(\dot{\rho}_x)_r\Big]
\end{aligned}
\tag{D-37}
$$

$$
\begin{aligned}
M_z = {} & I_{xz}\dot{\omega}_x + I_{yz}\dot{\omega}_y + I_{zz}\dot{\omega}_z + \dot{I}_{xz}\omega_x + \dot{I}_{yz}\omega_y + \dot{I}_{zz}\omega_z + I_{xy}\omega_x^2 - I_{xx}\omega_x\omega_y \\
& + I_{yy}\omega_x\omega_y - I_{xy}\omega_y^2 + I_{yz}\omega_x\omega_z - I_{xz}\omega_y\omega_z \\
& + \Big[-m\rho_x\rho_z\dot{\omega}_x - m\rho_y\rho_z\dot{\omega}_y - m\omega_x\rho_x\dot{\rho}_z - m\omega_x\dot{\rho}_x\rho_z - m\omega_y\rho_y\dot{\rho}_z \\
& - m\omega_y\dot{\rho}_y\rho_z + m\dot{\omega}_z\rho_x^2 - m\dot{\omega}_x\rho_x\rho_z - m\dot{\omega}_y\rho_y\rho_z + m\dot{\omega}_z\rho_y^2 \\
& + m\omega_y\omega_z\rho_x\rho_z - m\omega_z^2\rho_x\rho_y - m\omega_x^2\rho_x\rho_y + m\omega_x\omega_y\rho_x^2 - m\omega_x\omega_y\rho_y^2 \\
& + m\omega_y^2\rho_x\rho_y + m\omega_z^2\rho_x\rho_y - m\omega_x\omega_z\rho_y\rho_z + m\rho_x(\ddot{\rho}_y)_r - m\rho_y(\ddot{\rho}_x)_r \\
& + m\omega_z\rho_x(\dot{\rho}_x)_r - m\omega_x\rho_x(\dot{\rho}_z)_r - m\omega_y\rho_y(\dot{\rho}_z)_r + m\omega_z\rho_y(\dot{\rho}_y)_r\Big]
\end{aligned}
\tag{D-38}
$$

Rearranging terms yields the following generalized rigid body rotational equations of motion with a time-varying mass distribution and an arbitrary reference point. From these equations, we can easily see that the derived equation simplifies to the Generalized Euler equation provided in [87] for a fixed body reference frame origin at the center of mass and a time-constant mass distribution.

$$
\begin{aligned}
M_x = {} & I_{xx}\dot{\omega}_x + I_{xy}(\dot{\omega}_y - \omega_x\omega_z) + I_{xz}(\dot{\omega}_z + \omega_x\omega_y) + (I_{zz} - I_{yy})\omega_y\omega_z \\
& + I_{yz}(\omega_y^2 - \omega_z^2) + \dot{I}_{xx}\omega_x + \dot{I}_{xy}\omega_y + \dot{I}_{xz}\omega_z \\
& - m\Big[2\rho_x\rho_y\dot{\omega}_y + 2\rho_x\rho_z\dot{\omega}_z + \omega_y(\rho_x\dot{\rho}_y + \dot{\rho}_x\rho_y) + \omega_z(\rho_x\dot{\rho}_z + \dot{\rho}_x\rho_z) \\
& - \dot{\omega}_x(\rho_y^2 + \rho_z^2) + \rho_y\rho_z(\omega_y^2 - \omega_z^2) + \omega_y\omega_z(\rho_z^2 - \rho_y^2) \\
& + (\dot{\rho}_x)_r(\omega_y\rho_y + \omega_z\rho_z) - \rho_y\left((\ddot{\rho}_z)_r + \omega_x(\dot{\rho}_y)_r + \omega_x\omega_z\rho_x\right) \\
& + \rho_z\left((\ddot{\rho}_y)_r - \omega_x(\dot{\rho}_z)_r + \omega_x\omega_y\rho_x\right)\Big]
\end{aligned}
\tag{D-39}
$$

$$
\begin{aligned}
M_y = {} & I_{xy}\left(\dot{\omega}_x + \omega_y\omega_z\right) + I_{yy}\dot{\omega}_y + I_{yz}\left(\dot{\omega}_z - \omega_x\omega_y\right) + (I_{xx} - I_{zz})\omega_x\omega_z \\
& + I_{xz}(\omega_z^2 - \omega_x^2) + \dot{I}_{xy}\omega_x + \dot{I}_{yy}\omega_y + \dot{I}_{yz}\omega_z \\
& - m\Big[2\rho_x\rho_y\dot{\omega}_x + 2\rho_y\rho_z\dot{\omega}_z + \omega_x\left(\rho_x\dot{\rho}_y + \dot{\rho}_x\rho_y\right) + \omega_z\left(\rho_y\dot{\rho}_z + \dot{\rho}_y\rho_z\right) \\
& - \dot{\omega}_y(\rho_z^2 + \rho_x^2) + \rho_x\rho_z(\omega_z^2 - \omega_x^2) + \omega_x\omega_z(\rho_x^2 - \rho_z^2) \\
& + \left(\dot{\rho}_y\right)_r(\omega_z\rho_z + \omega_x\rho_x) - \rho_z\left((\ddot{\rho}_x)_r + \omega_y(\dot{\rho}_z)_r + \omega_x\omega_y\rho_y\right) \\
& + \rho_x\left((\ddot{\rho}_z)_r - \omega_y(\dot{\rho}_x)_r + \omega_y\omega_z\rho_y\right)\Big]
\end{aligned} \tag{D-40}
$$

$$
\begin{aligned}
M_z = {} & I_{xz}\left(\dot{\omega}_x - \omega_y\omega_z\right) + I_{yz}\left(\dot{\omega}_y + \omega_x\omega_z\right) + I_{zz}\dot{\omega}_z + \left(I_{yy} - I_{xx}\right)\omega_x\omega_y \\
& + I_{xy}\left(\omega_x^2 - \omega_y^2\right) + \dot{I}_{xz}\omega_x + \dot{I}_{yz}\omega_y + \dot{I}_{zz}\omega_z \\
& - m\Big[2\rho_x\rho_z\dot{\omega}_x + 2\rho_y\rho_z\dot{\omega}_y + \omega_x(\rho_x\dot{\rho}_z + \dot{\rho}_x\rho_z) + \omega_y\left(\rho_y\dot{\rho}_z + \dot{\rho}_y\rho_z\right) \\
& - \dot{\omega}_z\left(\rho_x^2 + \rho_y^2\right) + \rho_x\rho_y\left(\omega_x^2 - \omega_y^2\right) + \omega_x\omega_y\left(\rho_y^2 - \rho_x^2\right) \\
& + (\dot{\rho}_z)_r\left(\omega_x\rho_x + \omega_y\rho_y\right) - \rho_x\left(\left(\ddot{\rho}_y\right)_r + \omega_z(\dot{\rho}_x)_r + \omega_y\omega_z\rho_z\right) \\
& + \rho_y\left((\ddot{\rho}_x)_r - \omega_z\left(\dot{\rho}_y\right)_r + \omega_x\omega_z\rho_z\right)\Big]
\end{aligned} \tag{D-41}
$$

As detailed to a greater extent in Chapter 3, the samara model is using principal axes. The Euler equations can thereby be simplified to the following,

$$
\begin{aligned}
M_x = {} & I_{xx}\dot{\omega}_x + \left(I_{zz} - I_{yy}\right)\omega_y\omega_z + \dot{I}_{xx}\omega_x \\
& - m\Big[2\rho_x\rho_y\dot{\omega}_y + 2\rho_x\rho_z\dot{\omega}_z + \omega_y\left(\rho_x\dot{\rho}_y + \dot{\rho}_x\rho_y\right) + \omega_z(\rho_x\dot{\rho}_z + \dot{\rho}_x\rho_z) \\
& - \dot{\omega}_x\left(\rho_y^2 + \rho_z^2\right) + \rho_y\rho_z\left(\omega_y^2 - \omega_z^2\right) + \omega_y\omega_z\left(\rho_z^2 - \rho_y^2\right) \\
& + (\dot{\rho}_x)_r\left(\omega_y\rho_y + \omega_z\rho_z\right) - \rho_y\left((\ddot{\rho}_z)_r + \omega_x\left(\dot{\rho}_y\right)_r + \omega_x\omega_z\rho_x\right) \\
& + \rho_z\left(\left(\ddot{\rho}_y\right)_r - \omega_x(\dot{\rho}_z)_r + \omega_x\omega_y\rho_x\right)\Big]
\end{aligned} \tag{D-42}
$$

$$
\begin{aligned}
M_y = {} & I_{yy}\dot{\omega}_y + (I_{xx} - I_{zz})\omega_x\omega_z + \dot{I}_{yy}\omega_y \\
& - m\Big[2\rho_x\rho_y\dot{\omega}_x + 2\rho_y\rho_z\dot{\omega}_z + \omega_x\left(\rho_x\dot{\rho}_y + \dot{\rho}_x\rho_y\right) + \omega_z\left(\rho_y\dot{\rho}_z + \dot{\rho}_y\rho_z\right) \\
& - \dot{\omega}_y(\rho_z^2 + \rho_x^2) + \rho_x\rho_z(\omega_z^2 - \omega_x^2) + \omega_x\omega_z(\rho_x^2 - \rho_z^2) \\
& + \left(\dot{\rho}_y\right)_r(\omega_z\rho_z + \omega_x\rho_x) - \rho_z\left((\ddot{\rho}_x)_r + \omega_y(\dot{\rho}_z)_r + \omega_x\omega_y\rho_y\right) \\
& + \rho_x\left((\ddot{\rho}_z)_r - \omega_y(\dot{\rho}_x)_r + \omega_y\omega_z\rho_y\right)\Big]
\end{aligned} \tag{D-43}
$$

$$
\begin{aligned}
M_z = I_{zz}\dot{\omega}_z + \left(I_{yy} - I_{xx}\right)\omega_x\omega_y + \dot{I}_{zz}\omega_z \\
&- m\Big[2\rho_x\rho_z\dot{\omega}_x + 2\rho_y\rho_z\dot{\omega}_y + \omega_x(\rho_x\dot{\rho}_z + \dot{\rho}_x\rho_z) + \omega_y\left(\rho_y\dot{\rho}_z + \dot{\rho}_y\rho_z\right) \\
&- \dot{\omega}_z\left(\rho_x^2 + \rho_y^2\right) + \rho_x\rho_y\left(\omega_x^2 - \omega_y^2\right) + \omega_x\omega_y\left(\rho_y^2 - \rho_x^2\right) \\
&+ (\dot{\rho}_z)_r\left(\omega_x\rho_x + \omega_y\rho_y\right) - \rho_x\left(\left(\ddot{\rho}_y\right)_r + \omega_z(\dot{\rho}_x)_r + \omega_y\omega_z\rho_z\right) \\
&+ \rho_y\left((\ddot{\rho}_x)_r - \omega_z\left(\dot{\rho}_y\right)_r + \omega_x\omega_z\rho_z\right)\Big]
\end{aligned}
\tag{D-44}
$$

D.1. Time-Varying Mass Implementation

Now, the derived generalized rotational equations of motion for time-varying mass distribution using the samara-inspired vehicle diagrammed in Figure 3-3 can be applied. The moving mass is constrained to moving along a linear rail that coincides with the X_b-axis, which means $\rho_y = 0$ and $\rho_z = 0$ for all time. Applying this constraint to Equations (D-42), (D-43), and (D-44) yields the following,

$$
\boxed{
\begin{aligned}
M_x &= I_{xx}\dot{\omega}_x + \left(I_{zz} - I_{yy}\right)\omega_y\omega_z + \dot{I}_{xx}\omega_x && \text{(D-45)} \\
M_y &= \left(I_{yy} + m\rho_x^2\right)\dot{\omega}_y + (I_{xx} - I_{zz} - m\rho_x^2)\omega_x\omega_z + \left(\dot{I}_{yy} + m\rho_x(\dot{\rho}_x)_r\right)\omega_y && \text{(D-46)} \\
M_z &= (I_{zz} + m\rho_x^2)\dot{\omega}_z + \left(I_{yy} - I_{xx} + m\rho_x^2\right)\omega_x\omega_y + \left(\dot{I}_{zz} + m\rho_x(\dot{\rho}_x)_r\right)\omega_z && \text{(D-47)}
\end{aligned}
}
$$

Substituting the angular velocity terms found in Equations (B-9) and (B-10) into Equations (D-45), (D-46), and (D-47),

$$
\begin{aligned}
M_x = I_{xx}\left(\ddot{\psi} + \ddot{\phi}\sin\theta + \dot{\phi}\dot{\theta}\cos\theta\right) \\
&+ \left(I_{zz} - I_{yy}\right)\left(\dot{\phi}\cos\theta\sin\psi - \dot{\theta}\cos\psi\right)\left(\dot{\phi}\cos\theta\cos\psi + \dot{\theta}\sin\psi\right) \\
&+ \dot{I}_{xx}\left(\dot{\psi} + \dot{\phi}\sin\theta\right)
\end{aligned}
\tag{D-48}
$$

$$
\begin{aligned}
M_y = \left(I_{yy} + m\rho_x^2\right)\big(\ddot{\phi}\cos\theta\sin\psi - \ddot{\theta}\cos\psi - \dot{\phi}\dot{\theta}\sin\theta\sin\psi + \dot{\phi}\dot{\psi}\cos\theta\cos\psi \\
&+ \dot{\theta}\dot{\psi}\sin\psi\big) \\
&+ (I_{xx} - I_{zz} - m\rho_x^2)\left(\dot{\psi} + \dot{\phi}\sin\theta\right)\left(\dot{\phi}\cos\theta\cos\psi + \dot{\theta}\sin\psi\right) \\
&+ \left(\dot{I}_{yy} + m\rho_x(\dot{\rho}_x)_r\right)\left(\dot{\phi}\cos\theta\sin\psi - \dot{\theta}\cos\psi\right)
\end{aligned}
\tag{D-49}
$$

$$
\begin{aligned}
M_z = (I_{zz} + m\rho_x^2)\big(\ddot{\phi}\cos\theta\cos\psi + \ddot{\theta}\sin\psi - \dot{\phi}\dot{\theta}\sin\theta\cos\psi - \dot{\phi}\dot{\psi}\cos\theta\sin\psi \\
&+ \dot{\theta}\dot{\psi}\cos\psi\big) \\
&+ \left(I_{yy} - I_{xx} + m\rho_x^2\right)\left(\dot{\psi} + \dot{\phi}\sin\theta\right)\left(\dot{\phi}\cos\theta\sin\psi - \dot{\theta}\cos\psi\right) \\
&+ \left(\dot{I}_{zz} + m\rho_x(\dot{\rho}_x)_r\right)\left(\dot{\phi}\cos\theta\cos\psi + \dot{\theta}\sin\psi\right)
\end{aligned}
\tag{D-50}
$$

Solving Equations (D-48), (D-49), and (D-50) for $\ddot{\phi}$, $\ddot{\theta}$, and $\ddot{\psi}$,

$$\ddot{\psi} = \frac{M_x}{I_{xx}} - \frac{\left(I_{zz} - I_{yy}\right)}{I_{xx}}\left(\dot{\phi}\cos\theta\sin\psi - \dot{\theta}\cos\psi\right)\left(\dot{\phi}\cos\theta\cos\psi + \dot{\theta}\sin\psi\right) - \frac{\dot{I}_{xx}}{I_{xx}}\left(\dot{\psi} + \dot{\phi}\sin\theta\right) - \ddot{\phi}\sin\theta - \dot{\phi}\dot{\theta}\cos\theta \tag{D-51}$$

$$\begin{aligned}\ddot{\theta} = -&\frac{M_y}{\left(I_{yy} + m\rho_x^2\right)\cos\psi} \\ &+ \frac{\left(I_{xx} - I_{zz} - m\rho_x^2\right)}{\left(I_{yy} + m\rho_x^2\right)\cos\psi}\left(\dot{\psi} + \dot{\phi}\sin\theta\right)\left(\dot{\phi}\cos\theta\cos\psi + \dot{\theta}\sin\psi\right) \\ &+ \frac{\left(\dot{I}_{yy} + m\rho_x(\dot{\rho}_x)_r\right)}{\left(I_{yy} + m\rho_x^2\right)\cos\psi}\left(\dot{\phi}\cos\theta\sin\psi - \dot{\theta}\cos\psi\right) + \frac{\ddot{\phi}\cos\theta\sin\psi}{\cos\psi} \\ &- \frac{\dot{\phi}\dot{\theta}\sin\theta\sin\psi}{\cos\psi} + \frac{\dot{\phi}\dot{\psi}\cos\theta\cos\psi}{\cos\psi} + \frac{\dot{\theta}\dot{\psi}\sin\psi}{\cos\psi}\end{aligned} \tag{D-52}$$

$$\begin{aligned}\ddot{\phi} = &\frac{M_z}{\left(I_{zz} + m\rho_x^2\right)\cos\theta\cos\psi} \\ &- \frac{\left(I_{yy} - I_{xx} + m\rho_x^2\right)}{\left(I_{zz} + m\rho_x^2\right)\cos\theta\cos\psi}\left(\dot{\psi} + \dot{\phi}\sin\theta\right)\left(\dot{\phi}\cos\theta\sin\psi - \dot{\theta}\cos\psi\right) \\ &- \frac{\left(\dot{I}_{zz} + m\rho_x(\dot{\rho}_x)_r\right)}{\left(I_{zz} + m\rho_x^2\right)\cos\theta\cos\psi}\left(\dot{\phi}\cos\theta\cos\psi + \dot{\theta}\sin\psi\right) - \frac{\ddot{\theta}\sin\psi}{\cos\theta\cos\psi} \\ &+ \frac{\dot{\phi}\dot{\theta}\sin\theta\cos\psi}{\cos\theta\cos\psi} + \frac{\dot{\phi}\dot{\psi}\cos\theta\sin\psi}{\cos\theta\cos\psi} - \frac{\dot{\theta}\dot{\psi}\cos\psi}{\cos\theta\cos\psi}\end{aligned} \tag{D-53}$$

Substituting the Equations (D-52) and (D-53) into each other to find independent equations of motion for $\ddot{\theta}$ and $\ddot{\phi}$,

$$
\begin{aligned}
\ddot{\theta} = -\frac{M_y}{\left(I_{yy} + m\rho_x^2\right)\cos\psi}(\cos\psi\cos\psi) \\
&+ \frac{\left(I_{xx} - I_{zz} - m\rho_x^2\right)}{\left(I_{yy} + m\rho_x^2\right)\cos\psi}(\cos\psi\cos\psi)\left(\dot{\psi} + \dot{\phi}\sin\theta\right)\left(\dot{\phi}\cos\theta\cos\psi\right. \\
&\left.+ \dot{\theta}\sin\psi\right) \\
&+ \frac{\left(\dot{I}_{yy} + m\rho_x(\dot{\rho}_x)_r\right)}{\left(I_{yy} + m\rho_x^2\right)\cos\psi}(\cos\psi\cos\psi)\left(\dot{\phi}\cos\theta\sin\psi - \dot{\theta}\cos\psi\right) \\
&+ \frac{M_z}{\left(I_{zz} + m\rho_x^2\right)\cos\theta\cos\psi}(\cos\psi\cos\psi)\left(\frac{\cos\theta\sin\psi}{\cos\psi}\right) \\
&- \frac{\left(I_{yy} - I_{xx} + m\rho_x^2\right)}{\left(I_{zz} + m\rho_x^2\right)\cos\theta\cos\psi}(\cos\psi\cos\psi)\left(\frac{\cos\theta\sin\psi}{\cos\psi}\right)\left(\dot{\psi}\right. \\
&\left.+ \dot{\phi}\sin\theta\right)\left(\dot{\phi}\cos\theta\sin\psi - \dot{\theta}\cos\psi\right) \\
&- \frac{\left(\dot{I}_{zz} + m\rho_x(\dot{\rho}_x)_r\right)}{\left(I_{zz} + m\rho_x^2\right)\cos\theta\cos\psi}(\cos\psi\cos\psi)\left(\frac{\cos\theta\sin\psi}{\cos\psi}\right)\left(\dot{\phi}\cos\theta\cos\psi\right. \\
&\left.+ \dot{\theta}\sin\psi\right) + \frac{\dot{\phi}\dot{\theta}\sin\theta\cos\psi}{\cos\theta\cos\psi}(\cos\psi\cos\psi)\left(\frac{\cos\theta\sin\psi}{\cos\psi}\right) \\
&+ \frac{\dot{\phi}\dot{\psi}\cos\theta\sin\psi}{\cos\theta\cos\psi}(\cos\psi\cos\psi)\left(\frac{\cos\theta\sin\psi}{\cos\psi}\right) \\
&- \frac{\dot{\theta}\dot{\psi}\cos\psi}{\cos\theta\cos\psi}(\cos\psi\cos\psi)\left(\frac{\cos\theta\sin\psi}{\cos\psi}\right) \\
&- \frac{\dot{\phi}\dot{\theta}\sin\theta\sin\psi}{\cos\psi}(\cos\psi\cos\psi) + \frac{\dot{\phi}\dot{\psi}\cos\theta\cos\psi}{\cos\psi}(\cos\psi\cos\psi) \\
&+ \frac{\dot{\theta}\dot{\psi}\sin\psi}{\cos\psi}(\cos\psi\cos\psi)
\end{aligned}
\tag{D-54}
$$

$$
\begin{aligned}
\ddot{\phi} = &\frac{M_z}{(I_{zz}+m\rho_x^2)\cos\theta\cos\psi}(\cos\psi\cos\psi) \\
&- \frac{(I_{yy}-I_{xx}+m\rho_x^2)}{(I_{zz}+m\rho_x^2)\cos\theta\cos\psi}(\cos\psi\cos\psi)(\dot{\psi}+\dot{\phi}\sin\theta)(\dot{\phi}\cos\theta\sin\psi \\
&- \dot{\theta}\cos\psi) \\
&- \frac{(\dot{I}_{zz}+m\rho_x(\dot{\rho}_x)_r)}{(I_{zz}+m\rho_x^2)\cos\theta\cos\psi}(\cos\psi\cos\psi)(\dot{\phi}\cos\theta\cos\psi+\dot{\theta}\sin\psi) \\
&+ \frac{M_y}{(I_{yy}+m\rho_x^2)\cos\psi}(\cos\psi\cos\psi)\left(\frac{\sin\psi}{\cos\theta\cos\psi}\right) \\
&- \frac{(I_{xx}-I_{zz}-m\rho_x^2)}{(I_{yy}+m\rho_x^2)\cos\psi}(\cos\psi\cos\psi)\left(\frac{\sin\psi}{\cos\theta\cos\psi}\right)(\dot{\psi} \\
&+ \dot{\phi}\sin\theta)(\dot{\phi}\cos\theta\cos\psi+\dot{\theta}\sin\psi) \\
&- \frac{(\dot{I}_{yy}+m\rho_x(\dot{\rho}_x)_r)}{(I_{yy}+m\rho_x^2)\cos\psi}(\cos\psi\cos\psi)\left(\frac{\sin\psi}{\cos\theta\cos\psi}\right)(\dot{\phi}\cos\theta\sin\psi \\
&- \dot{\theta}\cos\psi) + \frac{\dot{\phi}\dot{\theta}\sin\theta\sin\psi}{\cos\psi}(\cos\psi\cos\psi)\left(\frac{\sin\psi}{\cos\theta\cos\psi}\right) \\
&- \frac{\dot{\phi}\dot{\psi}\cos\theta\cos\psi}{\cos\psi}(\cos\psi\cos\psi)\left(\frac{\sin\psi}{\cos\theta\cos\psi}\right) \\
&- \frac{\dot{\theta}\dot{\psi}\sin\psi}{\cos\psi}(\cos\psi\cos\psi)\left(\frac{\sin\psi}{\cos\theta\cos\psi}\right) + \frac{\dot{\phi}\dot{\theta}\sin\theta\cos\psi}{\cos\theta\cos\psi}(\cos\psi\cos\psi) \\
&+ \frac{\dot{\phi}\dot{\psi}\cos\theta\sin\psi}{\cos\theta\cos\psi}(\cos\psi\cos\psi) - \frac{\dot{\theta}\dot{\psi}\cos\psi}{\cos\theta\cos\psi}(\cos\psi\cos\psi)
\end{aligned}
\tag{D-55}
$$

Simplifying the Equations (D-54) and (D-55) yields the following,

$$
\begin{aligned}
\ddot{\theta} = &-\frac{M_y\cos\psi}{(I_{yy}+m\rho_x^2)} \\
&+ \frac{(I_{xx}-I_{zz}-m\rho_x^2)}{(I_{yy}+m\rho_x^2)}(\dot{\psi}+\dot{\phi}\sin\theta)(\dot{\phi}\cos\theta\cos^2\psi+\dot{\theta}\sin\psi\cos\psi) \\
&+ \frac{(\dot{I}_{yy}+m\rho_x(\dot{\rho}_x)_r)}{(I_{yy}+m\rho_x^2)}(\dot{\phi}\cos\theta\sin\psi\cos\psi-\dot{\theta}\cos^2\psi) + \frac{M_z\sin\psi}{(I_{zz}+m\rho_x^2)} \\
&- \frac{(I_{yy}-I_{xx}+m\rho_x^2)}{(I_{zz}+m\rho_x^2)}(\dot{\psi}+\dot{\phi}\sin\theta)(\dot{\phi}\cos\theta\sin^2\psi-\dot{\theta}\sin\psi\cos\psi) \\
&- \frac{(\dot{I}_{zz}+m\rho_x(\dot{\rho}_x)_r)}{(I_{zz}+m\rho_x^2)}(\dot{\phi}\cos\theta\sin\psi\cos\psi+\dot{\theta}\sin^2\psi) + \dot{\phi}\dot{\psi}\cos\theta
\end{aligned}
\tag{D-56}
$$

$$
\begin{aligned}
\ddot{\phi} = & \frac{M_z \cos\psi}{(I_{zz} + m\rho_x^2)\cos\theta} \\
& - \frac{\left(I_{yy} - I_{xx} + m\rho_x^2\right)}{(I_{zz} + m\rho_x^2)}\left(\dot{\psi} + \dot{\phi}\sin\theta\right)\left(\dot{\phi}\sin\psi\cos\psi - \frac{\dot{\theta}\cos^2\psi}{\cos\theta}\right) \\
& - \frac{\left(\dot{I}_{zz} + m\rho_x(\dot{\rho}_x)_r\right)}{(I_{zz} + m\rho_x^2)}\left(\dot{\phi}\cos^2\psi + \frac{\dot{\theta}\sin\psi\cos\psi}{\cos\theta}\right) + \frac{M_y \sin\psi}{\left(I_{yy} + m\rho_x^2\right)\cos\theta} \\
& - \frac{(I_{xx} - I_{zz} - m\rho_x^2)}{\left(I_{yy} + m\rho_x^2\right)}\left(\dot{\psi} + \dot{\phi}\sin\theta\right)\left(\dot{\phi}\sin\psi\cos\psi + \frac{\dot{\theta}\sin^2\psi}{\cos\theta}\right) \\
& - \frac{\left(\dot{I}_{yy} + m\rho_x(\dot{\rho}_x)_r\right)}{\left(I_{yy} + m\rho_x^2\right)}\left(\dot{\phi}\sin^2\psi - \frac{\dot{\theta}\sin\psi\cos\psi}{\cos\theta}\right) + \frac{\dot{\phi}\dot{\theta}\sin\theta}{\cos\theta} - \frac{\dot{\theta}\dot{\psi}}{\cos\theta}
\end{aligned} \tag{D-57}
$$

In order to get an independent equation of motion for $\ddot{\psi}$, Equation (D-57) is substituted into Equation (D-51). As can be seen from Equation (C-15), $\dot{I}_{xx} = 0$. Also, As assumed in Chapter 3, $M_x \approx 0$. Therefore, a simplified independent equation of motion for is defined as follows.

$$
\begin{aligned}
\ddot{\psi} = & -\frac{\left(I_{zz} - I_{yy}\right)}{I_{xx}}\left(\dot{\phi}\cos\theta\sin\psi - \dot{\theta}\cos\psi\right)\left(\dot{\phi}\cos\theta\cos\psi + \dot{\theta}\sin\psi\right) \\
& - \frac{M_z}{(I_{zz} + m\rho_x^2)}(\tan\theta\cos\psi) \\
& + \frac{\left(I_{yy} - I_{xx} + m\rho_x^2\right)}{(I_{zz} + m\rho_x^2)}\left(\dot{\psi}\sin\theta + \dot{\phi}\sin^2\theta\right)\left(\dot{\phi}\sin\psi\cos\psi - \frac{\dot{\theta}\cos^2\psi}{\cos\theta}\right) \\
& + \frac{\left(\dot{I}_{zz} + m\rho_x(\dot{\rho}_x)_r\right)}{(I_{zz} + m\rho_x^2)}\left(\dot{\phi}\sin\theta\cos^2\psi + \dot{\theta}\tan\theta\sin\psi\cos\psi\right) \\
& - \frac{M_y}{\left(I_{yy} + m\rho_x^2\right)}(\tan\theta\sin\psi) \\
& + \frac{(I_{xx} - I_{zz} - m\rho_x^2)}{\left(I_{yy} + m\rho_x^2\right)}\left(\dot{\psi}\sin\theta + \dot{\phi}\sin^2\theta\right)\left(\dot{\phi}\sin\psi\cos\psi + \frac{\dot{\theta}\sin^2\psi}{\cos\theta}\right) \\
& + \frac{\left(\dot{I}_{yy} + m\rho_x(\dot{\rho}_x)_r\right)}{\left(I_{yy} + m\rho_x^2\right)}\left(\dot{\phi}\sin\theta\sin^2\psi - \dot{\theta}\tan\theta\sin\psi\cos\psi\right) \\
& - \dot{\phi}\dot{\theta}(\tan\theta\sin\theta + \cos\theta) + \dot{\theta}\dot{\psi}\tan\theta
\end{aligned} \tag{D-58}
$$

D.2. McConnell & Das Implementation

Since McConnell and Das did not use a time-varying mass in their model, they could use the samara center of mass as the fixed body frame origin. With these assumptions, the rotational equations of motion can be simplified to the following equations consistent with those used in [1] [2] [3],

$$
\begin{aligned}
M_y &= I_{yy}\dot{\omega}_y + (I_{xx} - I_{zz})\omega_x\omega_z \\
M_z &= I_{zz}\dot{\omega}_z + \left(I_{yy} - I_{xx}\right)\omega_x\omega_y
\end{aligned}
\tag{D-59}
$$

Furthermore, since the samara was modeled as a thin rod, $I_{xx} = 0$ and $I_{yy} = I_{zz}$, which simplifies the model to the following,

$$
\begin{aligned}
M_y &= I_{yy}\dot{\omega}_y - I_{yy}\omega_x\omega_z \\
M_z &= I_{yy}\dot{\omega}_z + I_{yy}\omega_x\omega_y
\end{aligned}
\tag{D-60}
$$

Substituting the angular velocity terms found in Equation (B-9) and (B-10) into Equation (D-60) and simplifying the angular velocity terms based on the assumption $\psi = \dot{\psi} \approx 0$,

$$
\begin{aligned}
M_y &= I_{yy}\left(-\ddot{\theta}\right) - I_{yy}\left(\dot{\phi}\sin\theta\right)\left(\dot{\phi}\cos\theta\right) \\
M_z &= I_{yy}\left(\ddot{\phi}\cos\theta - \dot{\phi}\dot{\theta}\sin\theta\right) + I_{yy}\left(\dot{\phi}\sin\theta\right)\left(-\dot{\theta}\right)
\end{aligned}
\tag{D-61}
$$

Simplifying and solving for $\ddot{\theta}$ and $\ddot{\phi}$, respectively, it can be shown below that the derivation of the rotational equations of motion found in this paper match that which was published in [1] [2] [3].

$$
\begin{aligned}
\ddot{\theta} &= -\frac{M_y}{I_{yy}} - \dot{\phi}^2\sin\theta\cos\theta \\
\ddot{\phi} &= \frac{M_z}{I_{yy}\cos\theta} + \frac{2\dot{\phi}\dot{\theta}\sin\theta}{\cos\theta}
\end{aligned}
\tag{D-62}
$$

Appendix E. Derivation of Translational Equations of Motion

This appendix derives the translational equations of motion used in this report. Figure E-1 shown below depicts the forces associated with the translational motion of the samara with respect to the inertial reference frame. The total force acting on the samara can be divided into two categories: $\boldsymbol{F}_i$, the net aerodynamic forces acting on the samara, and $\boldsymbol{F}_g$, the gravitational force acting on the samara. As described in Chapter 3, the Z_i-Axis of the inertial reference frame is defined to be in the negative direction of gravity.

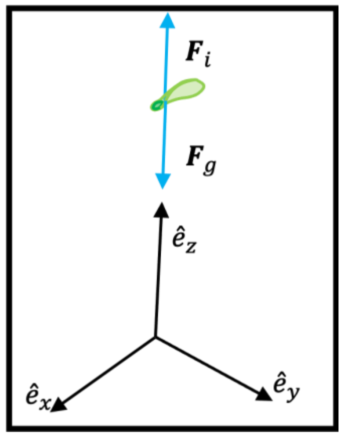

Figure E-1. Free body diagram of a samara in inertial space.

Since the analysis in this paper considers the time-varying effects of the samara in flight, all spatial components of translational velocity in the inertial reference frame need to be considered.

$$m\dot{\boldsymbol{v}}_O = -\vec{\boldsymbol{F}}_i = F_{x_i}\hat{e}_x + F_{y_i}\hat{e}_y + \left(-F_{g_i} + F_{z_i}\right)\hat{e}_z \tag{E-1}$$

Separating Equation (E-1) into three scalar equations that focus on each of the inertial reference frame components,

$$\boxed{\begin{aligned} m\dot{v}_x &= F_{x_i} \\ m\dot{v}_y &= F_{y_i} \\ m\dot{v}_z &= -F_{g_i} + F_{z_i} \end{aligned}} \tag{E-2}$$

Using the rotation matrix defined in Equation (A-8), the generalized aerodynamic forces derived in Chapter 3 can be defined in the inertial reference frame, which yields the following translational equation of motion can be defined as follows,

$$\begin{aligned} \dot{v}_x = \Big(& F_{x_b}\cos\phi\cos\theta + F_{y_b}(-\sin\phi\cos\psi - \cos\phi\sin\theta\sin\psi) \\ &+ F_{z_b}(\sin\phi\sin\psi - \cos\phi\sin\theta\cos\psi)\Big)/m \end{aligned} \tag{E-3}$$

$$\dot{v}_y = \Big(F_{x_b}\sin\phi\cos\theta + F_{y_b}(\cos\phi\cos\psi - \sin\phi\sin\theta\sin\psi) + F_{z_b}(-\cos\phi\sin\psi - \sin\phi\sin\theta\cos\psi)\Big)/m \tag{E-4}$$

$$\dot{v}_z = -g + \left(F_{x_b}\sin\theta + F_{y_b}\cos\theta\sin\psi + F_{z_b}\cos\theta\cos\psi\right)/m \tag{E-5}$$

where m is the total mass of the samara, g is the gravitational acceleration, and $\{F_{x_b}, F_{y_b}, F_{z_b}\}$ are the generalized forces acting on the samara in the fixed body reference frame.

While McConnell and Das simplified their model to only consider vertical translation in the Z_i-direction, their work can be used as a point of reference to build confidence that this extended derivation aligns with their findings. With some minor algebraic manipulation, Equation (E-5) can be modified to reflect what is found in [1] [2] [3],

$$m\dot{v}_z = -mg + F_{x_b}\sin\theta + F_{y_b}\cos\theta\sin\psi + F_{z_b}\cos\theta\cos\psi \tag{E-6}$$

Solving for $\dot{v}_z$ and introducing the assumptions used in [1] [2] [3] ($\psi \approx 0$ and $F_{x_b} \approx 0$), the equation simplifies to what was used in the reduced order model [1] [2] [3],

$$\dot{v}_z = -g + \frac{F_{z_b}\cos\theta}{m} \tag{E-7}$$